THE UNIVERSITY OF QUEENSLAND

AUSTRALIA

Evaluating Acquisition Techniques for Functional Magnetic Resonance Imaging at Ultra-High Field

Saskia Bollmann

B.Sc., M.Sc.

A thesis submitted for the degree of Doctor of Philosophy at

The University of Queensland in 2018

Queensland Brain Institute

Abstract

Functional magnetic resonance imaging (fMRI) enables the non-invasive investigation of human brain function. Identifying functionally segregated regions involved in the processing of sensory information and higher cognitive functions has provided detailed insight into its organisational architecture. The acquisition of fMRI data at ultra-high field provides enhanced signal sensitivity and contrast, and new acquisition techniques are continuously developed to increase image resolution and acquisition speed. The ultimate goal is to maximize functional sensitivity, i.e. the ability to detect and localise neurovascular activity using fMRI. Given the overwhelming number of parameters that need to be selected to compile an fMRI acquisition protocol, and their complex influences on image fidelity and contrast, ascertaining functional sensitivity is fundamental for every fMRI experiment. Only then a faithful representation of the underlying neurovascular activity can be obtained, forming the basis for new insights into brain function.

In this thesis, I will discuss key constituents of functional sensitivity, provide an overview of the impact of fMRI acquisition parameters, and outline relevant evaluation measures. I will then apply this framework to the functional imaging of the nuclei of the basal ganglia, whose tissue properties cause a reduction in functional sensitivity compared to cortical areas. I will show how multi-echo fMRI – a new class of fMRI data acquisition techniques – can overcome this limitation. By rapidly acquiring sets of images with different signal properties, the extensive signal loss in subcortical regions can be mitigated without sacrificing functional sensitivity in cortical areas.

Subsequently, I will investigate the noise properties of fMRI data acquired with a sub-second sampling interval at the single-subject level. Single-subject fMRI is especially relevant for clinical applications, but requires comprehensive noise modelling for valid inference. Accordingly, I will show that modelling of physiological noise sources such as cardiac and respiratory activity, and advanced pre-whitening schemes are necessary for valid inference using fast acquisition techniques.

To finish, I will introduce a custom software toolbox – uniQC – which provides a general framework to evaluate functional sensitivity. In particular, uniQC combines various visualisation tools with straightforward access to common mathematical and image operations and essential fMRI preprocessing steps in an object-oriented framework. Importantly, the handling of images with arbitrary dimensionality – such as multi-echo or multi-coil images – is inherently provided, and individual processing steps are generalized accordingly. Thus, flexible, yet straightforward evaluation of fMRI data becomes possible.

This thesis provides thorough guidance on the evaluation of functional sensitivity for fMRI, and how acquisition and analysis strategies can be tailored to specific research questions to obtain the best data possible. Utilizing advanced acquisition and analysis techniques to improve functional sensitivity across the whole brain will ultimately facilitate a more comprehensive understanding of human brain function.

Declaration by author

This thesis is composed of my original work, and contains no material previously published or written by another person except where due reference has been made in the text. I have clearly stated the contribution by others to jointly-authored works that I have included in my thesis.

I have clearly stated the contribution of others to my thesis as a whole, including statistical assistance, survey design, data analysis, significant technical procedures, professional editorial advice, financial support and any other original research work used or reported in my thesis. The content of my thesis is the result of work I have carried out since the commencement of my higher degree by research candidature and does not include a substantial part of work that has been submitted to qualify for the award of any other degree or diploma in any university or other tertiary institution. I have clearly stated which parts of my thesis, if any, have been submitted to qualify for another award.

I acknowledge that an electronic copy of my thesis must be lodged with the University Library and, subject to the policy and procedures of The University of Queensland, the thesis be made available for research and study in accordance with the Copyright Act 1968 unless a period of embargo has been approved by the Dean of the Graduate School.

I acknowledge that copyright of all material contained in my thesis resides with the copyright holder(s) of that material. Where appropriate I have obtained copyright permission from the copyright holder to reproduce material in this thesis and have sought permission from co-authors for any jointly authored works included in the thesis.

Publications during candidature

Peer-reviewed papers

Bollmann, S.†, Puckett, A.M.†, Poser, B.A., Palmer, J., Barth, M. †, Cunnington, R. †, 2018. Using multi-echo simultaneous multi-slice (SMS) EPI to improve functional MRI of the subcortical nuclei of the basal ganglia at ultra-high field (7T). NeuroImage 172, 886-895. https://doi.org/10.1016/j.neuroimage.2017.12.005

Bollmann, S., Puckett, A.M., Cunnington, R., Barth, M., 2018. Serial correlations in single-subject fMRI with sub-second TR. NeuroImage 166, 152–166. https://doi.org/10.1016/j.neuroimage.2017.10.043

Puckett, A.M., **Bollmann, S.**, Barth, M., Cunnington, R., 2017. Measuring the effects of attention to individual fingertips in somatosensory cortex using ultra-high field (7T) fMRI. NeuroImage 161, 179–187. https://doi.org/10.1016/j.neuroimage.2017.08.014

Bollmann, S.†, Kasper, L.†, Vannesjo, S.J., Diaconescu, A.O., Dietrich, B.E., Gross, S., Stephan, K.E., Pruessmann, K.P., 2017. Analysis and correction of field fluctuations in fMRI data using field monitoring. NeuroImage 154, 92-105. doi:10.1016/j.neuroimage.2017.01.014

† Indicates shared first/senior authorship.

Conference abstracts (oral presentations are indicated by an underline)

Bollmann, S., Staeb, D., Barth, M., 2018. BOLD fMRI with 0.5 mm isotropic voxel size and minimal in-plane distortion using 3D planes-on-a-paddlewheel (POP) EPI at 7 Tesla. Presented at the 26th Annual Meeting of the International Society for Magnetic Resonance Imaging in Medicine, Paris, France, p708.

Bollmann, S., Kasper, L., Pruessmann, K., Barth, M., Stephan, K.E., 2018. Interactive and flexible quality control in fMRI sequence evaluation: the uniQC toolbox. Presented at the 26th Annual Meeting of the International Society for Magnetic Resonance Imaging in Medicine, Paris, France, p2842.

Bollmann, S., Puckett, A.M., Cunnington, R., Barth, M., 2017. Impact of Physiological Noise on Serial Correlations in Fast Simultaneous Multislice (SMS) EPI at 7T. Presented at the 25th Annual Meeting of the International Society for Magnetic Resonance Imaging in Medicine, Honolulu, US, p5308.

Bollmann, S., Bollmann, S., Puckett, A.M., Janke, A., Barth, M., 2017. Non-linear Realignment Using Minimum Deformation Averaging for Single-subject fMRI at Ultra-high Field. Presented at the 25th Annual Meeting of the International Society for Magnetic Resonance Imaging in Medicine, Honolulu, US, p5338.

Puckett A.M., **Bollmann S.**, Barth M., Cunnington R., 2017. Using SMS multi-echo to improve functional imaging of the cortex and subcortex at 7T. Presented at the 23rd Annual Meeting of the Organization of Human Brain Mapping, Vancouver, Canada, p 4199.

Puckett A.M., **Bollmann S.**, Barth M., Cunnington R., 2017. Exploring somatosensory cortex using ultra-high field (7T) fMRI. Presented at the 7th Australasian Cognitive Neuroscience Society Conference, Adelaide, Australia.

Puckett A.M., **Bollmann S.**, Barth M., Cunnington R., 2016. Measuring the effects of attention to single fingertips using ultra-high field (7T) fMRI. Presented at the 6th Australasian Cognitive Neuroscience Society Conference, New Castle, Australia.

Bollmann, S., Puckett, A.M., Cunnington, R., Barth, M., 2016. Serial correlations in ultra-fast simultaneous multislice (SMS) EPI at 7T. Presented at the Annual Meeting of the European Society for Magnetic Resonance in Medicine and Biology, Vienna, Austria, p334.

Bollmann, S., Puckett, A.M., Poser, B.A., Cunnington, R., Barth, M., 2016. BOLD fMRI in the basal ganglia at 7T using simultaneous multislice (SMS) multi-echo EPI. Presented at the Annual Meeting of the European Society for Magnetic Resonance in Medicine and Biology, Vienna, Austria, p337.

Kasper, L., Diaconescu, A.O., **Bollmann, S.**, Bollmann, S., Pruessmann, K.P., Stephan, K.E., 2016. The Impact of Physiological Noise on Group Level Statistics in fMRI. Presented at the 22nd Annual Meeting of the Organization for Human Brain Mapping, Geneva, Switzerland, p4339.

Puckett, A.M., **Bollmann, S.**, Barth, M., Cunnington, R., 2016. Measuring the effects of attention to single fingertips using ultra-high field (7T) fMRI. Presented at the 22nd Annual Meeting of the Organization for Human Brain Mapping, Geneva, Switzerland, p. 2360.

Bollmann, S., Bednark, J.G., Poser, B.A., Cunnington, R., Barth, M., 2015. Single-Echo vs Multi-Echo Acquisition for Simultaneous Multiband fMRI at 7T in the Basal Ganglia. Presented at the 21st Annual Meeting of the Organization for Human Brain Mapping, Honolulu, USA, p1597.

Kasper, L., Haeberlin, M., **Bollmann, S.**, Vannesjo, S.J., Wilm, B.J., Dietrich, B.E., Gross, S., Stephan, K.E., Pruessmann, K.P., 2015. Matched-filter acquisition of high-resolution single-shot spirals. Presented at the 23rd Annual Meeting of the International Society for Magnetic Resonance Imaging in Medicine, Toronto, Canada, p2060.

Kasper, L., Haeberlin, M., **Bollmann, S.**, Vannesjo, S.J., Wilm, B.J., Dietrich, B.E., Gross, S., Stephan, K.E., Pruessmann, K.P., 2015. Matched-filter acquisition of high-resolution single-shot spirals. Presented at the 21st Annual Meeting of the Organization for Human Brain Mapping, Honolulu, USA, p1649.

Puckett, A.M., **Bollmann, S.**, Barth, M., Cunnington, R., 2015. Functional imaging of basal ganglia at ultra-high field (7T). Presented at the Systems & Computational Neuroscience Down Under Conference, Brisbane, Australia, p66.

Puckett, A.M., Palmer, J., **Bollmann, S.**, Barth, M., Cunnington, R., 2015. Functional imaging of basal ganglia at ultra-high field (7T). Presented at the 5th Australasian Cognitive Neuroscience Society Conference, Auckland, New Zealand, FME004.

Publications included in this thesis

Bollmann, S.†, Puckett, A.M.†, Poser, B.A., Palmer, J., Barth, M. †, Cunnington, R. †, 2017. Using multi-echo simultaneous multi-slice (SMS) EPI to improve functional MRI of the subcortical nuclei of the basal ganglia at ultra-high field (7T). NeuroImage 172, 886-895. https://doi.org/10.1016/j.neuroimage.2017.12.005

† Indicates shared first/senior authorship.

This publication was incorporated in Chapter 2.

Contributor	Statement of contribution
Bollmann, S. (Candidate)	Conception and design (40 %) Data acquisition (25 %) Analysis and interpretation (35 %) Drafting and production (45 %)
Puckett, A.M.	Conception and design (40 %) Data acquisition (25 %) Analysis and interpretation (35 %) Drafting and production (45 %)
Poser, B.A.	Conception and design (0 %) Data acquisition (25 %) Analysis and interpretation (5 %) Drafting and production (0 %)
Palmer, J.	Conception and design (0 %) Data acquisition (25 %) Analysis and interpretation (15 %) Drafting and production (0 %)
Barth, M.	Conception and design (10 %) Data acquisition (0 %) Analysis and interpretation (5 %) Drafting and production (5 %)
Cunnington, R.	Conception and design (10 %) Data acquisition (0 %) Analysis and interpretation (5 %) Drafting and production (5 %)

Bollmann, S., Puckett, A.M., Cunnington, R., Barth, M., 2018. Serial correlations in single-subject fMRI with sub-second TR. NeuroImage 166, 152–166. https://doi.org/10.1016/j.neuroimage.2017.10.043

This publication was incorporated in Chapter 3.

Contributor	Statement of contribution
Bollmann, S. (Candidate)	Conception and design (80 %) Data acquisition (50 %) Analysis and interpretation (90 %) Drafting and production (70 %)
Puckett, A.M.	Conception and design (0 %) Data acquisition (50 %) Analysis and interpretation (5 %) Drafting and production (10 %)
Cunnington, R.	Conception and design (10 %) Data acquisition (0 %) Analysis and interpretation (0 %) Drafting and production (10 %)
Barth, M.	Conception and design (10 %) Data acquisition (0 %) Analysis and interpretation (5 %) Drafting and production (10 %)

Contributions by others to the thesis

I would like to thank my co-authors for their invaluable input and support during the preparation of this thesis. In particular, I would like to thank Alex Puckett and Markus Barth for their contributions not only to the individual projects, but also their generous feedback during the overall conception of this document. Further, I would like to thank Lars Kasper, Klaas P. Pruessmann, and Klaas E. Stephan for their continuing encouragement during the development of uniQC.

Statement of parts of the thesis submitted to qualify for the award of another degree

None

Research Involving Human or Animal Subjects

The research presented in this thesis was approved by the Medical Research Ethics Committee at the University of Queensland (Project Number: 2011001394). The corresponding ethics approval letter is included in the appendix.

Acknowledgements

I thank Aiman Al-Najjar, Nicole Atcheson, and Steffen Bollmann for help with data collection. I thank Steve Cauley for providing a multi-echo enabled variant of the MGH slice-GRAPPA reconstruction and Himanshu Bath for details on the sequence-recon interface. I thank Will Penny for valuable comments on the VB algorithm and the estimation and interpretation of the frequency response of the AR models.

Financial support

This research was supported by an Australian Government Research Training Program Scholarship, the National Health and Medical Research Council (APP 1088419) and the Australian Research Council Future Fellowship grant FT140100865. Further, the support of the National Imaging Facility (NIF) at the Centre for Advanced Imaging, University of Queensland is acknowledged.

Keywords

functional MRI, simultaneous multi-slice, autocorrelation, physiological noise, multi-echo, motor, variational Bayes, EPI, susceptibility artefacts, signal loss, echo time, basal ganglia, sequence development, quality control, image quality, SPM, MATLAB, time series analysis, BOLD sensitivity, functional sensitivity

Australian and New Zealand Standard Research Classifications (ANZSRC)

ANZSRC code: 110903 Central Nervous System 70 %

ANZSRC code : 090303, Biomedical Instrumentation 20 %

ANZSRC code : 010404 Probability Theory 10 %

Fields of Research (FoR) Classification

FoR code: 1109 Neurosciences 70 %

FoR code: 0903 Biomedical Engineering 20 %

FoR code: 0104 Statistics 10 %

Dedications

I have been extremely fortunate to meet numerous wonderful people during my (scientific) journey. In particular, I would like to thank

… my mum. *Liebe Mutti, danke, dass du mich neugierig gemacht hast auf die Welt und mir das Selbstvertrauen gegeben hast, sie zu erkunden.*

… my dad and Rosi. *Liebe Rosi und lieber Papa, danke, dass ihr mit beigebracht habt immer den Blick auf's Wesentliche zu richten.*

… Steffen. *Mein Schatz*, thanks for sharing the last 10 years, 6 months and 5 days with me. You are the patience to my eagerness, and the chaos to my order. Thank you for keeping my mind sharp and my heart happy.

… Lars. *Lieber Lars*, sic! I'm so proud that our friendship and scientific partnership keeps growing despite all the kilometres between us. Thank you for sharing your passion for science with me.

… Christine. Thank you for making me more excited about the brain than ever.

… Markus. Thank you for giving me the opportunity to come to Brisbane; I couldn't image a better place or a better supervisor. Thank you for your patience, and for supporting me to follow my own ideas.

… Alex. Our joint scanning sessions are certainly one of the more memorable experiences - thanks for hanging in there. You have been a wonderful colleague and a great friend, and I can't appreciate enough your help with sorting out my thoughts and making my writing flow.

… Ben, Jake and Ross. Thanks for stepping in whenever the multi-echo project got stuck.

… Nicole, Aiman, Alan, Dave, Don, Lorine, Lesley and everyone else behind the scenes. Thank you so much for your support, last-minute equipment repairs and for always keeping the spirit high.

… Daniel, Kieran, Fabian, Judith, Marge, Aurelien, Kiran, Marco, Tom, Atena, Shahrokh and everyone else in the 7T group. The shared laughs, cakes and coffees are a major contributor to this thesis.

… Viktor and Martha. Thank you for the encouragement, and the critical questions during my milestones.

… everyone else at the Centre for Advanced Imaging. Thank you for making me feel welcome, and for explaining the Australian way of life to me.

Further, I would like to thank all the participants who spend a long time in the scanner and helped us to acquire such beautiful data.

To finish, I would like to thank the reviewers for their time and effort.

Table of Contents

Chapter 1 Introduction 26

1.1 Aims and objectives 29

1.2 Functional magnetic resonance imaging 29

1.2.1 Overview 29

1.2.2 Contrast mechanisms in fMRI 29

1.2.3 BOLD contrast and the hemodynamic response function 30

1.2.4 Image encoding in fMRI 31

1.2.5 The general linear model 33

1.2.6 Further reading 33

1.3 Definition of functional sensitivity 34

1.3.1 BOLD sensitivity 34

1.3.2 Spatial specificity 35

1.4 Impact of acquisition parameters and statistical modelling on functional sensitivity 37

1.4.1 Field strength 37

1.4.2 Acquisition strategies 37

1.4.3 Noise reduction in fMRI 39

1.5 Evaluating functional sensitivity 39

1.6 Outline of the thesis 41

Chapter 2 Using multi-echo simultaneous multi-slice (SMS) EPI to improve functional MRI of the subcortical nuclei of the basal ganglia at ultra-high field (7T) 44

2.1 Introduction 47

2.2 Theory 48

2.2.1 Multi-echo imaging for fMRI 48

2.2.2 Motor cortex and basal ganglia 50

2.3 Methods 50

2.3.1 Participants 50

2.3.2 Experimental design....51
2.3.3 Magnetic resonance imaging data acquisition....53
2.3.4 Preprocessing....54
2.3.5 Single-subject analysis....54
2.3.6 Group analysis....55
2.4 Results and discussion....56
2.4.1 tSNR in a single subject....56
2.4.2 Group statistical parametric mapping....58
2.4.3 Comparing activation parameters....60
2.4.4 Relationship of sensitivity gains to T2*....61
2.5 Conclusions and recommendations....62
2.6 Acknowledgements....64
2.7 Appendix A. Supplementary data....64
Chapter 3 Serial correlations in single-subject fMRI with sub-second TR....68
3.1 Introduction....71
3.2 Materials and Methods....73
3.2.1 Data acquisition....73
3.2.2 Study design....74
3.2.3 Preprocessing....75
3.2.4 Physiological noise modelling....75
3.2.5 Model estimation and analysis....76
3.3 Results....78
3.3.1 Optimal AR model orders and the impact of physiological noise modelling....78
3.3.2 Bayes factor analysis....84
3.3.3 AR coefficient analysis....85
3.3.4 Noise spectrum and FAST for pre-whitening....87
3.3.5 Impact of smoothing....89
3.4 Discussion....90

3.4.1 Effect of TR and physiological noise on optimal AR model order 90
3.4.2 Implications for error modelling in statistical inference 91
3.4.3 Limitations and considerations 93
3.5 Conclusion 93
3.6 Acknowledgements 93
Chapter 4 Interactive and flexible MRI data evaluation: the uniQC toolbox 96
4.1 Introduction 99
4.2 Methods 101
4.2.1 Overview 101
4.2.2 MrImage 103
4.2.3 MrSeries 105
4.2.4 Class structure 105
4.2.5 File management 111
4.2.6 Integration with SPM 113
4.2.7 Unit testing 114
4.2.8 Coding conventions 114
4.2.9 Example data 114
4.3 Results 115
4.3.1 Example Use Cases 115
4.3.2 Visualisation tools 115
4.3.3 Image operations 116
4.3.4 Quality control pipeline for fMRI data 118
4.3.5 Extension to n-dimensional data sets 120
4.3.6 Demos overview 121
4.4 Discussion and conclusion 123
4.4.1 Summary 123
4.4.2 Comparison to other fMRI analysis software 123
4.4.3 Limitations and Outlook 126

4.5 Software note....126
4.6 Acknowledgements....126
Chapter 5 Discussion and Conclusion....128
5.1 Summary....131
5.2 Advanced pre-whitening schemes for single-subject fMRI....132
5.3 T-score testing for the mean as a measure of functional sensitivity....132
5.4 Implications for group-level inference....133
5.5 The impact of spatial specificity on statistical power....134
5.6 Outlook....135

List of Figures & Tables

Figure 1-1: Illustration of the hemodynamic response function 31
Figure 1-2: Illustration of a 2D k-space. 32
Figure 2-1: Experiment overview. 52
Figure 2-2: tSNR maps. 57
Figure 2-3: Group activation maps. 59
Figure 2-4: Group activation parameters. 60
Figure 2-5: Improvement in *t*-statistic across brain regions. 62
Figure 3-1: Estimated optimal AR model orders for the short-TR sequence 79
Figure 3-2: Distribution of optimal AR model orders. 80
Figure 3-3: Estimated optimal AR model orders for the long TR sequence. 82
Figure 3-4: Distribution of optimal AR model orders. 83
Figure 3-5: Log Bayes Factor 84
Figure 3-6: Spectrum of AR models. 85
Figure 3-7: AR coefficient maps 86
Figure 3-8: Average spectrum of the residual image time series 88
Figure 3-9: Average spectrum of the residual image time series 89
Figure 3-10: Estimated optimal AR model orders for the short-TR sequence 90
Figure 4-1: Overview of `MrImage` and `MrSeries`. 102
Figure 4-2: Properties and methods of the `MrImage` class. 104
Figure 4-3: Properties and methods of the `MrSeries` class. 105
Figure 4-4: Properties defining `MrDimInfo` 108
Figure 4-5: Constructor of `MrDimInfo` 109
Figure 4-6: Plot operations for MrImage 116
Figure 4-7: Illustration and code for algebraic matrix and image operations 117
Figure 4-8: Illustration of `MrSeries` for quality control 119
Figure 4-9: Application stages and corresponding software requirements 125
Figure S1: Group activation maps complex movement 64
Figure S2: Group activation maps simple movement 65
Figure S3: Functionally-defined ROIs 65
Table 4-1: Overview of uniQC classes 106
Table 4-2: Overview of `MrGlm` properties 112
Table 4-3: Overview of Scenarios 120

List of Abbreviations used in the thesis

AR	autoregressive
BOLD	blood oxygen level dependent
CN	caudate nucleus
CNR	contrast-to-noise ratio
CRF	cardiac response function
CSF	cerebrospinal fluid
EPI	echo-planar imaging
FA	flip angle
FDR	false discovery rate
fMRI	functional magnetic resonance imaging
FOV	field-of-view
FWHM	full-width-at-half-maximum
GE-EPI	gradient-echo echo-planar-imaging
GLM	general linear model
GM	grey matter
GRE	gradient-recalled echo
HRF	hemodynamic response function
MRI	magnetic resonance imaging
M1	primary motor cortex
PCA	principal component analysis
PSF	point spread function
PUT	putamen
ReML	restricted maximum likelihood
RF	radio frequency
ROI	region-of-interest
RRF	respiration response function
SD	standard deviation
SMA	supplementary motor cortex
SMS	simultaneous multi-slice
SNR	signal-to-noise ratio
SPM	statistical parametric mapping
T	Tesla

TE	echo time
TI	inversion time
TPM	tissue probability map
TR	repetition time
tSNR	temporal signal-to-noise ratio
QC	quality control
uniQC	unified neuroimaging quality control
VB	variational Bayes
VST	ventral striatum
WM	white matter

Chapter 1

Introduction

1.1 Aims and objectives

Functional magnetic resonance imaging (fMRI) enables the non-invasive investigation of human brain function. New data acquisition techniques for fMRI are continuously developed to increase image resolution, acquisition speed and contrast. The ultimate goal is to maximize functional sensitivity, i.e. the ability to detect and localise neurovascular activity using fMRI. Given the overwhelming number of parameters that need to be selected to compile an fMRI acquisition protocol, and their complex influences on image fidelity and contrast, ascertaining functional sensitivity is fundamental for every fMRI experiment. Here, I will discuss key constituents of functional sensitivity, provide an overview of the impact of fMRI acquisition parameters, and outline relevant evaluation measures. In Chapter 2, I will examine functional sensitivity for multi-echo fMRI – a new class of data acquisition techniques. Subsequently in Chapter 3, I will investigate the effect of increased acquisition speed on serial correlations, and how this can affect estimates of functional sensitivity. In Chapter 4, I will present uniQC - a computational framework implemented as a MATLAB toolbox to perform interactive, flexible and comprehensive evaluation of functional sensitivity.

1.2 Functional magnetic resonance imaging

1.2.1 Overview

In an fMRI experiment, magnetic resonance imaging (MRI) is utilized to acquire a time series of images reflecting neuronal activity. More precisely, changes in image intensity over time depict local changes in brain physiology, indicative of neuronal activity. To then infer on the location of neuronal activity, statistical analysis is performed on the image time series. In the following, key concepts of MRI, the physiological basis of the employed contrast mechanism and the statistical analysis are briefly revisited to initialize the discussion of functional sensitivity. For the interested reader, a guide to detailed literature is given at the end of this brief summary.

1.2.2 Contrast mechanisms in fMRI

MRI utilizes the principles of nuclear magnetic resonance for signal and contrast generation. The image contrast is governed by the relaxation times and the timing of the employed acquisition protocol (= sequence). The longitudinal relaxation time T_1 describes the rate of regrowth to the equilibrium magnetisation after the application of a radio-frequency (RF) pulse (Brown et al., 2014a). The T_1 value of cortical grey matter at a main magnetic (B_0) field strength of 7 Tesla (T) is estimated at approximately 1940 ms, but pronounced differences

between measurement methods and brain regions have been observed (Wright et al., 2008). In fMRI, the repeated excitation of the same spins can introduce unwanted intensity fluctuations due to T_1 relaxation. To overcome this, the Ernst angle α_{Ernst} can be used, which provides maximal available signal given the repetition time (TR) and the longitudinal relaxation time T_1 (Brown et al., 2014b):

$$\alpha_{Ernst} = \arccos\left(\exp\left(-\frac{TR}{T_1}\right)\right). \quad (1)$$

The transverse relaxation times T_2 and T_2^* describe the dephasing of the transverse magnetization. T_2 characterizes irreversible spin-spin interaction, and T_2^* additionally contains contributions from local field inhomogeneities. In fMRI, T_2^*-weighted images using a gradient recalled echo (GRE) sequence are commonly employed, because they provide higher sensitivity and efficiency compared to the T_2-weighted images produced by spin-echo acquisitions (Boyacioğlu et al., 2014). However, spin-echo fMRI has the potential to provide better sensitivity to micro-vasculature (Yacoub et al., 2003). The T_2^* in cortical grey matter at 7T has been estimated at approximately 33 ms, but shorter T_2^* values have been observed in subcortical nuclei such as the caudate (20 ms) and putamen (16 ms) (Peters et al., 2007). The signal model to characterize the impact of the effective transverse relaxation time T_2^* on the image intensity I reads

$$I \propto \rho \cdot \exp\left(-\frac{TE}{T_2^*}\right). \quad (2)$$

where ρ is the spin density and TE is the echo time. Consequently, a change in T_2^* can be observed as a change in image intensity I.

1.2.3 BOLD contrast and the hemodynamic response function

The fluctuations in image intensity reflect neuronal activity based on two mechanisms. First, the hemodynamic response (Buxton et al., 1998) causes an increase in the ratio of oxygenated to de-oxygenated blood following neuronal activity (Bandettini et al., 1992; Kwong et al., 1992; Ogawa et al., 1992). This net decrease of the amount of de-oxygenated blood (Fox and Raichle, 1986; Malonek et al., 1997) is induced by an increase of blood flow followed by blood volume changes (Hoge et al., 1999). Although the contrast mechanism used in fMRI is based on changes in blood oxygenation, the hemodynamic response itself is mainly driven by neurotransmitter signalling, most notably glutamate (Attwell and Iadecola, 2002). In combination with the large number of neurons contained in one voxel (100 000 neurons in 1µl or 1 mm^3 of grey matter), inference on the underlying neuronal

processes remains challenging (Logothetis, 2008). In general, the hemodynamic response is seen as a reflection of input and intracortical processing rather than spiking output (Logothetis et al., 2001).

The level of blood oxygenation affects the local effective transverse relaxation time T_2^* because deoxygenated hemoglobin is paramagnetic (Ogawa et al., 1990). Following the net increase in oxygenated blood, an increase in T_2^* can be observed, resulting in an intensity increase in T_2^*-weighted images. This contrast mechanism is termed blood oxygenation level dependent (BOLD) contrast. Note that this definition of contrast generation neglects inflow effects, which can be substantial under certain conditions (Duyn et al., 1994).

The hemodynamic response function (HRF) (Glover, 1999a) was introduced to model the expected signal change following a stimulus (Figure 1-1). Characteristic timings of the HRF are the delay of the response (6 s) and the delay of the undershoot (16 s) (Glover, 1999a). In the statistical analysis, the HRF is then used to model the expected signal time course.

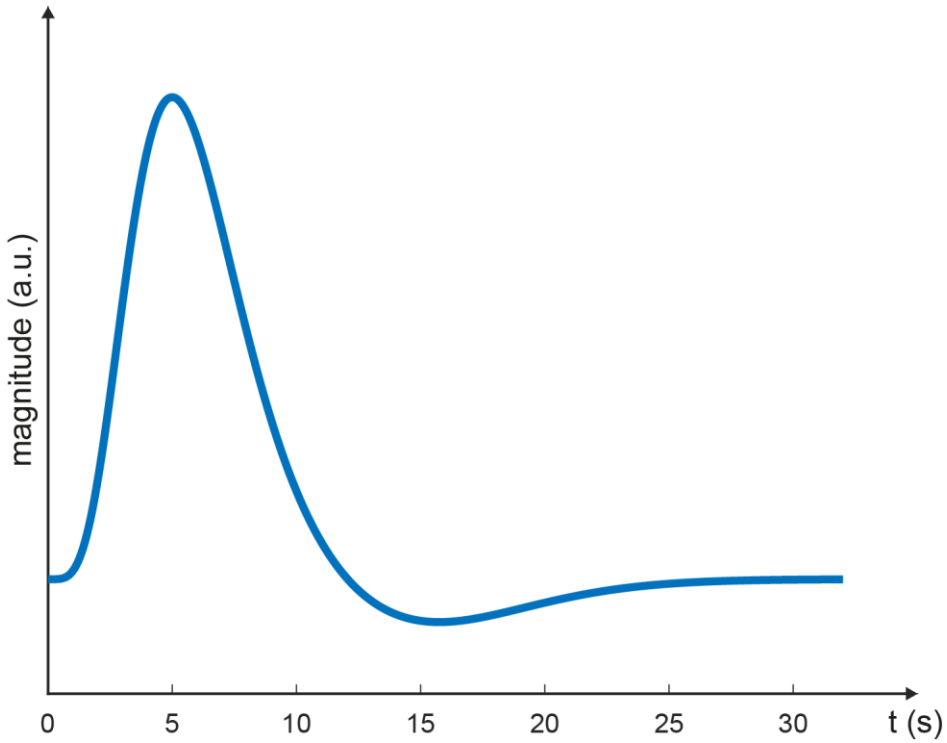

Figure 1-1: Illustration of the hemodynamic response function (HRF). Following a stimulus at time 0, a delayed signal increase can be observed lasting several seconds. Return to baseline conditions can take up to 30 seconds.

1.2.4 Image encoding in fMRI

To form an image, i.e. to localize the change in T_2^*, spatial encoding of the object needs to be performed. Image encoding in MRI is enabled through the application of external, temporally-varying gradient fields $G(t)$. Thus, the location of the spin density $\rho(\vec{r})$ is encoded

through the introduction of a complex phase term (eq. (3)). The resulting signal $s(t)$ obtained in a receiver coil from an imaging volume V then reads

$$s(t) \approx \int_V \rho(\vec{r}) \cdot \exp(-i2\pi\vec{k}(t) \cdot \vec{r})\, d\vec{r}. \quad (3)$$

Image encoding is best visualised in k-space, which expresses the signal in terms of a Fourier transform of the spin density. The k-space trajectory describes the sampling pattern within that k-space (Figure 1-2). In fMRI, echo-planar imaging (EPI) (Mansfield, 1984) is commonly employed to enable fast image acquisition. Therein, a 2D k-space $(k_x(t), k_y(t))$

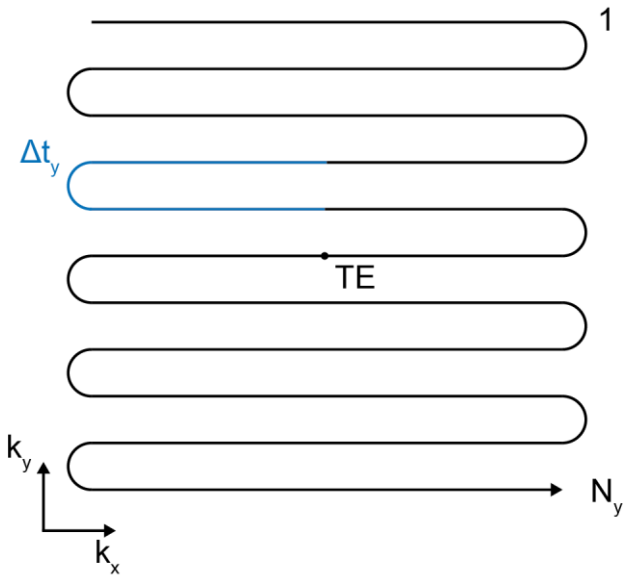

Figure 1-2: Illustration of a 2D k-space. The echo-time is defined as the time when the centre of k-space is sampled. The number of k-space lines is indicated by N_y, and the echo spacing Δk_y is the time between two consecutive echoes.

is read out after one RF excitation by temporally varying the external gradient fields $G(t)$:

$$\begin{aligned} k_x(t) &= \gamma \int_0^t G_x(t')dt' \,, \\ k_y(t) &= \gamma \int_0^t G_y(t')dt'. \end{aligned} \quad (4)$$

Given a sufficient k-space coverage, the reconstructed image $\hat{\rho}(\vec{r})$ can then be estimated via an inverse Fourier transform of the measured signal $s(t)$ (Brown et al., 2014c). Using a GRE EPI readout, the final image intensity I is then also weighted by transverse relaxation time T_2^* (eq. (2)). This provides the basis for the fast acquisition of a T_2^*-weighted image time series for fMRI. This image time series is then analysed to infer on the location of stimulus induced signal changes, and, thereby, neuronal activity.

1.2.5 The general linear model

The general linear model (GLM) expresses the image intensity values Y[1] acquired over time as a combination of the design matrix X describing the experimental manipulations, the (unknown) parameters β and a random error e following a normal distribution with variance σ^2 (Kiebel and Holmes, 2007):

$$Y = X\beta + e. \tag{5}$$

The design matrix comprises the expected signal, which is estimated by convolving the HRF with a vector containing the timing of the experimental manipulation. The β parameters are then estimated at each voxel and statistical inference is performed to identify those voxel where the measured signal resembles the expected signal. For this purpose, a t-value can be computed from the parameter estimates $\hat{\beta}$ and their variance $Var(\hat{\beta})$:

$$T = \frac{c^T\hat{\beta}}{\sqrt{Var(c^T\hat{\beta})}}, \tag{6}$$

where the contrast vector c encodes the model parameters of interest. The variance of the parameter estimates depends on the residual variance $\hat{\sigma}^2$ and the design matrix:

$$T = \frac{c^T\hat{\beta}}{\sqrt{\hat{\sigma}^2 c^T(X^TX)^{-1}c}}. \tag{7}$$

The residual variance estimate $\hat{\sigma}^2$ is obtained from the error e and the $J - p$ degrees of freedom, with J being the number of observations and $p = rank(X)$:

$$\hat{\sigma}^2 = \frac{e^Te}{J-p}. \tag{8}$$

The resulting statistical map is then thresholded to identify those locations with high t-scores, i.e. good congruency between measured and modelled signal and low noise levels.

1.2.6 Further reading

For the interested reader, an excellent introduction to fMRI can be found in *Functional magnetic resonance imaging* (Huettel et al., 2008), and more personal reviews in *20 Years of fMRI* (Bandettini, 2012). A general discussion of MRI is presented in *Magnetic Resonance Imaging: Physical Principles and Sequence Design* (Brown et al., 2014d). Detailed information on nuclear magnetic resonance and on pulse sequences are provided in *Principles of Nuclear Magnetism* (Abragam, 1983) and the *Handbook of MRI Pulse Sequences* (Bernstein, 2005), respectively. An overview of current developments in image

[1] The change in notation from I to Y represents the transition from the field of MRI to the field of statistical parametric mapping (SPM).

acquisition for (f)MRI is compiled in *Neuroimaging with Ultra-high Field MRI: Present and Future* (Polimeni and Uludag, 2018) and *Pushing the spatio-temporal limits of MRI and fMRI* (Yacoub and Wald, 2018). The foundations of the statistical analysis of fMRI data and advanced modelling strategies are outlined in *Statistical Parametric Mapping: The Analysis of Functional Brain Images* (Friston et al., 2006). Specific details of noise correction methods for fMRI are discussed in *Cleaning up the fMRI time series: Mitigating noise with advanced acquisition and correction strategies* (Murphy and Bright, 2017). Latest insights into brain physiology and organisation are summarized in *Functional architecture of the human brain* (Van Den Heuvel et al., 2017).

1.3 Definition of functional sensitivity

1.3.1 BOLD sensitivity

In an fMRI experiment, an image time series is acquired depicting fluctuations in the image intensity over time. These image fluctuation reflect neuronal activity over time across a large number of locations (voxels) simultaneously. When evaluating functional sensitivity, this spatio-temporal nature of the fMRI data needs to be considered.

The temporal properties of functional sensitivity can be assessed using the definition of BOLD sensitivity (S_{BOLD}) as introduced by Deichmann et al. (2002) and Posse et al. (1999). Therein, BOLD sensitivity is defined as the change in image intensity ΔI given a change in T_2^*:

$$S_{BOLD} = \Delta I|_{T_2^* \to T_2^* + \Delta T_2^*}. \quad (9)^2$$

To find the echo time that maximizes BOLD sensitivity, equation (9) is simplified using equation (2) and a first order Taylor expansion (Deichmann et al., 2002; Posse et al., 1999) or differential (Poser et al., 2006) to

$$S_{BOLD} = I \cdot TE, \quad (10)$$

which reaches its maximum at

$$TE = T_2^*. \quad (11)$$

To incorporate subsequent developments in image acquisition and analysis, this definition of BOLD sensitivity has been extended further. Following the introduction of the GLM to the

[2] Note that equation (9) is usually stated in the form $S_{BOLD} = \Delta I \backslash \Delta T_2^*$ (Deichmann et al., 2002; Poser et al., 2006; Posse et al., 1999). However, ΔI is a function of ΔT_2^* (2), prohibiting the optimization of *individual* parameters. Thus, this slight adjustment has been made to only include independent parameters in the definition of BOLD sensitivity. Nevertheless, the mechanism of the signal genesis, i.e. the change of T_2^* to $T_2^* + \Delta T_2^*$, is still expressed.

analysis of fMRI data (Friston et al., 1994), the standard deviation σ_{time} of the temporal noise has been included (eq. (8)) (Poser et al., 2006):

$$S_{BOLD} = \frac{\Delta I|_{T_2^* \to T_2^* + \Delta T_2^*}}{\sigma_{time}}. \quad (12)$$

The temporal noise σ_{time} consists of thermal noise $\sigma_{thermal}$, low frequency drifts and other system noise σ_{system}, physiological noise $\sigma_{physiology}$, i.e. fluctuations related to cardiac and respiratory activity, un-modelled neuronal activity $\sigma_{neuronal}$ and motion σ_{motion} (Bianciardi et al., 2009; Friston et al., 1996, for a recent review see Liu, 2016). The overall temporal noise σ_{time} is given by (Krüger and Glover, 2001)

$$\sigma_{time} = \sqrt{\sigma_{thermal}^2 + \sigma_{system}^2 + \sigma_{physiology}^2 + \sigma_{neuronal}^2 + \sigma_{motion}^2}. \quad (13)$$

Note the lower bound that is imposed on σ_{time}, which is the maximum of the individual noise components. As a consequence, a reduction in thermal noise does not necessarily result in a reduction of temporal noise, if other noise sources, such as physiological noise, are considerably stronger (Triantafyllou et al., 2005).

The second extension to the definition of BOLD sensitivity followed the introduction of simultaneous multi-slice (SMS) imaging (Breuer et al., 2005; Larkman et al., 2001) to fMRI (Feinberg et al., 2010; Setsompop et al., 2012), providing a considerable gain in acquisition speed. Accordingly, the number of samples N that can be acquired per unit time increases, reducing the variance of the parameter estimates in the statistical analysis (Kasper, 2014; Kiebel and Holmes, 2007, eq. (7)). Hence, the definition of BOLD sensitivity has been extended further to incorporate the number of samples (Barth and Poser, 2011):

$$S_{BOLD} = \frac{\Delta I|_{T_2^* \to T_2^* + \Delta T_2^*} \cdot \sqrt{N}}{\sigma_{time}}. \quad (14)$$

The number of samples N can also be replaced by the inverse of the repetition time providing BOLD sensitivity per unit time. In summary, BOLD sensitivity can be increased by (i) a larger change in image intensity for a given ΔT_2^*, (ii) a larger ΔT_2^* for a given neuronal activity, (iii) a reduction in noise and (iv) a higher number of samples.

1.3.2 Spatial specificity

The second aspect when evaluating functional sensitivity concerns the spatial domain of the fMRI data, i.e. the spatial specificity. Spatial specificity describes the ability to locate and differentiate sites of neuronal activation. First investigations of the physiologically imposed lower bound on spatial specificity estimated the point spread function (PSF) of the BOLD response to be below 2 mm for fMRI at 7T (Shmuel et al., 2007). However, new empirical evidence (Koopmans et al., 2010; Shi et al., 2017) and the development of specific analysis

strategies for high-resolution fMRI data (Polimeni et al., 2017) have challenged these initial findings. Currently, a trend towards imaging of structures as small as cortical laminae and columns (< 0.5 mm, Mountcastle et al., 1955) can be observed (Chaimow et al., 2018; Lawrence et al., 2017; Nasr et al., 2016; Stephan et al., 2017a). This becomes possible because the underlying tissue microstructure (Uludağ et al., 2009) and the stimulus timing (Sheth, 2004) are important components shaping the BOLD PSF. Equivalently, the image acquisition also determines spatial specificity, which can be described by an image PSF (Robson et al., 1997).

Furthermore, the statistical analysis following the image acquisition additionally impacts the spatial specificity. In classical statistics using the GLM, random field theory (Worsley, 2007) is applied to overcome the multiple comparison problem and perform statistical inference. Therein, two mechanism determine the spatial specificity of the obtained statistical map. The first is the required smoothness (Friston, 2007a; Nichols and Hayasaka, 2003), which is often assured by spatially smoothing the images during preprocessing, significantly reducing the spatial specificity. Recommendations for the full width at half maximum (FWHM) of the necessary smoothness can be as high as 6 voxel FWHM (Nichols and Hayasaka, 2003). Second, the chosen topological feature, i.e. peaks, clusters or excursion sets, also determine the spatial specificity (Friston, 2007a). Peak (or voxel) - level inference is based on the height of the peak, giving it the highest localising power. Cluster-level inference utilizes the spatial extent of a cluster, providing less localising power but more sensitivity. Ultimately, set-level inference has the highest sensitivity, because it basically tests the statistical map as a whole, but is rarely used due to its very low spatial specificity. However, the loss in spatial specificity through smoothing and cluster-level inference provides a much needed increase in statistical power to detect activation and was certainly enabling in the wide-spread application of fMRI (Nichols and Hayasaka, 2003).

To illustrate the interplay between the different mechanisms governing spatial specificity, one could assume Gaussian kernels as the PSFs of the individual components. Then, the overall spatial specificity can be expressed in terms of the standard deviation of a Gaussian kernel σ_{space} as

$$\sigma_{space} = \sqrt{\sigma_{MRI}^2 + \sigma_{BOLD}^2 + \sigma_{smoothing}^2 + \sigma_{distortions}^2}. \quad (15)$$

containing the contributions from the imaging process σ_{MRI}, the BOLD response σ_{BOLD}, spatial smoothing $\sigma_{smoothing}$ and distortions $\sigma_{distortions}$. The distortions are introduced through the sensitivity of EPI to inhomogeneities in the main magnetic field, leading to voxel mislocations (Hutton et al., 2002). These voxel mislocations can cause a mismatch between

the fMRI and an anatomical reference image, impeding the reliable identification of a site of activation (Brett et al., 2002). Similarly as for the temporal noise, a lower bound is imposed on σ_{space}, which is limited to the largest width of the individual components. Hence, an increase in image resolutions needs to be accompanied by an appropriate statistical analysis to improve overall spatial specificity.

In summary, functional sensitivity depends on the sensitivity within a voxel to detect a signal change (BOLD sensitivity) and the ability to accurately locate this signal change (spatial specificity). Since one can be traded in for the other, both need to be assessed when evaluating functional sensitivity. Ultimately, the image acquisition can be tailored to the image analysis a priori (Kasper et al., 2014), increasing overall functional sensitivity.

1.4 Impact of acquisition parameters and statistical modelling on functional sensitivity

1.4.1 Field strength

MRI technology and sequences are continuously developed, allowing the researcher to select from a wide range of acquisition options. Due to the large number of interdependent parameters with different (and often opposing) effects on functional sensitivity, a compromise needs to be found optimizing both BOLD sensitivity and spatial specificity for a specific research question.

The most widespread improvement in functional sensitivity can be achieved through an increase in field strength. The image signal-to-noise ratio (SNR) for a given voxel volume increases linearly (Edelstein et al., 1986) or supralinearly (Pohmann et al., 2016) with field strength. Thus, the maximally achievable temporal SNR (tSNR) also increases, which is determined by thermal noise only (Krüger and Glover, 2001). Additionally, the BOLD contrast increases through both an increase in ΔI for a given ΔT_2^* (Gati et al., 1997; Okada et al., 2005) and an increase in ΔT_2^* for a given stimulus (van der Zwaag et al., 2009) (eq. (14)). Spatial specificity can be increased by utilizing the increased image SNR to increase the spatial resolution (σ_{MRI}^2). Furthermore, contributions from draining veins are reduced at higher field strength (Boxerman et al., 1995; Gati et al., 1997; Uludağ et al., 2009) decreasing the BOLD PSF (σ_{BOLD}^2) (Shmuel et al., 2007).

1.4.2 Acquisition strategies

New sequence and reconstruction methods have enabled an increase in image acquisition speed providing more samples N per unit time, increasing BOLD sensitivity (eq. (14)) . EPI

can be seen as an enabling technique for fMRI, allowing the acquisition of a single image slice in tens of milliseconds and, accordingly, the acquisition of a whole image volume in a few seconds. However, GRE EPI is sensitive to image distortions and signal loss (Jezzard and Clare, 1999). Inhomogeneities in the B_0 - field cause additional phase contributions mostly along the phase encoding direction, effectively introducing a voxel mislocation ($\sigma^2_{distortions}$), and degrading spatial specificity (eq. (15)). The voxel displacement Δy in the phase encoding direction is given by (Jezzard and Clare, 1999)

$$\Delta y = \frac{\Delta \nu(y)}{BW_{PE}}, \tag{16}$$

where $\Delta \nu(y)$ is the spatial distribution of the frequency offset and BW_{PE} is the bandwidth per voxel in the phase encoding direction. The bandwidth per voxel corresponds to the frequency offset that would cause a voxel displacement of exactly one voxel length (Polimeni et al., 2017). An alternative formulation using the echo spacing Δt_y and the number of (acquired) phase encoding steps N_y (Figure 1-2) is given by (Holland et al., 2010):

$$\Delta y = \Delta \nu(y) \cdot \Delta t_y \cdot N_y. \tag{17}$$

Additionally, signal loss can be caused by through-plane dephasing, which occurs in areas with strong susceptibility differences, for example at air-tissue interfaces. Therein, a strong susceptibility gradient in the slice direction introduces an additional decay term in equation (2), leading to a much faster signal dephasing (Volz et al., 2009). A number of methods have been put forward to counteract distortions and signal loss in EPI. Their aim is to either counteract the frequency offset $\Delta \nu(y)$, reduce the sensitivity of the acquisition to field inhomogeneities by minimizing Δt_y or N_y, or correct for the voxel displacement Δy.

The most commonly applied measure to minimize $\Delta \nu(y)$ is B_0 shimming (Balteau et al., 2010), where shim coils are used to produce magnetic fields counteracting B_0 inhomogeneities. Signal loss in areas with remaining inhomogeneities can then be further reduced through slice-specific z-shimming (Glover, 1999b; Schneider et al., 2015). Additional improvement can be obtained through an appropriate choice of a number of sequence parameters, such as slice-tilt and phase-encoding direction (De Panfilis and Schwarzbauer, 2005; Speck et al., 2008; Weiskopf et al., 2006), slice thickness (Poser et al., 2006; Robinson et al., 2004), resolution (Robinson et al., 2008; Weiskopf et al., 2007) and echo time (Poser and Norris, 2009; Stocker et al., 2006, but cf. Gorno-Tempini et al., 2002). Retrospective correction techniques utilize field maps to correct the voxel displacement Δy either in k-space (Man et al., 1997) or in image-space (Hutton et al., 2002; Jezzard and Clare, 1999).

The development of receive arrays has enabled parallel imaging (Griswold et al., 2002; Pruessmann et al., 1999), providing a decrease in the number of phase encoding steps N_y by an acceleration factor R, which can considerably reduce distortions (Poser et al., 2006). Further, the length of the readout train, and, hence, the repetition time can be shortened, allowing the acquisition of an increased number of samples N per unit time. Additionally, the reduction in the readout train length significantly reduces the echo time, allowing either shorter echo times or higher image resolution with the same echo time. Because T_2^* values decrease with field strength (Peters et al., 2007), the optimality criterion in equation (11) imposes shorter echo times for higher field strength. Hence, parallel imaging enables optimal BOLD sensitivity for high-resolution fMRI at ultra-high field. Disadvantages are the decrease in image SNR by a factor of $\sqrt{R}$, and the spatially varying noise amplification due to the ill-conditioning of the image reconstruction problem (Pruessmann et al., 1999). Additionally, SMS imaging (Breuer et al., 2005; Feinberg et al., 2010; Larkman et al., 2001; Setsompop et al., 2012) provides a dramatic increase in acquisition speed at little cost of image SNR (Moeller et al., 2010).

1.4.3 Noise reduction in fMRI

The reduction of temporal noise σ_{time} in the image time series can be achieved during the image acquisition, the image reconstruction or the statistical analysis. Most methods target individual noise sources, and, hence, a combination of several noise reduction methods is usually required. Prospective techniques can reduce the impact of motion (Speck et al., 2006) and low-frequency drifts and breathing-related field fluctuations (Duerst et al., 2015). Similarly during image reconstruction, fluctuations in the main magnetic (Hu and Kim, 1994) and the image encoding fields (Bollmann et al., 2017) can also be addressed. Incorporated into the statistical analysis are a number of dedicated preprocessing steps, targeting different noise sources: the impact of motion is reduced through the alignment of the image time series (Friston et al., 1996), and thermal noise is reduced through spatial smoothing (Friston, 2007b). Motion, low-frequency drifts and physiological noise can also be addressed during the statistical modelling by incorporating appropriate confound regressors (Hutton et al., 2011; Kiebel and Holmes, 2007). A more detailed overview on noise reduction strategies can be found in Murphy et al. (2013) and Caballero-Gaudes and Reynolds (2016).

1.5 Evaluating functional sensitivity

Functional sensitivity is, for example, assessed when developing a new fMRI acquisition technique or compiling an fMRI acquisition protocol for a specific research question. This

allows the tailoring of the acquisition parameters to the region of interest and the ensuing statistical analysis. Given the large number of components and their non-linear interactions, functional sensitivity is often evaluated in a hierarchical fashion (Welvaert and Rosseel, 2013). Therein, a number of surrogate measures describing individual aspects of functional sensitivity are utilized. This allows the gradual evaluation and optimization of parameters using easily accessible measures first, and only later on employing more involved fMRI experiments.

Image quality is usually assessed first when evaluating functional sensitivity. It provides information about the spatial specificity in terms of distortion level, ghosting, blurring, coverage, areas of signal loss and resolution. The main disadvantage is the predominantly manual interpretation through visual inspection. At this stage, also the ensuing statistical analysis should be considered, for example the proposed smoothing kernel in relation to the voxel size. A first estimate of BOLD sensitivity can already be obtained using equation (10). However, this estimate can be misleading in areas with strong susceptibility gradients, which cause a shift in the local effective echo time (Deichmann et al., 2002).

Next, the tSNR can be obtained from the fMRI image time series by computing the ratio of its mean and standard deviation over time (Friedman and Glover, 2006; Welvaert and Rosseel, 2013). Thereby, the temporal noise σ_{time}, a key component of BOLD sensitivity (eq. (12)), can be evaluated. However, the relationship between tSNR and BOLD sensitivity is highly non-linear, and depends on a number of factors ranging from echo time and resolution to effect size (ΔI) and false-positive level (Murphy et al., 2007). Similarly, Fera et al. (2004) observed that an increase in tSNR does not necessarily induce an equally high increase in t-score.

The contrast-to-noise ratio (CNR), which is analogue to the BOLD sensitivity as defined in equation (12), is often employed in the assessment of data quality (Geissler et al., 2007; Welvaert and Rosseel, 2013). It is independent from the design efficiency and the number of samples, which can, under certain conditions, provide direct insight into properties such as effect size and noise level.

Ultimately, evaluation of functional sensitivity is commonly performed using t-scores whose definition (eq. (7)) resembles the definition of functional sensitivity in equation (14). However, equation (14) does not take into account the effect of serial correlations and confound modelling, which can have considerable impact especially at higher field strengths (Hutton et al., 2011; Kasper et al., 2017) and for fast sequences (Chapter 3).

Note that in practice, the optimality criterion in equation (11) can be relaxed, and a range of echo times can provide an adequate BOLD sensitivity (Gorno-Tempini et al., 2002; Poser

and Norris, 2009). To compute CNR or t-scores across the whole brain, a global change of T_2^* is required. A global change in blood oxygenation can, for example, be induced by breath-hold experiments (Bright and Murphy, 2013). Alternatively, stimuli inducing known neuronal activity are employed to evaluate functional sensitivity in a region-of-interest (ROI). This is especially useful if targeting specific brain regions either because of their functional role or known deficits in functional sensitivity.

In summary, functional sensitivity consists of BOLD sensitivity and spatial specificity, which are both dependent on a number of acquisition parameters. In practice, individual constituents of functional sensitivity are evaluated before performing comprehensive statistical analysis. In the reminder of this thesis, I will apply this framework for the evaluation of functional sensitivity to new fMRI sequences and introduce its implementation in the uniQC toolbox.

1.6 Outline of the thesis

- Chapter 2 illustrates sequence evaluation for a multi-echo SMS EPI. Therein, the nuclei of the basal ganglia were specifically targeted, which are characterized by their short T_2^* values (Peters et al., 2007), leading to reduced BOLD sensitivity compared to cortical areas (eq. (11)). Based on initial promising results (Bollmann et al., 2015), a comprehensive assessment of a single-echo vs multi-echo SMS EPI was performed including all levels from basic tSNR and image quality measures, to single subject CNR maps, and, ultimately, group-level t-scores and extent of activation.
- Chapter 3 investigates serial correlations in SMS EPI with sub-second temporal resolution. The definition of BOLD sensitivity as stated in equation (12) and (14) assumes independence between sampling points, which is not the case for fMRI data (Friston et al., 1994). In this study, the interaction between repetition time and serial correlations was investigated, alongside the impact of physiological noise modelling. It could be concluded that advanced pre-whitening schemes are required for valid inference using fMRI data acquired at these short temporal scales.
- Chapter 4 presents the Unified NeuroImaging Quality Control (uniQC) toolbox, which was developed over the course of this thesis. It incorporates the concepts discussed here, and is meant to provide easy access to a wide range of fMRI time series quality measures. These include basic quality measures, such as mean and tSNR images, and versatile visualisation tools as required in the initial development stage. Additionally, image operations and common preprocessing steps up to whole

statistical analysis using SPM[3] are provided. The underlying design theme was to provide flexible handling of a large range of data types, but at the same time ensure reproducibility through data provenance and documentability provided by the strict usage of function calls in an object-orientated framework.

- Chapter 5 discusses implications for future studies, advanced pre-whitening schemes, and new measures for functional sensitivity.

[3] http://www.fil.ion.ucl.ac.uk/spm/

Chapter 2

Using multi-echo simultaneous multi-slice (SMS) EPI to improve functional MRI of the subcortical nuclei of the basal ganglia at ultra-high field (7T)

Saskia Bollmann[1,†], Alexander M. Puckett[2,†], Benedikt A. Poser[3], Jake Palmer[4], Markus Barth[1,†], Ross Cunnington[2,4,†]

[1]Centre for Advanced Imaging, The University of Queensland, Brisbane QLD 4072, Australia

[2]Queensland Brain Institute, The University of Queensland, Brisbane QLD 4072, Australia

[3]Department of Cognitive Neuroscience, Faculty of Psychology and Neuroscience, Maastricht University, Maastricht, The Netherlands

[4]School of Psychology, The University of Queensland; Brisbane QLD 4072; Australia

† Indicates shared first/senior authorship.

Keywords

Functional MRI

EPI

Simultaneous multi-slice

Multi-echo

Susceptibility artefacts

Signal loss

Echo time

Basal ganglia

Motor

Abstract

The nuclei of the basal ganglia pose a special problem for functional MRI, especially at ultra-high field, because T2* variations between different regions result in suboptimal BOLD sensitivity when using gradient-echo echo-planar imaging (EPI). Specifically, the iron-rich lentiform nucleus of the basal ganglia, including the putamen and globus pallidus, suffers from substantial signal loss when imaging is performed using conventional single-echo EPI with echo times (TE) optimized for the cortex. Multi-echo EPI acquires several echoes at different echo times for every imaging slice, allowing images to be reconstructed with a weighting of echo times that is optimized individually for each voxel according to the underlying tissue or T2* properties. Here we show that multi-echo simultaneous multi-slice (SMS) EPI can improve functional activation of iron-rich subcortical regions while maintaining sensitivity within cortical areas. Functional imaging during a motor task known to elicit strong activations in the cortex and the subcortex (basal ganglia) was performed to compare the performance of multi-echo SMS EPI to single-echo SMS EPI. Notably within both the caudate nucleus and putamen of the basal ganglia, multi-echo SMS EPI yielded higher tSNR (an average 84% increase) and CNR (an average 58% increase), an approximate 3-fold increase in supra-threshold voxels, and higher *t*-values (an average 39% increase). The degree of improvement in the group level t-statistics was negatively correlated to the underlying T2* of the voxels, such that the shorter the T2*, as in the iron-rich nuclei of the basal ganglia, the higher the improvement of *t*-values in the activated region.

2.1 Introduction

Blood oxygenation level dependent (BOLD) fMRI is most commonly performed using a gradient-echo echo-planar imaging (GE-EPI) sequence at high (3T) or ultra-high field (≥ 7T) for enhanced functional sensitivity. In conventional GE-EPI sequences, the functional contrast depends on the chosen echo time (TE). The maximum BOLD contrast occurs at the TE at which the difference in the T2* signal decay of the oxygenated states of hemoglobin is maximal. In a first approximation, this is achieved when matching the TE with the effective transverse relaxation time (T2*) of the underlying tissue (Gati et al., 1997; Triantafyllou et al., 2005). A particular challenge for functional MRI of subcortical nuclei is the significant regional variation in T2* that exists across different brain regions, specifically between cortical and subcortical regions, i.e. T2* in subcortical nuclei is considerably shorter than in cortical regions (Cohen-Adad et al., 2012; Deistung et al., 2013; Sedlacik et al., 2014; Yao et al., 2009).

The significant regional variation in T2* across different brain areas is caused by two effects, i.e. (i) by tissue-intrinsic (microscopic T2 and diffusion) as well as mesoscopic (smaller than voxel size, but larger scale than microscopic) relaxation effects, and (ii) by macroscopic effects from static field inhomogeneities. The macroscopic effects are caused by magnetic susceptibility differences at the interfaces between tissue, air, and bone (Volz et al., 2009) or suboptimal shim settings and can result in signal loss and image distortions. As these macroscopic effects depend on acquisition parameters such as slice-thickness and orientation, they can be partly reduced by optimizing a range of sequence properties including slice tilt and phase-encoding direction in a whole-brain (Robinson et al., 2008; Weiskopf et al., 2007, 2006) or in a slice-by-slice fashion (Brunheim et al., 2017; Stocker et al., 2006).

While these techniques are well-suited to compensate for large-scale, temporally static, and gradually changing susceptibility gradients in space, they cannot compensate for microscopic and mesoscopic effects caused by the high iron content within the basal ganglia nuclei (Gelman et al., 1999; Ordidge et al., 1994), which lead to a short T2* in these brain regions (Peters et al., 2007; Robinson et al., 2004; Schenck, 2003). The reduced T2* then causes considerable signal loss in EPI images using a single TE optimized for cortical regions (Berger et al., 2016; Koopmans et al., 2011; van der Zwaag et al., 2009; Yacoub et al., 2001) as this TE is usually much longer than the T2* of the basal ganglia nuclei at ultra-high field (Cohen-Adad et al., 2012; Deistung et al., 2013). Hence it is impossible for single-echo EPI to provide an optimal BOLD sensitivity for the entire brain.

Multi-echo fMRI is a technique that has been shown to compensate for regional T2* variation and enhance functional sensitivity (Posse et al., 1999). Multi-echo imaging involves collecting multiple sets of echoes at a range of different TEs, which can then be combined to optimize functional sensitivity in a voxel-wise manner depending on the optimal TE for the underlying tissue. Applied to GE-EPI and in combination with parallel imaging, multi-echo EPI has been shown to improve functional sensitivity at both 3T (Poser et al., 2006) and 7T (Poser and Norris, 2009) with larger improvements seen in regions suffering from susceptibility-induced inhomogeneities. Here, we investigate the capabilities of multi-echo imaging to compensate for the mesoscopic, within-voxel inhomogeneities that occur in iron-rich subcortical nuclei such as the basal ganglia while retaining high sensitivity in cortical regions. In this study, we combined the multi-echo readout with a state-of-the-art implementation of a simultaneous-multislice (SMS) acquisition and reconstruction technique to obtain a sub-second volume repetition time (TR) for whole-brain imaging.

2.2 Theory

2.2.1 Multi-echo imaging for fMRI

Multi-echo EPI is a functional imaging technique that can increase the BOLD sensitivity while simultaneously reducing image distortions and signal loss (Poser and Norris, 2009). In essence, multi-echo imaging involves acquiring multiple echoes in one shot following a single RF pulse. This opens up various possibilities for how to process the data and to exploit the additional information that is obtained by simultaneously acquiring the BOLD signal at different echo times. A straightforward option is to combine the different echoes into a single image time series, which can then be processed and analyzed in a conventional manner just like a single-echo acquisition; this is the path chosen for the present study. The change in T2* due to changes in blood oxygen level can also be investigated directly by fitting a mono-exponential decay to the different echoes (Speck and Hennig, 1998). Another option that has gained interest recently is to use the multi-echo information for automatic denoising with the MEICA technique (Kundu et al., 2017, 2014, 2012). This method attempts to separate ‘BOLD like’ from ‘non-BOLD like’ signal components (and filter out the latter) by performing an ICA across the spatial concatenation of the multiple echoes and then characterizing their TE dependence as T2* induced (linear TE dependence, i.e. BOLD like) or S0 induced (no TE dependence, i.e. artefact like). However, the focus of this study was on BOLD sensitivity, and the ability of multi-echo EPI to provide more uniform sensitivity

across different underlying T2* values; hence, we chose a form of weighted echo combination as described below.

Echo combination using a weighted summation has been shown to maximize the contrast-to-noise-ratio (CNR) by matching the weights applied to images of different echo times to the bell-shaped BOLD sensitivity curve (Posse et al., 1999). However, this requires the accurate knowledge of the T2* values at each voxel location. An alternative strategy has been proposed by Poser et al. (2006), in which the different echoes are weighted directly by their measured CNR. To avoid confounds through task related signal changes, the tSNR needs to be estimated from additional calibration scans. However, a simple average across the different TE images outperformed the CNR-weighted average in regions with short T2* (Poser and Norris, 2009), and a recent study by Kettinger et al. (2016) has shown that all combination schemes perform equally well. Here, we used the temporal average of the time series (AVG) instead of the tSNR. The benefit of this weighting scheme is that the weights can be directly estimated from the data and no additional calibration scans or model assumptions are required. Importantly, changes in the signal due to BOLD fluctuations (i.e. due to task or resting-state fluctuations) do not influence the weights as they primarily affect the estimated variance, but not the average.

$$w_n = \frac{AVG_n \cdot TE_n}{\sum AVG_n \cdot TE_n} \tag{18}$$

One potential limitation of multi-echo EPI is the prolonged readout time, which is especially challenging for 7T-applications due to the short T2* values in grey matter and subcortical nuclei in comparison to lower field strength (Peters et al., 2007; Yao et al., 2009). However, parallel imaging can be used to drastically reduce the number of phase encoding steps, which in turn reduces the EPI readout time and simultaneously increases the bandwidth in phase encoding direction to reduce image distortions and blurring (Poser et al., 2006). This has enabled the successful applications of multi-echo EPI at 7T to reduce artefacts and enhance functional contrast (Poser and Norris, 2009). In a separate development, SMS EPI (Feinberg et al., 2010; Setsompop et al., 2012) based on earlier work by Larkman et al. (2001) and Breuer et al. (2005) has brought the capability to significantly reduce the TR by acquiring multiple slices at once; for a review on this topic see Barth et al. (2016). In this study, we combine both the ME-EPI and SMS-EPI techniques, which allows us to acquire multi-echo EPI with whole-brain coverage at a temporal resolution of well below one second TR.

2.2.2 Motor cortex and basal ganglia

When performing complex motor movements, activity is elicited in a wide network of areas including cortical motor areas and subcortical nuclei of the basal ganglia and thalamus (Bednark et al., 2015; Cunnington et al., 2002; Lehericy et al., 2006). These subcortical nuclei within the basal ganglia are known to be high in iron content. Early post-mortem histological evidence showed that non-heme iron levels vary throughout the brain with highest concentration consistently found within the basal ganglia, particularly within the lentiform nucleus that contains regions of the putamen and globus pallidus (Drayer et al., 1986; Hallgren and Sourander, 1958). These early findings have been confirmed in-vivo through recently developed MRI techniques that form susceptibility-weighted images sensitive to iron levels (Deistung et al., 2013; Haacke et al., 2005, 2004; Schafer et al., 2012; Schweser et al., 2011). While the high iron content of the basal ganglia can be exploited for anatomical imaging to improve delineation of structural boundaries (Abosch et al., 2010), it is highly detrimental for the functional contrast necessary for fMRI. This is particularly problematic at high magnetic field strengths as the signal decays even more rapidly resulting in shorter T2* and very little signal remaining at typically used TEs (Schenck, 2003). Multi-echo EPI sequences may therefore be ideally suited to whole-brain fMRI of complex motor movements at 7T, to improve the concurrent imaging of cortical and subcortical areas that differ in underlying T2* values and thereby to compensate for the signal loss typical seen in fMRI of the basal ganglia.

2.3 Methods

To test whether multi-echo EPI can improve functional imaging of cortical and subcortical areas over single-echo EPI for a complex motor task, we performed whole-brain fMRI during finger motor movements known to elicit coordinated activity in primary motor cortex (M1), supplementary motor cortex (SMA), and the basal ganglia. Data were collected using both single-echo and multi-echo sequences for each participant to allow direct comparison between MRI sequence types.

2.3.1 Participants

N = 10 right-handed participants (7 female) in the age range of 21-30 years, (M = 25.1, SD = 3.6 years) with no history of neurological or psychiatric diseases participated in this study. The experiment was conducted with the understanding and written consent of each subject and was approved by the local ethics committee and in accordance with national guidelines.

2.3.2 Experimental design

Participants performed motor movements in response to visual cues while inside the MRI scanner (Figure 2-1). The visual stimuli were presented on a projector screen at the back of the scanner, viewed from a mirror mounted on the head coil. There were two experimental conditions, simple and complex finger-movements, which both involved making four-finger motor movements by pressing buttons in sequence on a four-button response box with the index, middle, ring, and little fingers of the right hand. Previous work has shown that this movement task elicits focal clusters of differential activity in cortical motor areas and within the basal ganglia (Bednark et al., 2015). The rationale was to therefore use these two conditions to localize and then examine the responses in voxels simultaneously activated in both cortex and subcortex under multi-echo versus single-echo imaging sequences.

The motor responses in both conditions (i.e. simple and complex) were self-paced and differed only in the duration of button presses. The stimulus for the simple movement condition (Figure 2-1A) consisted of four equal sized and evenly spaced dashes. Subjects made four consistent, medium length button presses with the same stimulus presented for each trial within a simple block. For the complex movement condition (Figure 2-1B), the stimulus consisted of dots and dashes indicating button presses of different durations, in a Morse code style. Dots represented a short button press while dashes represented a long button press, with a combination of two short and two long presses per presentation. Therefore, there were six possible combinations of short and long button presses for the complex condition. A single trial of either the simple or complex movement condition involved the visual cue being presented for 2500 ms, followed by a fixation cross that was presented for another 500 ms, as shown in Figure 2-1. Subjects were instructed to complete the movement before the next presentation of the fixation cross but to remain consistent, taking up the entire available time to complete the movement.

The fMRI paradigm followed a block design consisting of three types of blocks: simple movement, complex movement, and rest (Figure 2-1C). Each movement block contained six single trials (3000 ms trial length), in which participants performed either the simple or complex movement, resulting in a total block length of 18 s. In every complex movement block, each of the six possible combination of short and long button presses was presented once. Between complex movement blocks, the order of presentation of the different combinations was randomized. In the simple movement block, participants performed the simple movement repeatedly. In the rest block, participants were instructed to passively view the fixation cross.

For all participants, each fMRI run started with a rest block (Figure 2-1C). The order of the first presentation of each of the two following movement conditions was then counterbalanced between participants. Specifically, half of the participants followed the order of rest – simple – complex – rest – complex – simple repeated, while the other half followed the order of rest – complex – simple – rest – simple – complex repeated. An extra rest block was also included following the final movement condition to ensure the BOLD signal associated with the movement was acquired. In total, each movement condition was presented six times and a full run lasted of 342 s. Two functional runs were collected using each sequence (i.e. single-echo and multi-echo) within the scan session, and the order was counterbalanced with respect to acquisition sequence.

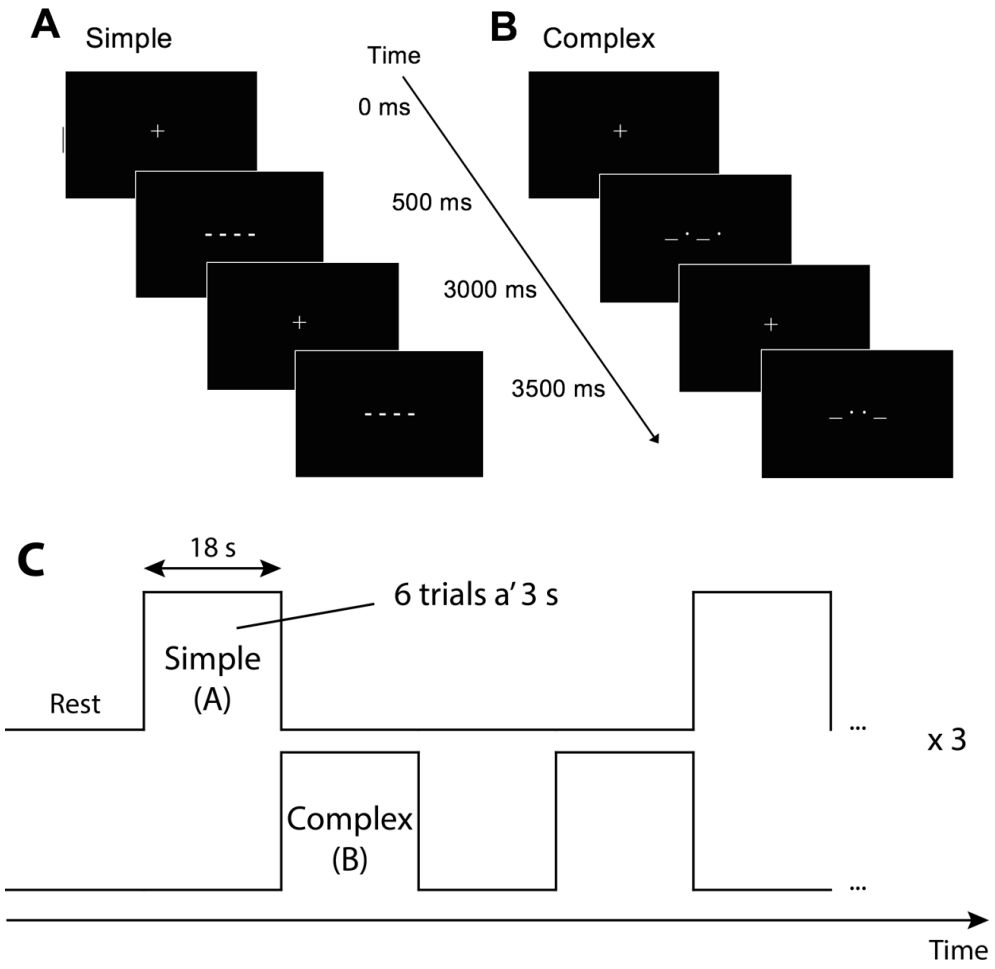

Figure 2-1: Experiment overview. For the simple movement condition (A) participants made four consistent medium length button presses corresponding to the four evenly spaced dashes. For the complex movement condition (B) participants completed combinations of two short and two long button presses corresponding to dots and dashes. Importantly, the stimulus in the complex condition changed with each presentation, while the stimuli in the simple condition remained the same. For both simple and complex conditions, the fixation cross was present for 500 ms with the stimulus presented for 2500 ms. Each run started with a rest block of 18s (C), followed by simple – complex – rest – complex – simple blocks for half of the participants. The other half the participants started with the complex movement condition. In total, six simple and six complex blocks were presented per run, and each run lasted for 342 s.

Before beginning the experiment, participants completed a training run. The training was sufficiently short to ensure the complex movement sequences were not learned, but participants were able to become familiar with the visual cues, button responses and requirements of the task. This training took place either outside the scanner on a standard desktop computer and keyboard or in the scanner before the first functional scan.

2.3.3 Magnetic resonance imaging data acquisition

All images were acquired on a whole-body 7T Siemens Magnetom MRI scanner (Siemens Healthcare, Erlangen, Germany) with a 32-channel head coil (Nova Medical, Wilmington, US). B0 shimming up to 3rd order was employed to minimize field inhomogeneity. The single-echo images were acquired using the CMRR SMS sequence implementation (release 11a) (https://www.cmrr.umn.edu/multiband/). The multi-echo acquisition used a SMS version of the multi-echo sequence described in Poser and Norris (2009). When choosing the sequence settings, the following key parameters were kept equal for both sequences to facilitate the comparison: spatial resolution (to prevent tSNR changes through differences in voxel volume), total scan time, in-plane acceleration factor using GRAPPA (Griswold et al., 2002) and slice acceleration factor using SMS (to obtain comparable image quality). SMS reconstruction was done using the slice-GRAPPA technique (Setsompop et al., 2012) as implemented in the CMRR sequence for the single-echo EPI, and the MGH blipped-CAIPI SMS-EPI sequence (https://www.nmr.mgh.harvard.edu/software/c2p/sms) for the multi-echo sequence. The CMRR implementation for the single-echo sequence was chosen as it is a well-established, commonly used sequence for single-echo EPI (Van Essen et al., 2013). It also offers increased reconstruction speed compared to other sequences such as the single echo version of the multi-echo sequence. The in-plane acceleration factor was selected based on the multi-echo sequence to facilitate the acquisition of three echoes with sufficiently short echo times. Further shortening of the EPI echo trains was effected by use of phase partial Fourier (6/8) in case of the multi-echo sequence. The slice acceleration factor was chosen to provide sub-second temporal resolution for whole-brain acquisition. Images were acquired with axial slices covering the brain from the most dorsal cortex to approximately midway through the cerebellum.

In detail, both sequences shared the following acquisition parameters: isotropic voxel size = 2.5 mm, matrix size = 84 x 84, FOV = 212 x 212 mm, number of slices = 48, flip angle = 35°, GRAPPA acceleration factor = 2, SMS acceleration factor = 4. The TE for the single-echo acquisition was set to 23 ms, slightly shorter than the measured optimum for 7T BOLD fMRI in cortical areas (Berger et al., 2016; Koopmans et al., 2011; van der Zwaag et al., 2009;

Yacoub et al., 2001). The three echoes of the multi-echo sequence were acquired at 9.9 ms, 28 ms and 45 ms, respectively. While resolution and acceleration factors were equal for both sequences, the TR was set to the minimal possible length to maximize the number of acquired samples for a given run-length, resulting in a TR of 589 ms for the single-echo sequence and 830 ms for the multi-echo sequence.

For anatomical reference, a three-dimensional whole brain T1-weighted structural image was acquired for each participant using a prototype MP2RAGE sequence (WIP 900) (Marques et al., 2010; O'Brien et al., 2014) with the following parameters: TE = 2.5 ms, TR = 4300 ms, flip angle (FA) = 5° and 6°, inversion time (TI) = 840 ms and 2370 ms, GRAPPA factor = 3, acquisition matrix = 320 x 300 x 256 and an isotropic voxel size of 0.75 mm.

2.3.4 Preprocessing

All MRI data preprocessing was performed using the AFNI analysis package (Cox, 1996). Each functional EPI volume was registered to the volume with the minimum outlier fraction (i.e. the volume that is least different from all the others after detrending) to correct for head motion. The subject's anatomical images were aligned with the functional data by skull-stripping and then aligning the anatomical to the same EPI base (with minimum outlier fraction) using AFNI's align_epi_anat.py script. The functional data for each subject was transformed into a standard space by computing the transform required to non-linearly warp the subject's anatomical to match the Montreal Neurological Institute (MNI) 152 template at 0.75 mm isotropic resolution (Fonov et al., 2009) and then applying this tranform to the functional data.

The initial preprocessing steps were performed identically for both the single-echo and multi-echo data, with the only difference being that there were three sets of images per run for the multi-echo data rather than a single set per run as in the case of the single-echo data. Weighted summation based on the temporal average as described in section 2.1 was then used to combine the different echoes. To obtain estimates of T2* values in cortical and sub-cortical regions, we performed a voxel-wise linear fit on the logarithm across the three echoes for each subject on the temporal average, assuming a mono-exponential decay and low noise levels.

2.3.5 Single-subject analysis

All functional time-courses were scaled to percent signal change (i.e. each voxel time series was scaled to have a mean of 100) before calculating a multiple linear regression. The regression model contained 2 regressors corresponding to each experimental condition

(simple and complex movement, Figure 2-1C) generated by convolving the stimulus timing of each condition with a canonical hemodynamic response function model. A further 6 regressors, estimated from the volume registration step and representing the participant's head movement during the scan, were also included. From the calculated regression model, contrast-to-noise ratio (CNR) was calculated on a voxel-wise basis for each condition by dividing each voxel's beta or linear contrast value from the general linear model analysis by the standard deviation of the residual error of the time-series for that voxel. Results from the single-subject regression analysis were then used in a second stage group analysis as described below (section *Group analysis*).

In addition to the task-based fMRI, resting state scans were acquired for a single participant to assess the tSNR achieved with both sequences. To this end, 50 volumes were collected at rest using each sequence, and tSNR images were calculated by dividing the mean signal in each voxel by its standard deviation across all 50 volumes. The tSNR was then compared across regions of interest (ROIs) by calculating the average tSNR of all voxels within each ROI.

ROIs for the tSNR analysis included cortical regions M1 and SMA as well as the subcortical caudate nucleus (CN) and putamen (PUT) within the basal ganglia. The cortical regions were defined using the Harvard-Oxford atlas developed at the Center for Morphometric Analysis (CMA), and distributed with the FMRIB Software Library (FSL) (Desikan et al., 2006; Frazier et al., 2005; Goldstein et al., 2007; Makris et al., 2006). This probabilistic atlas was thresholded at 33 % and resampled to match the resolution of the functional data (2.5 mm isotropic). For the subcortical nuclei, the basal ganglia were first identified using a recently published basal ganglia atlas derived from high-resolution 7T anatomical imaging (Keuken et al., 2014). As this atlas defines the striatum as a single ROI, the striatum was then manually divided into the CN, PUT, and ventral striatum (VST) based on the guidelines set forth by Tziortzi et al. (2014).

2.3.6 Group analysis

To construct group statistical parametric maps to examine effects across all participants, mixed effects meta-analyses were performed using AFNI's 3dMEMA. This program models both within- and across-subject variability and therefore requires both the regression coefficients or a general linear contrast among them as well as the associated t-statistic from each subject. Being interested in the voxels that respond differentially to the complex vs. simple movement conditions, we used the general linear contrast between the two

regression coefficients (complex – simple) and the corresponding t-statistics from each subject to construct the group maps.

The mixed effects meta-analysis was first performed separately for the single-echo and combined multi-echo data to construct sequence-specific group maps. The overall extent of activation detected using the different sequences was compared by counting the number of active voxels within each atlas-based ROI (section *Single-subject analysis*) for each sequence-specific group map. Voxels were defined as active if they survived a threshold set to the false discovery rate (FDR)-corrected q value of 0.05 (Genovese et al., 2002).

Next, those voxels within the atlas-based ROIs that were commonly activated in both sequences, i.e. those showing a significantly different response to the complex movement condition compared to the single movement condition across both sequences, were identified. To this end, data from both sequences were combined into one dataset and the same mixed effects meta-analysis was performed. The rationale for not including the entire structural ROIs was that only small regions within the relevant basal ganglia nuclei were expected to show activation due to the motor task (Bednark et al., 2015). Therefore, including all voxels within a structural ROI for analysis would result in a very small effect size, as the majority of voxels within the ROI would not show significant activation. These functionally-defined ROIs were then applied to the sequence-specific group maps to compare the t-statistic values measured using each sequence across an identical set of voxels. These same ROIs were also applied to group CNR maps constructed by voxel-wise averaging of the individual subject CNR maps.

2.4 Results and discussion

2.4.1 tSNR in a single subject

tSNR images were computed for each sequence using the resting state scans with an equal number of volumes from a single subject to illustrate basic signal properties (Figure 2-2A) (Welvaert and Rosseel, 2013) and indicate the effect of weighting the first echo in the basal ganglia (Figure 2-2B). Figure 2-2A (top) shows a single axial slice of the tSNR images computed for the single-echo data (left) and for the combined multi-echo data (right). The slice shown intersects the BG (red arrows), and as expected, although tSNR is high in the cortex, considerable signal loss can be seen in the basal ganglia in the single-echo data. The combined multi-echo data, however, suffers far less from this signal void, profiting from the increased signal levels incorporated from the earlier echo. This is illustrated in the tSNR

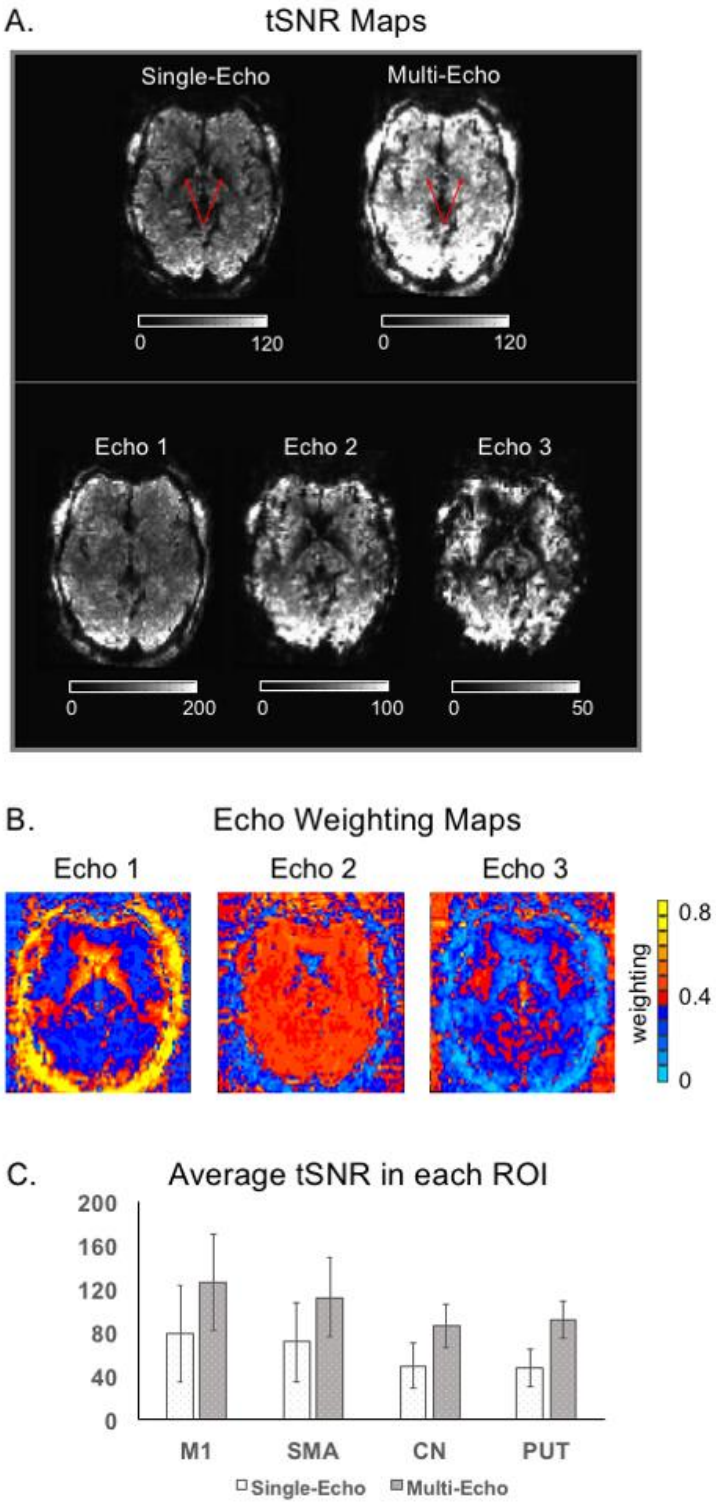

Figure 2-2: tSNR maps. *(*A) tSNR maps. Top, increased tSNR was found for the combined multi-echo acquisitions compared to the single-echo sequence. Red arrows indicate dark areas of signal loss in the basal ganglia. Bottom, tSNR maps of each echo of the multi-echo sequence illustrating the relatively homogenous tSNR for the first echo and the signal loss in the basal ganglia at the later echoes. (B) Weighting maps at same slice for each echo (see Eq. 1) with higher values for the first echo in the basal ganglia. (C) Average tSNR in each ROI showing the increased tSNR for the multi-echo sequence. Error bars represent standard deviation of the tSNR across all voxels in each ROI.

images (Figure 2-2A, bottom) and echo weighting maps (Figure 2-2B) constructed separately for the individual echo data collected with the multi-echo sequence. Note the

increased contribution of the first echo in the basal ganglia illustrated in the echo weighting maps.

To quantify the tSNR in each ROI we averaged across all voxels in each ROI (Figure 2-2C) finding that the multi-echo sequence yielded higher tSNR in all ROIs, both cortical and subcortical with an average increase in tSNR of 84 % in the basal ganglia ROIs. This was further supported by a paired-sample t-test performed on the tSNR values across all voxels within the ROIs, finding that the tSNR was significantly greater for the multi-echo sequence (M=116, SD=42) than the single-echo sequence (M=70, SD=25); $t(6835)= -114$, $p<0.001$. These results show that, as expected, tSNR of the multi-echo sequence is increased overall, partially due to a longer readout; making better use of the 'dead time' after the RF excitation is indeed one of the advantages of multi-echo EPI (Poser and Norris, 2009).

When optimizing both sequences, we aimed to keep key parameters, such as resolution, in-plane and slice acceleration factor, FOV and reconstruction technique (Setsompop et al., 2012), equal to facilitate the comparison and interpretation of the results. Note that the same flip angle was also used for both sequences despite different TRs. While image SNR strongly depends on the chosen flip angle with respect to the repetition time, tSNR remains nearly constant across a broad range of flip angles (Gonzalez-Castillo et al., 2011). Hence, we do not expect a noticeable impact on the tSNR measurements due to using the same flip angle at different TRs. Furthermore, reconstruction performance between the two sequences might differ slightly (e.g. g-factor related noise amplification), similar to when comparing the same sequence with different acceleration factors (Chen et al., 2015; Moeller et al., 2010; Setsompop et al., 2012). This is related to variations in the sequence implementation and the additional partial Fourier factor employed in the multi-echo acquisition, and hence, could not be fully avoided.

2.4.2 Group statistical parametric mapping

Group *t*-statistic maps were computed separately for the single-echo (Figure 2-3A) and combined multi-echo (Figure 2-3B) data to examine how the spatial distribution and extent of the detected activation compared between the two sequences. Bilateral activation was detected in each ROI for both sequences with the multi-echo sequence showing a greater extent of activation in all ROIs except the SMA (Figure 2-3C). Qualitative comparison of the activation maps across sequences reveals the most striking difference is in the area of the basal ganglia (Figure 2-3A,B – green arrows), with a much greater extent of activation and larger *t*-statistics evident in the multi-echo data. For example, we observed about a 3-fold increase in supra-threshold voxel in both the putamen and caudate nucleus for the multi-

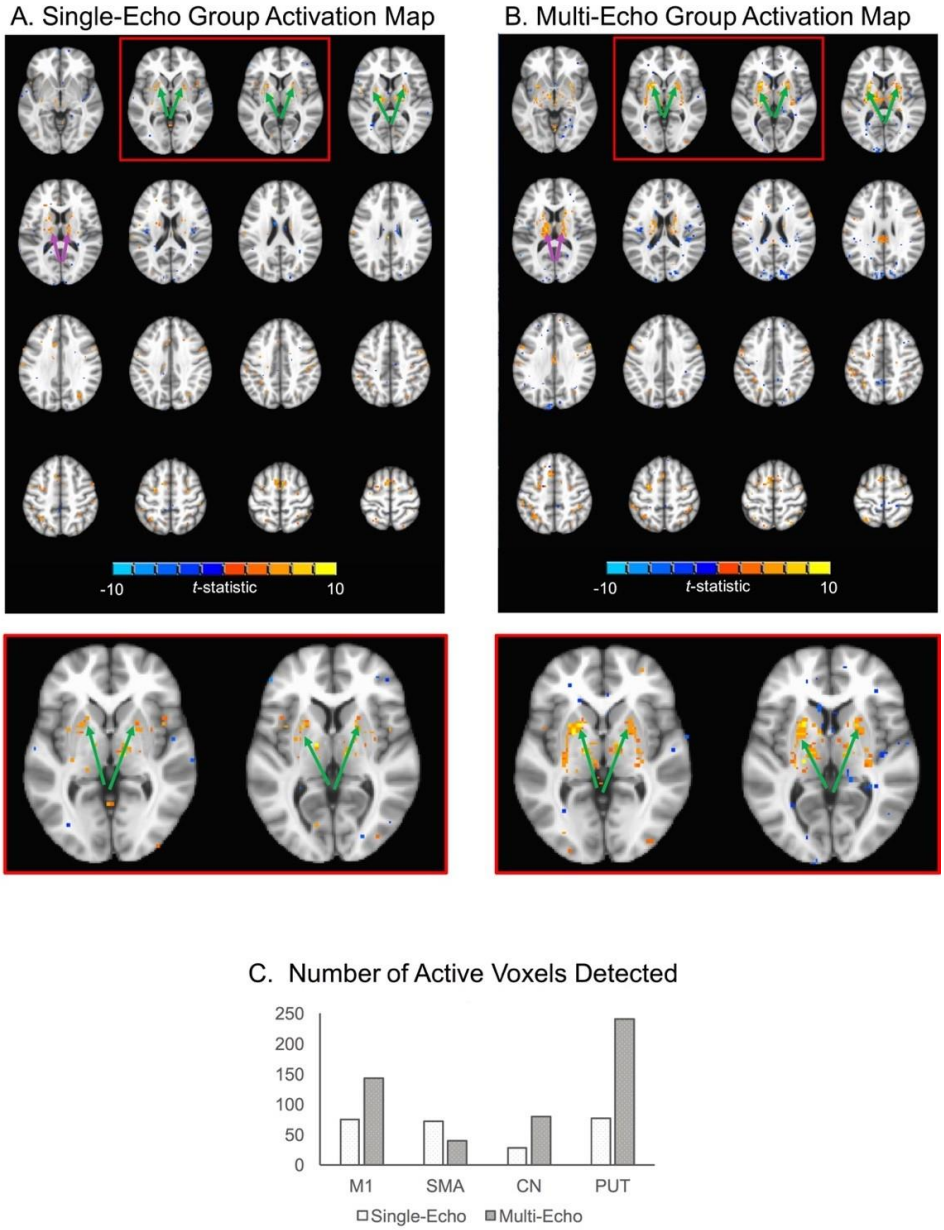

Figure 2-3: Group activation maps. Group activation maps displayed on a series of axial slices. (A) Single-echo and (B) multi-echo group *t*-statistic maps, both thresholded at a FDR-corrected $q<0.05$. Top illustrates a mosaic of slices across both cortical and subcortical ROIs. Bottom shows zoomed in version of two slices from the mosaic (denoted by red outline) showing considerable differences in basal ganglia activation between the two sequences. Green arrows point to regions in the basal ganglia showing marked improvement with the multi-echo sequence. Purple arrows point to significant activation in the thalamus, which, although not included in the subcortical ROI, also shows an improvement with the multi-echo sequence. (C) Number of functionally active voxels detected (i.e. those surviving threshold) within each ROI.

echo sequence (Figure 2-3C). In addition to the a priori defined subcortical ROIs, significant bilateral activation was also detected in the thalamus (Figure 2-3A,B – purple arrows). Although it is clear that a greater extent of activation was detected in the region of the thalamus using the multi-echo sequence compared to the single-echo, the responses in this region were not analysed further. Recall that the group activation maps in Figure 2-3 were constructed using the contrast between the complex and simple movement conditions.

Group activation maps for the two movement conditions vs. rest are included as supplementary material (Figure S1 and Figure S2) and, as expected, showed a much broader extent of cortical activation similar to that elicited by a conventional finger tapping motor paradigm.

2.4.3 Comparing activation parameters

To compare activation parameters across sequences and brain region, we extracted these from an identical set of voxels within each functionally-defined ROI (see section 3.6 for more on ROI definition and see supplementary Figure S3 for an illustration of the ROIs). A 2-way repeated measures ANOVA was performed to test the effect of sequence (single-echo, multi-echo) and ROI (M1, SMA, CN, PUT) on the magnitude of the *t*-statistic associated with the linear contrast between the two movement conditions (Figure 2-4A). Mauchly's test revealed that the assumption of sphericity was violated so the Greenhouse-Geisser correction was used. A main effect was found for both sequence [$F(1, 138)=111$, $p<0.001$)] and ROI [$F(2.5, 340)=24$, $p<0.001$)] as well as significant interaction between the two [$F(2.6, 361)=46$, $p<0.001$)]. The significant interaction indicates that the effect of the sequence was

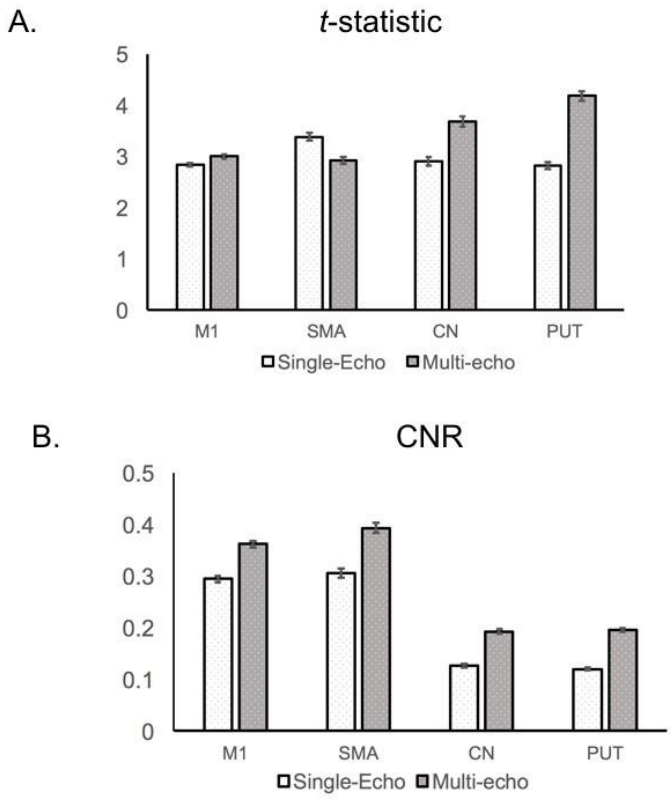

Figure 2-4: Group activation parameters. Comparing group activation parameters across sequence and brain region. (A) Increase in mean t-statistic was observed in putamen, caudate and M1 with highest improvement in the subcortical nuclei. (B) Increased CNR values were found in all ROIs. Error bars represent standard error of the mean.

dependent on the ROI. As can be seen in Figure 2-4A, it is clear that the improvement in *t*-statistic provided by the multi-echo sequence is greater in subcortical compared to cortical areas, with one of the cortical areas (SMA) actually showing a decrease in magnitude of the *t*-statistics when using multi-echo compared to single-echo data. When interpreting the *t*-statistics results here and in Figure 2-3, it is important to note that, when computing statistical maps on the single-subject level prior to performing the group analysis, the degrees-of-freedom differed between the two sequences due to the single-echo sequence having a shorter TR (approximately 30 % more volumes were acquired using the single-echo sequence compared to the multi-echo sequence). Hence, the improvement seen using the multi-echo sequence is in spite of the advantage afforded by the faster TR of the single-echo sequence.

To better understand the improvement in t-statistic afforded by the multi-echo sequence, additional 2-way repeated measures ANOVAs were performed to test the effect of sequence (single-echo, multi-echo) and ROI (M1, SMA, CN, PUT) on the CNR (Figure 2-4B). Again, a Greenhouse-Geisser correction was used as Mauchly's test revealed that the assumption of sphericity was violated. A main effect was found for both sequence [$F(1, 138)=240$, $p<0.001$)] and ROI [$F(2.2, 305)=210$, $p<0.001$)] as well as a mild interaction between the two [$F(2.0, 280)=3.5$, $p=0.03$)]. Inspection of Figure 2-4B reveals that the functional CNR was significantly higher for the multi-echo compared to the single-echo data in all ROIs ($p<0.001$). Together, these results demonstrate that increase in CNR on the single-subject level can translate to an improvement in t-statistics on the group level, with higher t-value gains in the subcortical regions.

*2.4.4 Relationship of sensitivity gains to T2**

The main goal of this study was to investigate the potential benefit of using a multi-echo EPI sequence to improve the simultaneous imaging of cortical and subcortical areas with different underlying T2* values. From previous work, it was expected that multi-echo imaging would improve image quality across the whole-brain, however, it was also predicted that this improvement would be greater in iron-rich subcortical nuclei marked by lower T2* values compared to cortical areas. In section 4.3, it was shown that improvement in t-statistic was indeed greater in subcortical areas compared to cortical regions. To further examine this issue, T2* values were estimated at each voxel and then compared to the degree of improvement in t-statistic provided by the multi-echo sequence. As expected, the average T2* varied across ROIs with the subcortical nuclei being marked by shorter T2* estimates than the cortical areas [ROI(mean,SD): M1(25.2, 3.7); SMA(30.9, 9.7); CN(18.3, 2.4);

PUT(17.5, 2.9)]. Interestingly, these values are close to the T2* values reported in (Peters et al., 2007), indicating that indeed the major source of signal dephasing in the basal ganglia are microscopic and mesoscopic susceptibility variations and not macroscopic field inhomogeneities. Figure 2-5 shows that there is a distinct correspondence between the T2* estimate and the improvement in t-statistic. It appears that the improvement is greatest in subcortical regions with lower T2* values relative to the cortical regions, with one of the cortical regions (SMA) actually showing a decrease in the average t-statistic when using the multi-echo sequence (Figure 2-5). This relationship is further supported by a significant negative voxel-wise correlation between the T2* estimate and the improvement in t-statistic ($r = -0.2665$, $P<.001$).

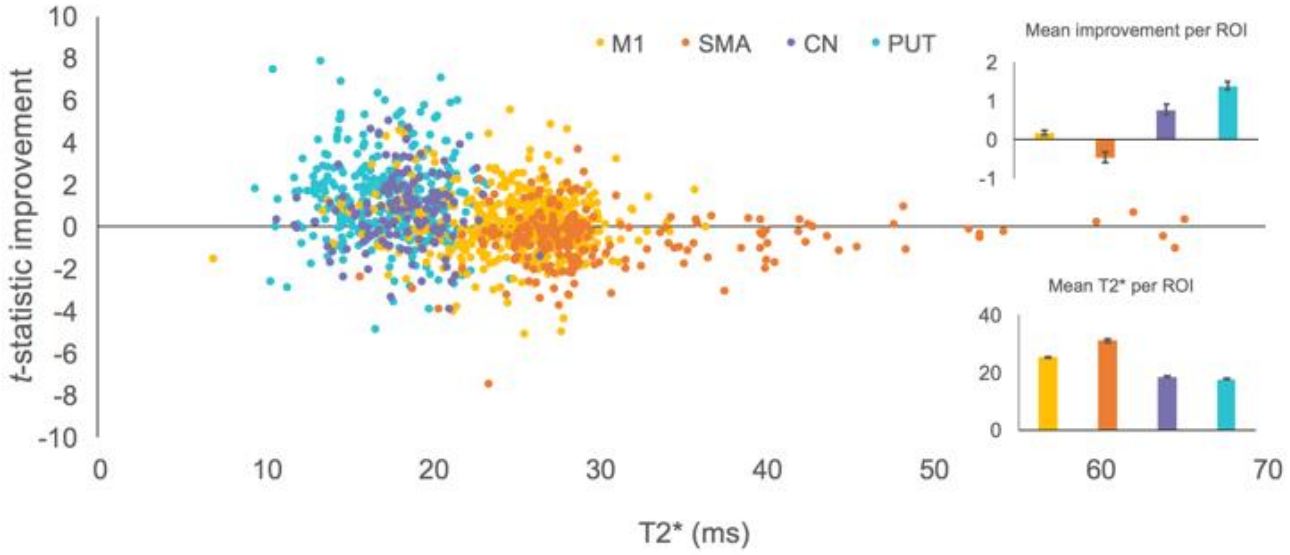

Figure 2-5: Improvement in *t*-statistic across brain regions. Main plot illustrates the voxel-wise comparison between the improvement in *t*-statistic and an estimate of the underlying T2*. Insets shows the average improvement (upper right) and T2* (lower right) in each ROI. Error bars represent standard error of the mean.

2.5 Conclusions and recommendations

This technical note demonstrates that multi-echo imaging can be used to improve the concurrent functional imaging of the cortex and subcortex at 7T compared to conventional single-echo EPI. As predicted, the greatest improvement in detecting activation was seen in the iron-rich, subcortical nuclei of the basal ganglia. Importantly, this was achieved while maintaining sensitivity to functional activity in the cortex although a slight decrease in performance was seen in the supplementary motor area. The improvement afforded by multi-echo imaging was achieved by maximizing sensitivity to different echo times at each

voxel through a weighted combination of the multiple echoes. By combining multi-echo imaging with a SMS acquisition scheme, it was possible to collect all three echoes with whole-brain coverage at a temporal resolution well below one second. Hence, the multi-echo SMS EPI sequence implemented here is well-suited to serve a wide range of functional imaging experiments.

One potential limitation for multi-echo EPI is the longer required echo train length. Using moderate parallel imaging factors and a conventional voxel size, we were, however, able to achieve sufficiently short TEs for imaging the iron rich basal ganglia nuclei at 7T. When higher resolution is required, one could either increase the acceleration factors of the parallel imaging methods employed here or resort to alternative acquisition schemes such as segmented Cartesian readouts (Hoogenraad et al., 2000; Li et al., 2002) or multi-echo spirals (Barth et al., 1999). Additionally, one could also further reduce the number of echoes, essentially acquiring only one early and one late echo. Given that the estimated average T2* in the Putamen was much higher than the first TE of the multi-echo sequence, it might be possible to increase the resolution and, thereby, lengthen the first TE to still obtain sufficient sensitivity in the iron-rich basal ganglia nuclei.

While in this study the main focus was on increased sensitivity to the BOLD signal, multi-echo EPI-based techniques to reduce noise contributions from physiology are powerful means to further increase functional sensitivity. For example, MEICA has been shown to reliably detect and remove physiological noise from fMRI time series (Kundu et al., 2014, 2012). Physiological noise (i.e. signal fluctuations in fMRI time series associated with cardiac and respiratory activity (Weisskoff et al., 1993) constitutes a major source of unwanted signal fluctuations (Bianciardi et al., 2009) increasing with field strength (Triantafyllou et al., 2005). Physiological noise is particularly problematic near the basal ganglia nuclei due to their proximity to major veins, with physiological noise modelling being shown to provide up to 30 % tSNR gain in these subcortical nuclei at 3T (Kasper et al., 2017). In this respect, the results obtained here represent a lower bound on the boost in sensitivity provided by multi-echo EPI at ultra-high field, with a further potential increase in sensitivity and specificity through physiological noise modelling (Boyacioğlu et al., 2015).

We conclude that multi-echo EPI acquisition offers increased BOLD sensitivity in regions with short T2*, such as the basal ganglia, and should be chosen over conventional GE-EPI when concurrently imaging cortical regions and iron-rich subcortical nuclei at 7T.

2.6 Acknowledgements

We thank Aiman Al-Najjar, Nicole Atcheson, and Steffen Bollmann for help with data collection. We thank Steve Cauley for providing a multi-echo enabled variant of the MGH slice-GRAPPA reconstruction and Himanshu Bath for details on the sequence-recon interface. This research was supported by the National Health and Medical Research Council (APP 1088419). MB acknowledges funding from Australian Research Council Future Fellowship grant FT140100865. SB acknowledges support through the Australian Government Research Training Program Scholarship. The authors acknowledge the facilities of the National Imaging Facility (NIF) at the Centre for Advanced Imaging, University of Queensland.

2.7 Appendix A. Supplementary data

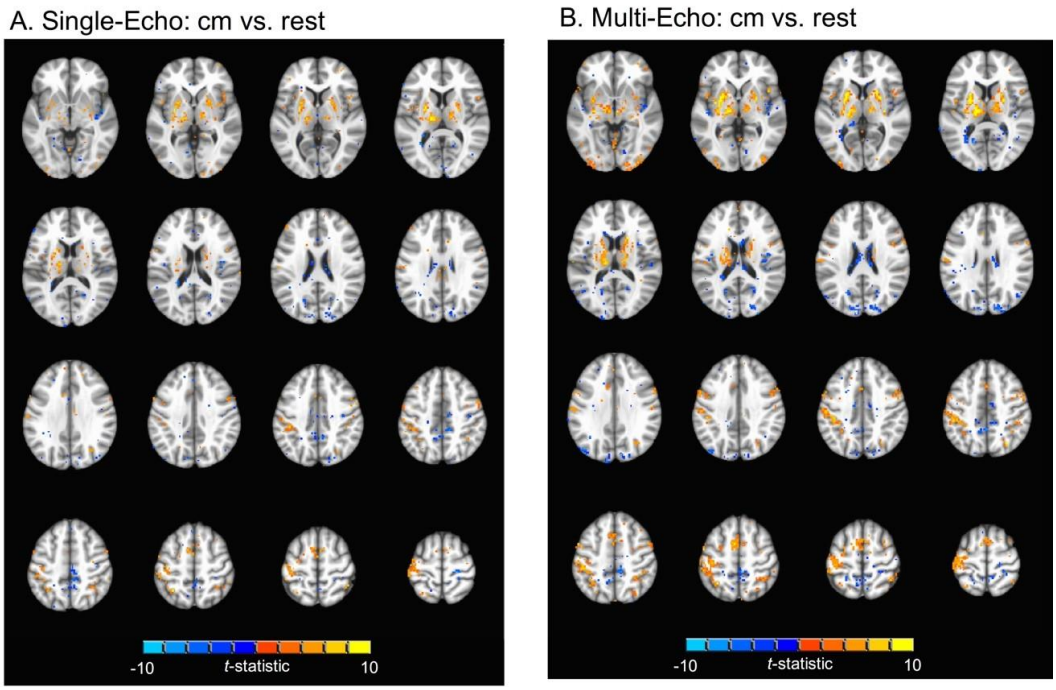

Figure S1: Group activation maps displayed on a series of axial slices for the complex movement (cm) – rest contrast. (A) Single-echo and (B) multi-echo group *t*-statistic maps, both thresholded at a FDR-corrected $q<0.05$.

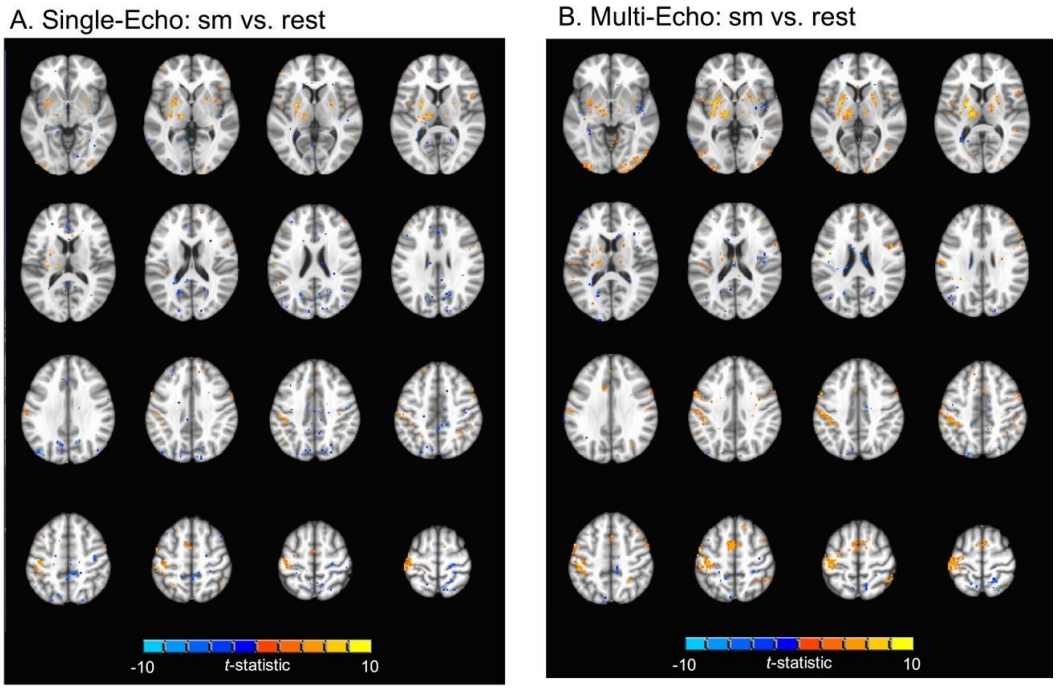

Figure S2: Group activation maps displayed on a series of axial slices for the simple movement (sm) – rest contrast. (A) Single-echo and (B) multi-echo group *t*-statistic maps, both thresholded at a FDR-corrected $q<0.05$.

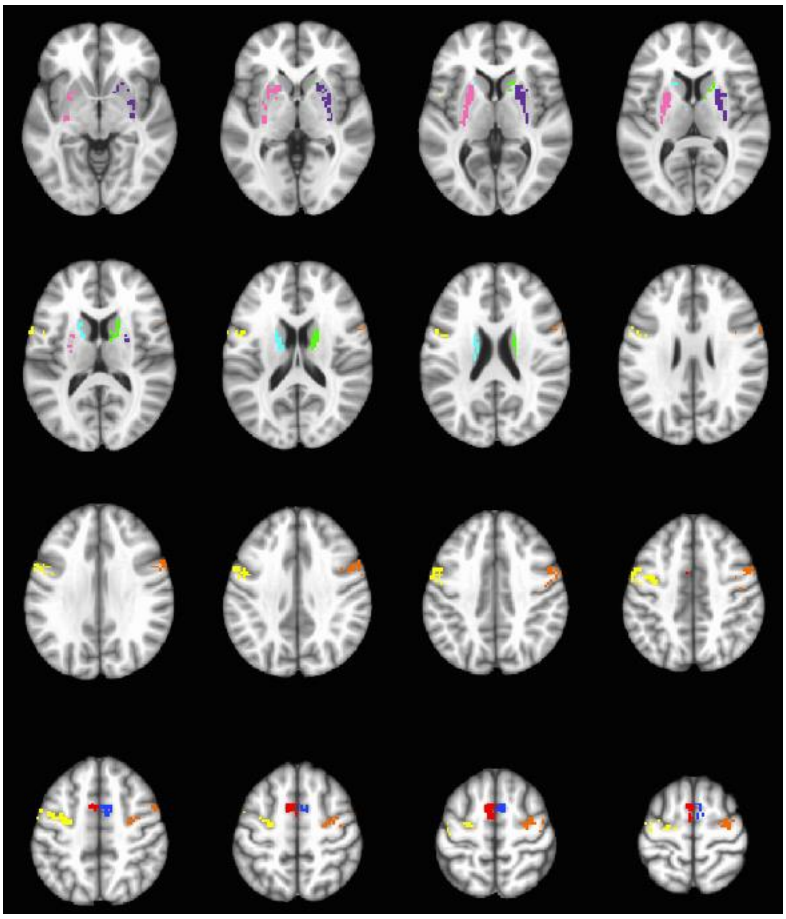

Figure S3: Functionally-defined ROIs on a series of axial slices. Colors represent different ROIs: yellow = left M1, orange = right M1, red = left SMA, blue = right SMA, cyan = left CN, green = right CN, pink = left PUT, purple = right PUT. Note that the ROIs are shown on the same montage of slices displayed in Figure 2-3, Figure **S1** and Figure **S2**.

Chapter 3

Serial correlations in single-subject fMRI with sub-second TR

Saskia Bollmann[1], Alexander M. Puckett[2], Ross Cunnington[2,3], Markus Barth[1]

[1]Centre for Advanced Imaging, The University of Queensland, Brisbane QLD 4072, Australia

[2]Queensland Brain Institute, The University of Queensland, Brisbane QLD 4072, Australia

[3]School of Psychology, The University of Queensland; Brisbane QLD 4072; Australia

Keywords

fMRI analysis

autocorrelation

simultaneous multi-slice

autoregressive model

physiological noise

Variational Bayes

Abstract

When performing statistical analysis of single-subject fMRI data, serial correlations need to be taken into account to allow for valid inference. Otherwise, the variability in the parameter estimates might be under-estimated resulting in increased false-positive rates. Serial correlations in fMRI data are commonly characterized in terms of a first-order autoregressive (AR) process and then removed via pre-whitening. The required noise model for the pre-whitening depends on a number of parameters, particularly the repetition time (TR). Here we investigate how the sub-second temporal resolution provided by simultaneous multislice (SMS) imaging changes the noise structure in fMRI time series. We fit a higher-order AR model and then estimate the optimal AR model order for a sequence with a TR of less than 600 ms providing whole brain coverage. We show that physiological noise modelling successfully reduces the required AR model order, but remaining serial correlations necessitate an advanced noise model. We conclude that commonly used noise models, such as the AR(1) model, are inadequate for modelling serial correlations in fMRI using sub-second TRs. Rather, physiological noise modelling in combination with advanced pre-whitening schemes enable valid inference in single-subject analysis using fast fMRI sequences.

3.1 Introduction

In functional MRI (fMRI), blood-oxygen-level-dependent (BOLD)-weighted images are acquired in a rapid, successive fashion depicting changes in deoxyhemoglobin content in the brain over time (Bandettini et al., 1992; Kwong et al., 1992; Ogawa et al., 1992). The signal of interest is the time series in each voxel comprising the local hemodynamic response (Boynton et al., 1996; Buxton et al., 1998; Fox et al., 1988). A statistical model is then applied to draw an inference about the effect of an experimental manipulation and its significance. In this process, serial correlations, i.e. correlations between the errors of successive samples, need to be taken into account for valid inference.

Statistical analysis of fMRI time series is often performed using a mass-univariate general linear model to assess the effect of a task in each voxel (Friston et al., 1994). The basic model at each voxel reads $Y = Xw + e$; where Y are the observations (data), X is the design matrix containing the explanatory variables, w are the (unknown) parameters on which the inference is based and e is the error following a normal distribution with $e \sim N(0, \sigma^2 V)$ (Kiebel and Holmes, 2007). Here, V describes the serial correlations over time. When performing a statistical test, this correlation structure needs to be taken into account to obtain the desired false-positive rate, such that the estimated variance of $\hat{w}$ is not biased, and too liberal thresholds are prevented (Purdon and Weisskoff, 1998; Woolrich et al., 2001; Worsley et al., 2002). Importantly, the estimate of w itself remains unbiased but becomes more variable when disregarding serial correlations in the data (Wooldridge, 2013; Worsley et al., 2002). Serial correlations initially reduce the effective degrees of freedom (Worsley and Friston, 1995), and pre-whitening[4] is traditionally performed to remove the serial correlations from the data and the model (Woolrich et al., 2001).

In combination with physiological noise modelling, pre-whitening using an autoregressive (AR) model of order 1 has been a successful strategy to improve the validity of drawn

[4]Pre-whitening relies on accurate knowledge of the error covariance matrix V, which depends on a number of (scan) parameters and is therefore usually estimated from the data itself. The error covariance matrix contains the variance of the error signal with itself shifted by increasing time lag τ (Friston et al., 1994). The parameter estimation is performed in two steps. First, the residuals $r = Y - X\hat{w}$ are estimated using ordinary least squares, i.e. the pseudoinverse X^- of the design matrix is used to estimate $\hat{w} = X^- Y$. The covariance matrix V can then be estimated from the residuals, choosing between several parametric and non-parametric methods (Woolrich et al., 2001) with negligible bias (Marchini and Smith, 2003). Within the SPM framework (http://www.fil.ion.ucl.ac.uk/spm/), Restricted Maximum Likelihood (ReML) is used to estimate the hyperparameters λ modelling the serial correlations. Variance estimates tend to be very noisy (Woolrich et al., 2001; Worsley et al., 2002), and it is therefore assumed that the covariance matrix $V(\lambda)$ is the same in all voxels and only the variance σ^2 differs between voxels, i.e. the pattern of serial correlations is the same in all voxels, but its amplitude is different at each voxel. This allows the pooling across voxels to give a highly precise estimate, and the error covariance matrix is then treated as a known quantity in the subsequent inference (Glaser and Friston, 2007). Since ReML requires a linear model for V, a first-order linear approximation of an autoregressive (AR) process of order 1 around the expansion point of $a_1 = 0.2$ is used to model the error covariance. Second, V is then used to form the pre-whitening matrix $M = V^{-1/2}$ giving $MY = MXw + z$ with $z \sim N(0, \sigma^2 I)$ and $z = Me$. This model now conforms to the sphericity assumption and the degrees of freedom revert to their classical values.

inferences for fMRI time series with a repetition time (TR) above 2 seconds (Lund et al., 2006). Similarly, Worsley et al. (2002) found an AR(1) to be adequate for most voxels. However, it has been hypothesized that a higher AR model order might be required to reliably capture serial correlations for data sets with considerably shorter TRs (Lund et al., 2006). Given the recent acceleration of echo-planar imaging (EPI) employing simultaneous multislice (SMS) techniques (Breuer et al., 2005; Larkman et al., 2001; Setsompop et al., 2012) - for a recent review see Barth et al. (2016) - one can now easily achieve sub-second temporal resolution for whole-brain acquisitions (Feinberg et al., 2010; Moeller et al., 2010). Hence, it is becoming increasingly important to address the effect of short TRs in fMRI analyses. Increased false-positive rates were observed empirically in resting-state data with a TR of 1 second but without physiological noise modelling (Eklund et al., 2012). Similarly, when using higher AR-model orders for pre-whitening in an event-related paradigm, a reduction in t-values was found for sequences with TRs below 2 seconds (Sahib et al., 2016). However, the underlying mechanisms and sources of serial correlations remain unknown. Therefore, we investigate serial correlations in fMRI time series with sub-second TR achieved using SMS EPI to assess changes in the noise correlation structure that need to be taken into account for valid inference.

We characterize serial correlations in terms of an AR process, and use the Variational Bayesian (VB) framework for fMRI time series (Penny et al., 2003) to estimate the optimal AR model order required for a short-TR sequence. VB implements Bayesian statistics for neuroimaging and offers a framework for parameter estimation complementary to classical statistics (Friston et al., 2002). Pertinent to the present study, the classical general linear model is extended by introducing an AR noise process of arbitrary order p. Instead of computing a pre-whitening matrix, serial correlations are explicitly modelled and integrated into the parameter estimation. The statistical model now reads $Y = XW + E$, where Y is the $[T \times N]$ data matrix, X is the $[T \times K]$ design matrix, W is a $[K \times N]$ matrix of regression coefficients and E is the $[T \times N]$ error matrix for N voxels at T points in time using K regressors (Penny et al., 2007, 2005). This constitutes a spatio-temporal model of the fMRI data to directly incorporate dependencies between voxels (Penny et al., 2005). The autoregressive process at voxel n is modelled as $y_n = Xw_n + e_n$, with $e_n = \tilde{E}_n a_n + z_n$. Here, e_n models an AR process where a_n are the AR coefficients, $\tilde{E}_n$ are the 'embedded' errors, i.e. the error of p previous samples, and z_n describes independent and identically distributed Gaussian errors. The priors over the regression and AR coefficients are used to model spatial dependencies across voxels, whereas the posterior factorizes over voxels and

parameter types making the update equations tractable (Penny et al., 2005). Using the VB framework, model parameters are estimated by maximizing the free energy F, which constitutes a lower bound on the model evidence, and can be used for Bayesian model selection to obtain the optimal AR model order (Penny et al., 2003). Therefore, VB is well suited to estimate the AR coefficients and to choose an optimal noise model.

As mentioned previously, physiological noise modelling can improve the validity of drawn inferences using fMRI data by reducing the required AR model order (Lund et al., 2006). Signal fluctuations related to cardiac and respiratory activity have been identified as major sources of structured noise in fMRI data (Bianciardi et al., 2009; Hutton et al., 2011). Signal fluctuations related to respiration enter the fMRI time series signal either through changes in venous oxygenation content (Windischberger et al., 2002) or through modulation of the main magnetic field (Van de Moortele et al., 2002) and higher image encoding fields (Bollmann et al., 2017; Vannesjo et al., 2015), which induce geometric distortions across the whole EPI image. Cardiac activity induces high and localized signal variability through mechanisms such as vessel pulsation (Dagli et al., 1999; Kasper et al., 2017). Physiological signal fluctuations can be modelled as a Fourier expansion of the cardiac and respiratory phase utilizing their intrinsic periodicity (Glover et al., 2000), thereby providing nuisance regressors which can then be included as covariates in the statistical analysis. Additionally, significant signal contributions related to changes in cardiac and respiratory rate have been identified causing low-frequency oscillations in fMRI time series (Birn et al., 2006, 2008; Chang et al., 2009). Another source of unwanted signal fluctuations are movement related effects (Friston et al., 1996). Changes in voxel position alter the spin history, thereby inducing signal fluctuations which can last for several seconds and depend on the voxel position in previous scans. Thus, a serially correlated signal is introduced into the fMRI time series. In summary, a range of physiological processes introduce unwanted, serially correlated signals that need to be taken into account in the modelling of fMRI time series data. Here, we investigate the impact of physiological noise modelling (including movement in addition to cardiac and respiratory activity) on the noise structure as well as on the optimal AR model order.

3.2 Materials and Methods

3.2.1 Data acquisition

MRI data were acquired on a MAGNETOM 7T whole-body scanner (Siemens Healthcare, Erlangen, Germany) with a 32-channel head coil (Nova Medical, Wilmington, US). To

achieve sufficiently short TRs, SMS EPI (Feinberg et al., 2010; Setsompop et al., 2012) was utilized to acquire multiple slices at once. The CMRR SMS implementation (release 11a) (https://www.cmrr.umn.edu/multiband/) was used and reconstruction was performed using the slice-GRAPPA technique (Setsompop et al., 2012). FMRI data were acquired with a short-TR sequence to investigate serial correlations and their interaction with physiological noise modelling. The results were then compared to those obtained from data acquired with a longer, more common TR. Imaging parameters for the short-TR sequence were: TR = 589 ms, voxel size = 2.5 mm isotropic, TE = 23 ms, SMS-acceleration-factor = 4, GRAPPA-factor = 2, FOV = 212 mm x 212 mm, number of slices = 48, number of scans = 581. Imaging parameters for the long-TR sequence were: TR = 1990 ms, voxel size = 1.3 mm isotropic, TE = 25 ms, SMS-acceleration-factor = 3, GRAPPA-factor = 3, Partial Fourier = 7/8, FOV = 212 mm x 212 mm, number of slices = 96, number of scans = 188.

3.2.2 Study design

The project was approved by the University of Queensland's Medical Research Ethics Committee. N = 10 healthy, right handed participants with normal or corrected to normal vision participated in the study after giving written, informed consent. The data were acquired as part of a larger study comparing different sequence parameter settings for fMRI at 7T. For six participants (five female), cardiac and respiratory data were recorded concurrently with the image acquisition using a breathing belt and an ECG system (Brain Products, Gilching, Germany) and their data were analysed here.

Participants performed a finger tapping task consisting of blocks of simple movement, complex movement and rest. In the simple movement condition, a visual stimulus of four dashed lines was presented and participants were asked to respond with consistent, medium length button presses of the index, middle, ring and little fingers of the right hand in sequential order. In the complex movement condition, a visual stimulus consisting of two dots and two dashed lines, indicating short and long button presses, was presented. In each block, the visual cue (2500 ms duration) followed by a fixation cross (500 ms duration) was shown six times, resulting in an 18 s block length. In the complex condition, each of the six possible combinations of two short and two long button presses were presented in a randomized order. In the rest condition, only the fixation cross was shown. For two participants, the first run of each sequence followed the order [rest - complex - simple - rest - simple - complex - repeated], while for the remaining four participants, the simple condition was presented first [rest - simple - complex - rest - complex - simple - repeated]. In total, one run of the task lasted 342 s, containing 6 blocks of rest, simple and complex movement

and an additional rest block at the end. For each sequence parameter setting, two runs of fMRI data were acquired. For the second run of each sequence, the order of movement conditions was reversed.

3.2.3 Preprocessing

Preprocessing was performed using SPM12 (r6224, Wellcome Trust Centre for Neuroimaging, London, UK) and Matlab (R2016a, The MathWorks, Inc., Natick, MA, US). For anatomical reference, an EPI image with an isotropic voxel size of 1 mm was chosen. Upon visual inspection, it provided better alignment in distortion prone areas such as frontal regions and around the ventricles than the additionally acquired T1-weighted image following the rationale in Grabner et al. (2014). To provide a robust starting point for the image segmentation, this reference image was first coregistered to the MNI305 T1 template. Next, the image was segmented using the unified segmentation algorithm (Ashburner and Friston, 2005) to retrieve tissue probability maps (TPMs) in subject space as well as the deformations field from and to MNI and subject space. The functional data were preprocessed in the following way: Realignment using the two-pass procedure. Coregistration (including resampling using a 7th order B-spline) to the reference anatomical EPI image for the first run, coregistration to the mean image of the first run for the second run to improve between-run alignment. Last, smoothing of the functional images was performed using a Gaussian smoothing kernel with 5 mm full-width-at-half-maximum (FWHM) size. All analyses were performed in subject space.

3.2.4 Physiological noise modelling

Peripheral ECG data were preprocessed using an in-house implementation and the fieldtrip toolbox (Oostenveld et al., 2011) for data read-in. Following the recommendations in Ritter et al. (2007), a simple gradient artefact correction was used fitting an offset and a moving average template (computed from the current, the previous and following 4 scans), followed by low-pass filtering and downsampling to 100 Hz. Preprocessed cardiac and raw breathing data were used to compute the Fourier expansion of cardiac and respiratory phase (Glover et al., 2000) as implemented in the physIO toolbox (Kasper et al., 2017) with a cardiac model order of 3, a respiratory model order of 4, and an interaction model order of 1 (Harvey et al., 2008). Changes in respiratory and cardiac rate were modelled using the respiration response function (RRF) (Birn et al., 2008) and cardiac response function (CRF) (Chang et al., 2009), respectively. Following the recommendations in Chang et al. (2009) and Falahpour et al. (2013), and to accommodate the (negative) latency of -8 s between the

estimated RRF from the breath-hold experiments and the rest data found in Birn et al. (2008), specific delay values were estimated for the RRF and CRF for each individual participant. Based on the latencies reported in Birn et al. (2008), delay values of -12, -8, -4, 0, 4, 8 and 12 s were examined. The response delay for each participant was then defined based on the highest number of supra-threshold voxels obtained in an F-test for each response function using the first short-TR run of each subject. To model remaining signal fluctuations related to movement, the Volterra expansion of the realignment parameters was used (Friston et al., 1996). The derivative, square and squared derivative of the realignment parameters totalling 24 regressors were estimated for the short-TR sequence.

3.2.5 Model estimation and analysis

Two task regressors for the simple and complex movement condition were constructed by specifying the respective onsets and duration (18s) of each block. The resulting box functions were then convolved with the canonical hemodynamic response function using the standard parameters provided in SPM12 and its temporal and dispersion derivatives.

To investigate the impact of physiological noise modelling, the estimation process was repeated with four different sets of nuisance regressors: (i) ‘no phys’ uses the realignment and task regressors, but no physiological noise regressors, (ii) ‘RETROICOR’ adds the physiological noise regressors as described in the RETROICOR model (Glover et al., 2000) to the task and realignment regressors, (iii) ‘RETROICOR + RRF + CRF’ incorporates the RETROICOR regressors and RRF (Birn et al., 2008) and CRF (Chang et al., 2009), (iv) ‘RETROICOR + Volterra’ contains RETROICOR regressors in combination with the Volterra expansion of the realignment parameters (Friston et al., 1996) for the short-TR sequence.

Similar to previous studies, the short-TR sequence was downsampled by a factor of 4 to create an artificial long-TR sequence (Boyacioğlu et al., 2015; Todd et al., 2017). Thereby, an fMRI time series that matches the spatial resolution of the short-TR sequence but has the temporal characteristics as if it were acquired with a TR of 2356 ms was obtained. This permitted the effect of serial correlations to be investigated on a downsampled short-TR sequence with otherwise identical signal properties compared to the short-TR sequence and on the long-TR sequence in a more realistic setting when taking full advantage of current imaging capabilities.

Bayesian model estimation was then performed to investigate the strength and characteristics of serial correlations in the fMRI time series. To this end, the VB framework (Penny et al., 2003, 2005) was used to compute log model evidence maps, containing the contribution to the overall model evidence from each voxel (Penny et al., 2007), for different

AR model orders ranging from 1 to 10. This enabled the determination of the optimal AR model order in each voxel required to model the serial correlations in the fMRI data. In addition, the impact of physiological noise modelling on serial correlations was investigated by using the four different sets of nuisance regressors described above. An uninformative (flat) signal prior and unweighted graph Laplacian (Harrison et al., 2007, 2008) noise priors were chosen for the Bayesian model estimation which was performed in a slice-by-slice fashion. To include the same data for different AR model orders, and thereby to allow a comparison between log model evidence maps, the first $p-1$ scans with p being the respective AR model order were removed from the data (Penny et al., 2003). The optimal AR model order for every voxel was determined as the AR model with the highest log model evidence for each set of nuisance regressors. To examine the evidence for a higher order AR-model in the presence of physiological noise modelling, log Bayes factors comparing AR model orders 4 to 1 were computed as the difference of the respective log model evidences (Kass and Raftery, 1995) for the 'RETROICOR + RRF + CRF' model for all three sequences and, in addition, the 'RETROICOR+Volterra' model for the case of the short-TR sequence.

The optimal AR model order was then summarized by computing the mean distribution of the voxel count over all subjects and runs in 6 different regions of interest (ROIs). The voxel count (in %) represents the number of voxel with AR model order 1 to 10 being the winning model, i.e. having the highest log model evidence, divided by the total number of voxel in each region. The 6 ROIs comprised the three tissue classes cerebrospinal fluid (CSF), grey matter (GM) and white matter (WM) as well as three regions expected to be involved in the task, i.e. primary motor cortex (M1), supplementary motor area (SMA) and putamen (Bednark et al., 2015). The cortical ROIs M1 and SMA were defined using the Harvard-Oxford cortical structural atlas as distributed with the FMRIB Software Library (Desikan et al., 2006; Frazier et al., 2005; Goldstein et al., 2007; Makris et al., 2006). The ROI for the putamen was derived from high-resolution 7T imaging (Keuken et al., 2014; Tziortzi et al., 2011). The ROIs were limited to grey matter by multiplying each ROI with a grey matter mask derived by thresholding the grey matter TPM at 0.9.

To visualize the noise characteristics fitted by the different AR models, their power spectra were estimated using the SPM function spm_ar_freq.m. For each voxel, the AR coefficients of the winning model were extracted and the spectra estimated. For each AR model order, the obtained spectra were then averaged and compared across the four different noise modelling schemes. Additionally, the spectrum when using an AR model of order 1 was compared to the spectrum using the optimal AR model.

Classical model estimation was performed to investigate the spectrum of the residuals visualizing the impact of physiological noise modelling and pre-whitening on the frequency content of the image time series and providing insight into possible remaining noise sources. Therein, the two different pre-whitening strategies as provided in SPM 12 were used: either the AR(1) or the FAST model, which uses a dictionary of covariance components based upon exponential covariance functions. Likewise as for the Bayesian model estimation, classical model estimation was performed for the four different noise modelling schemes with either of the pre-whitening options. The average amplitude spectrum of all grey matter voxels was then computed from the residual time series obtained after model fitting.

In summary, Bayesian model estimation was performed using data with three TRs (589 ms, 1990 ms and 2356 ms), and four noise modelling methods (no phys; RETROICOR; RETROICOR + RRF + CRF, RETROICOR + Volterra). Similarly, classical model estimation was performed using either an AR(1) model or the FAST option in SPM for pre-whitening. To investigate the effect of spatial smoothing, the analysis was repeated on the un-smoothed data obtained with the short-TR sequence.

3.3 Results

3.3.1 Optimal AR model orders and the impact of physiological noise modelling

To investigate serial correlations and the effect of physiological noise modelling for the short-TR sequence, optimal AR model orders obtained for the four noise modelling schemes are illustrated in Figure 3-1. A high optimal AR model order of up to 10 was found in large areas, especially in CSF and grey matter regions, when no physiological noise modelling was performed (Figure 3-1, 1st column). This indicates a complex, non-white noise structure in the fMRI time series. Including RETROICOR regressors to model cardiac and respiratory signal fluctuations successfully reduced the optimal AR model order to approximately 4 and below (Figure 3-1, 2nd column). High AR model orders remained in ventricles and anterior and posterior tissue-air boundaries. Additional regressors for variations in cardiac rate and respiration ('RETROICOR + RRF + CRF') had a localized effect (white arrow in Figure 3-1, 3rd column). Including additional movement regressors ('RETROICOR + Volterra') mainly reduced optimal AR model orders at the anterior and posterior tissue-air boundaries (white arrows in Figure 3-1, 4th column). In general, white matter areas showed lower AR model orders, with some voxel having an optimal AR model order of 1.

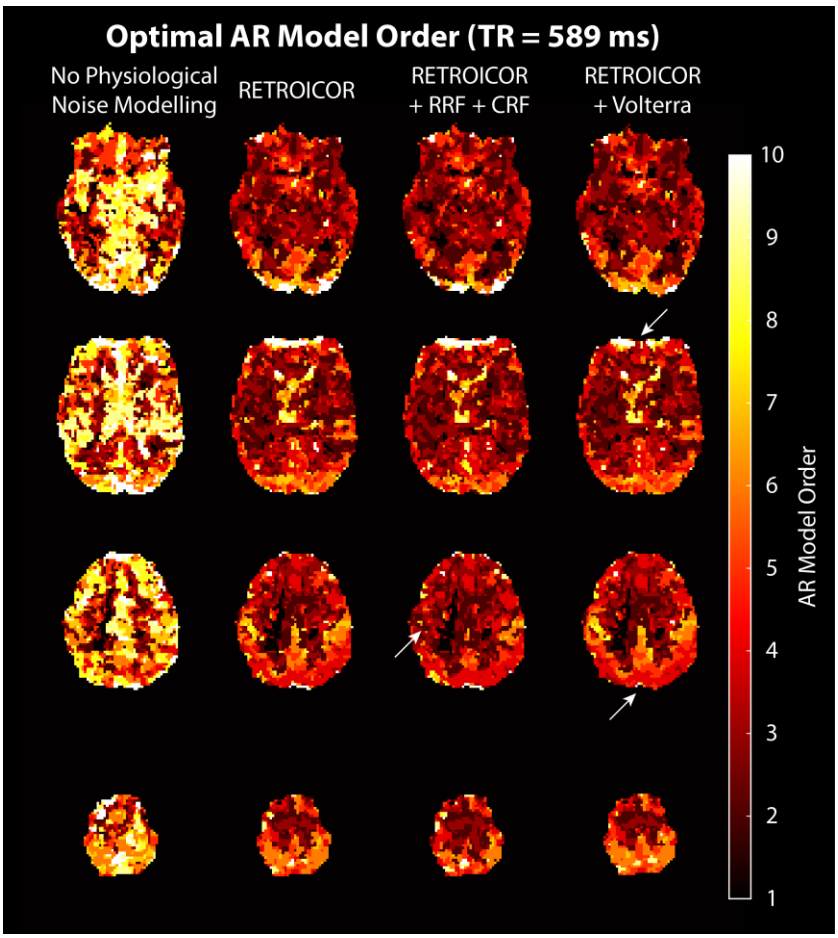

Figure 3-1: Estimated optimal AR model orders for the short-TR sequence without physiological noise modelling (1st column), with RETROICOR regressors (2nd column), with RETROICOR regressors and cardiac and respiration response function modelling (3rd column) and with RETROICOR regressors and Volterra expansion of the realignment parameters (4th column) illustrated on the example of 4 axial slices (subject 1, run 1, TR = 589 ms, 2.5×2.5×2.5 mm3, smoothed with a 5 mm FHWM Gaussian kernel). The white arrows indicate a local reduction of optimal AR model orders for the RETROICOR + RRF + CRF noise model (3rd column) and a reduction of optimal AR model orders at anterior and posterior tissue-air boundaries for the RETROICOR + Volterra noise model (4th column).

The distribution of optimal AR model orders shows the impact of physiological noise modelling for different tissue classes and in different cortical and subcortical regions (Figure 3-2): Grey matter had a large number of voxels with a high optimal AR model order without physiological noise modelling, i.e. 37 % of the voxels had an optimal AR model order > 5 (Figure 3-2, top left). For comparison, 48 % of the voxels in CSF (Figure 3-2, centre left), but only 20 % of the voxels in white matter had an optimal AR model order > 5 (Figure 3-2, top bottom). Including RETROICOR regressors had the largest impact reducing the number of voxels with optimal AR model order > 5 to 16 % in grey matter, 21 % in CSF, and 10 % in white matter. Adding RRF + CRF regressors further reduced this amount by 1 % in all three tissue classes. Additional movement regressors had a slightly larger impact, reducing the number of voxels with optimal AR model orders > 5 to 14 % in grey matter, 17 % in CSF and 9 % in white matter. In total, 68 % of the grey matter voxels had an AR optimal model

order ranging between 2 and 4 when using the RETROICOR noise modelling scheme (Figure 3-2, top left). The highest voxel count in grey matter was obtained for an AR model order of 4, with 28 % favouring this AR model under the RETROICOR + Volterra noise modelling scheme. Interestingly, the voxel count for an optimal AR model order of 1 was < 7 % in all three tissue classes even with physiological noise modelling.

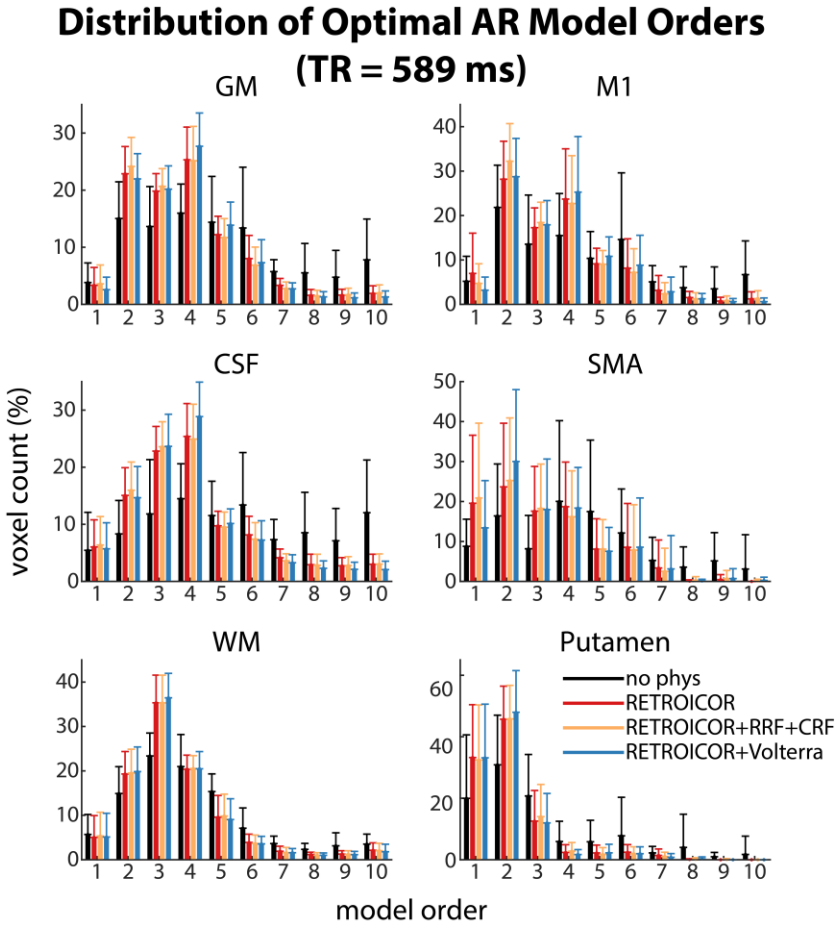

Figure 3-2: Distribution of optimal AR model orders. Mean and standard deviation across subjects and runs of the voxel count (%) for each optimal AR model order in 6 different regions-of-interest without physiological noise modelling (black), with RETROICOR regressors (red), with RETROICOR regressors and cardiac and respiration response function modelling (orange) and with RETROICOR regressors and Volterra expansion of the realignment parameters (blue) for the short-TR sequence (TR = 589 ms, 2.5×2.5×2.5 mm^3, smoothed with a 5 mm FHWM Gaussian kernel). The voxel count represents the number of voxel with AR model order 1 to 10 being the winning model, i.e. having the highest log model evidence, divided by the total number of voxel in each region.

The grey matter voxels in M1 and SMA showed comparable properties with regard to voxel count and impact of physiological noise modelling as the whole grey matter. When including RETROICOR regressors 69 % of the voxels in M1 supported an optimal AR model order between 2 and 4, and only 15 % supported an AR model order > 5 (Figure 3-2, top right). Similarly in SMA, 60 % of the voxels supported an optimal AR model order between 2 and 4 and only 12 % supported an AR model order > 5. (Figure 3-2, centre right). However, the voxel count for an optimal AR model order of 1 (20 %) was much higher than in the

previously discussed ROIs. Including additional regressors for cardiac and respiration response modelling (RETROICOR + RRF + CRF) or additional movement regressors (RETROICOR + Volterra) had a smaller impact giving results comparable to the RETROICOR noise model. The distribution of optimal AR model orders in the putamen showed a different pattern, with a maximum of 46 % supporting an AR model order of 2 and only 9 % of the voxels with an optimal AR model order > 3 when including the RETROICOR regressors (Figure 3-2, bottom right). As in the SMA, the voxel count supporting an AR model order of 1 (33 %) was much higher than in the whole grey matter.

In summary, tissue-class and region-specific distributions of optimal AR model orders were found. Including physiological noise regressors successfully reduced the number of voxel with high AR model orders and, consequently, increased the voxel count with low optimal AR model orders. Nevertheless, an AR model of order 1 proved insufficient for most voxels. Most grey matter areas still had an optimal AR model order ranging between 2 and 4.

In comparison, optimal AR model orders for the long-TR sequence remained low, with the majority of voxels having an optimal AR model order of 1 or 2 even without physiological noise modelling (Figure 3-3A, left column). Elevated AR model orders were observed in the vicinity of the circle of Willis and the ventricles, but also close to the insula and the anterior cingulate cortex (white arrows in Figure 3-3A, left column). Including regressors for physiological noise successfully reduced the optimal AR model order in these areas (Figure 3-3A, centre and right column), with virtually no difference between RETROICOR regressors only and the ‘RETROICOR + CRF + RRF’ noise modelling scheme. Optimal AR model orders for the downsampled short-TR sequence (Figure 3-3B) exhibited nearly identical characteristics as for the long-TR data. Slightly higher AR model orders were observed in a small number of voxels without physiological noise modelling (Figure 3-3B, left column). When including physiological noise regressors, low optimal AR model orders of 1 or 2 were obtained (Figure 3-3B, centre and right column).

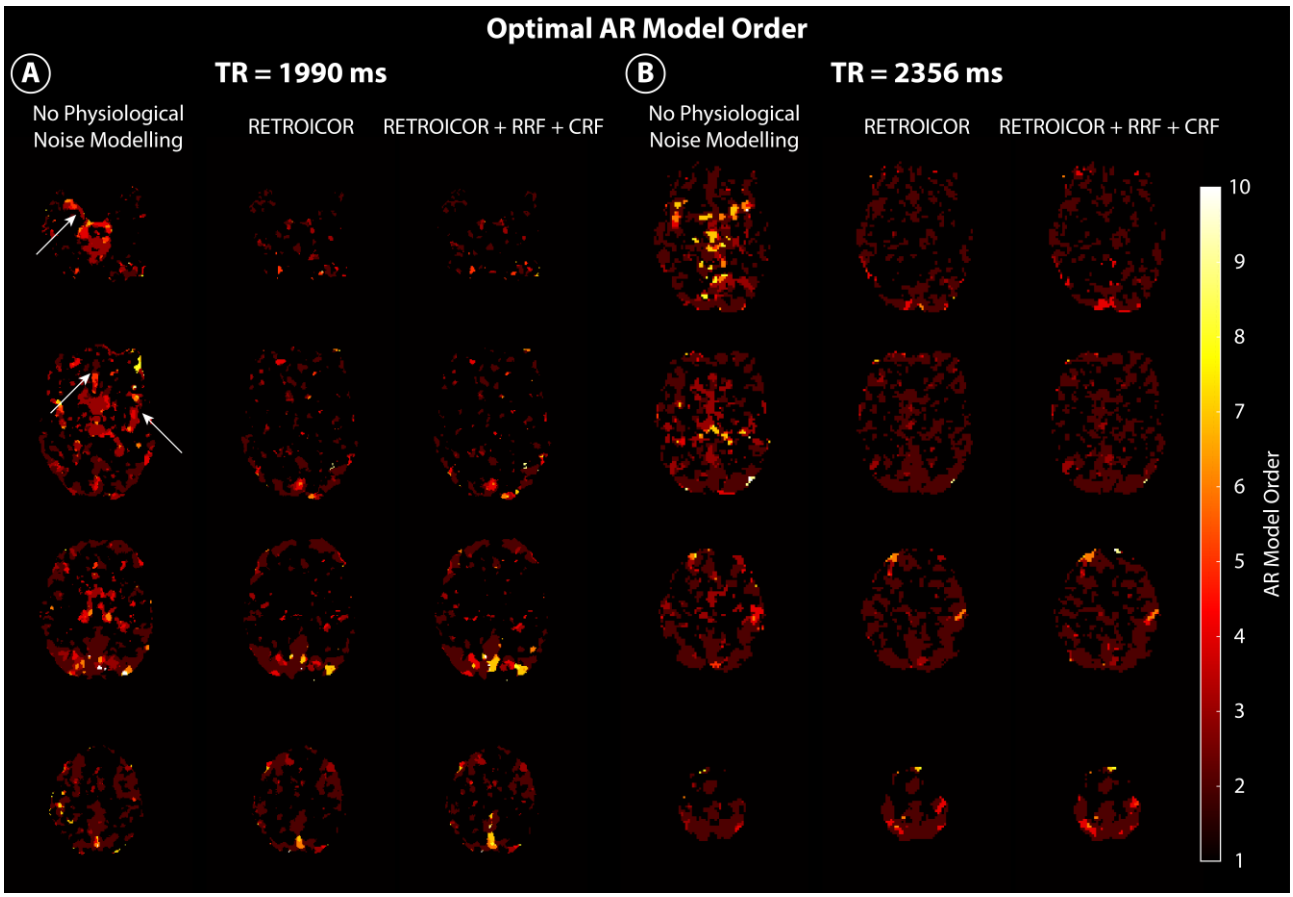

Figure 3-3: Estimated optimal AR model orders for the long TR sequence. Estimated optimal AR model orders without physiological noise modelling (LEFT), with RETROICOR regressors (CENTRE) and with RETROICOR regressors and cardiac and respiration response function modelling (RIGHT) for (A) the long-TR sequence (subject 1, run 1, TR = 1990 ms, 1.3×1.3×1.3 mm^3, smoothed with a 5 mm FWHM Gaussian kernel) and (B) the downsampled short-TR sequence (subject 1, run 1, TR = 2356 ms, 2.5×2.5×2.5 mm^3, smoothed with a 5 mm FWHM Gaussian kernel). The white arrows indicate elevated AR model orders obtained without physiological noise modelling in the vicinity of the circle of Willis, the insula and the anterior cingulate cortex.

The voxel count across subjects and runs for the long-TR sequences showed a majority of voxel with an optimal AR model order of 1 (Figure 3-4A). Even without physiological noise modelling, 45 % of the grey matter (Figure 3-4A, top left), 39 % of the CSF (Figure 3-4A, centre left), and 74 % of the white matter voxels (Figure 3-4A, bottom left) had an optimal AR model order of 1. These numbers were increased to 52% for grey matter and CSF, and 81 % for white matter voxels when including 'RETROICOR + CRF + RRF' regressors. Accordingly, the number of voxels with optimal AR model order > 3 was below 6 % in all three tissue classes. The distribution of optimal AR model orders in M1 and SMA grey matter voxels mimicked the characteristics observed in the whole grey matter (Figure 3-4A, top and centre right). As observed for the short-TR sequence, the distribution in the putamen is distinct from the previous ROIs and resembled features comparable to white matter voxels with 85 % of the voxels having an optimal AR model of order 1 when including RETROICOR + RRF + CRF regressors (Figure 3-4A, bottom right). This number was only slightly reduced

(to 80 %) when no physiological noise modelling was performed. Optimal AR model orders for the downsampled short-TR sequence follow a similar distribution, but with slightly higher values for AR model order 2 (Figure 3-4B). Including RETROICOR + RRF + CRF regressors, 49 % of the voxel in CSF (Figure 3-4B, top left), 51 % of the voxel in grey matter (Figure 3-4B, centre left) and 70 % of the voxel in white matter (Figure 3-4B, bottom left) had an optimal AR model order of 1. The number of voxels with optimal AR model order > 3 was below 3 % in all three tissue classes. Again, M1 (Figure 3-4B, top right) and SMA (Figure 3-4B, centre right) had comparable properties as the whole grey matter, with 51 % and 43 % of the voxel having an optimal AR model order of 1. Similarly, the highest number of voxels with optimal AR model order 1 (80 %) were found in the putamen.

In summary, the choice of the physiological noise modelling scheme has limited influence on the optimal AR model order for the long-TR sequence and the downsampled short-TR sequence, with largest effects in CSF and grey matter regions. A majority of voxel have an optimal AR model order of 1 or 2 even in the absence of physiological noise modelling.

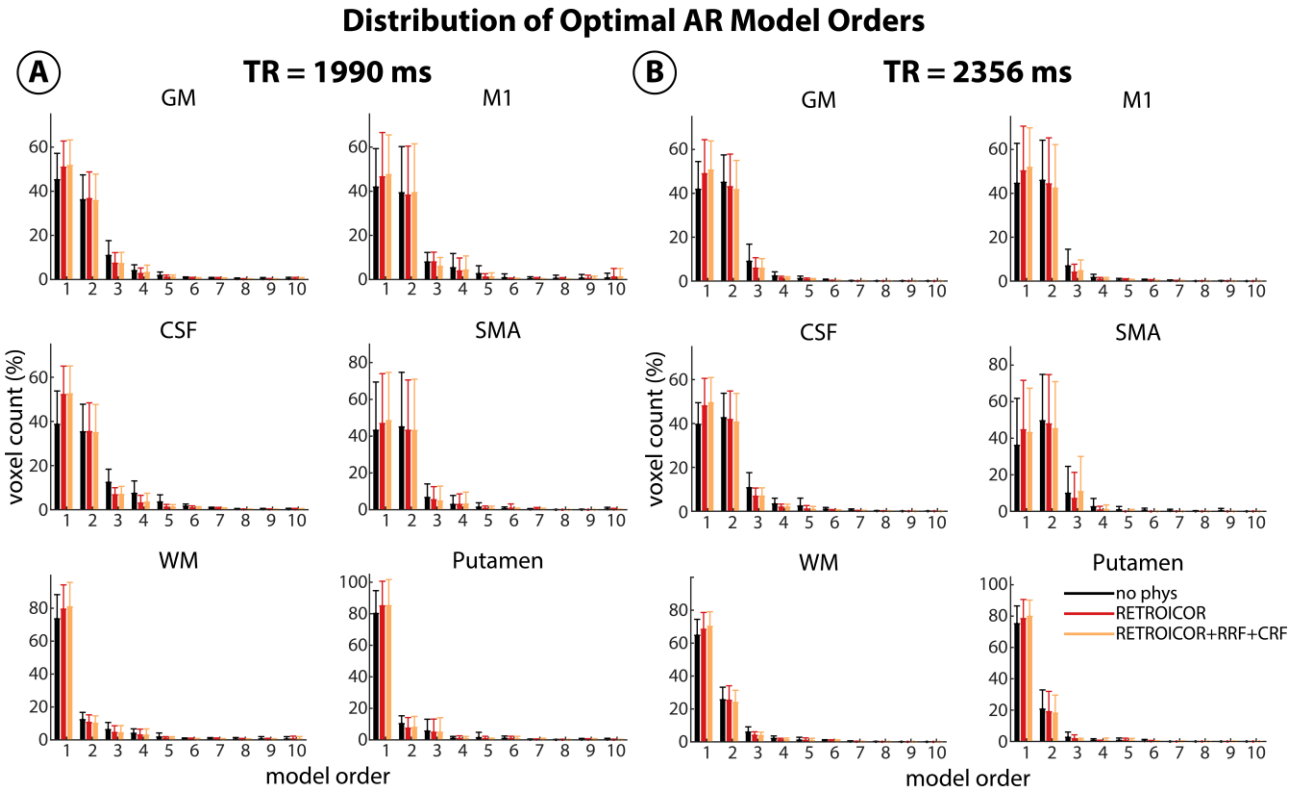

Figure 3-4: Distribution of optimal AR model orders. Mean and standard deviation across subjects and runs of the voxel count (%) for each optimal AR model order in 6 different regions-of-interest without physiological noise modelling (black), with RETROICOR regressors (red), and with RETROICOR regressors and cardiac and respiration response function modelling (orange) for (A) the long-TR sequence (TR = 1990 ms, 1.3×1.3×1.3 mm^3, smoothed with a 5 mm FWHM Gaussian kernel) and (B) the downsampled short-TR sequence (TR = 2356 ms, 2.5×2.5×2.5 mm^3, smoothed with a 5 mm FWHM Gaussian kernel). The voxel count represents the number of voxels with AR model order 1 to 10 being the winning model, i.e. having the highest log model evidence, divided by the total number of voxels in each region.

3.3.2 Bayes factor analysis

To assess the statistical significance of the obtained optimal orders, log Bayes factors were computed as the difference in log model evidence (Kass and Raftery, 1995). For the short-TR sequence, log Bayes factors comparing an AR model of order 4 to an AR model of order 1 showed positive evidence (BF > 3, corresponding to a posterior model probability > 95 %) for the higher AR model order in large areas of the brain, even when including RETROICOR + RRF + CRF (Figure 3-5, 1st column) or RETRICOR + Volterra regressors (Figure 3-5, 2nd column). Some white matter voxel showed support for the AR(1)-model as expected from Figure 1, where AR(1) was the winning model. In contrast, for the long-TR sequence positive evidence was mostly found for the AR(1)-model, with only a few patches favouring an AR

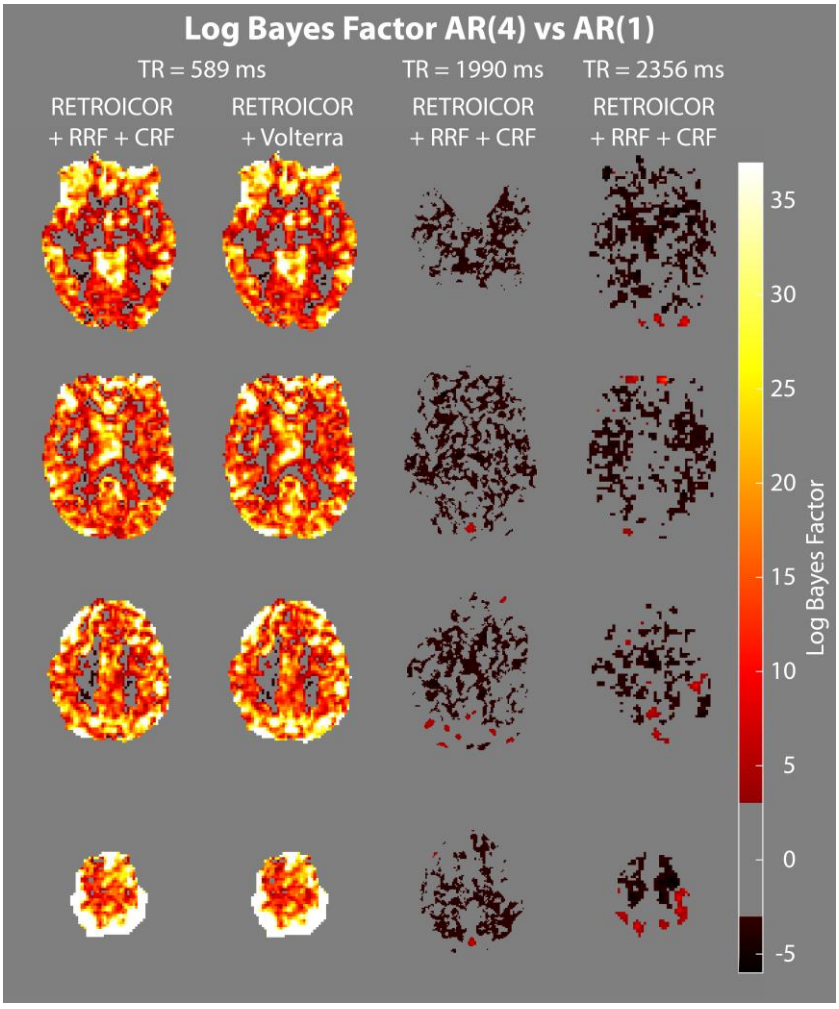

Figure 3-5: Log Bayes Factor for AR model order 4 vs. AR model order 1 for the short-TR sequence with RETROICOR regressors and cardiac and respiration response function modelling (1ST COLUMN), RETROICOR regressors and Volterra expansion of the realignment parameters (2ND COLUMN), the long-TR sequence with RETROICOR and cardiac and respiration response modelling (3RD COLUMN) and the downsampled short-TR sequence with RETROICOR and cardiac and respiration response modelling (4TH COLUMN) (subject 1, run 1, smoothed with a 5 mm FWHM Gaussian kernel). High log Bayes factors (> 3) indicate positive evidence for an AR model of order 4, whereas negative log Bayes factors below -3 indicate support for an AR model of order 1. Log Bayes factors between -3 and 3 indicate no clear evidence for either model.

model order of 4 (Figure 3-5, 3rd column). Similarly for the downsampled short-TR sequence, positive evidence was mostly found for the AR(1) model compared to the AR(4) model (Figure 3-5, 4th column). However, in large areas of the brain, log Bayes factors remain very low, indicating no clear evidence for any of the two models.

3.3.3 AR coefficient analysis

The spectra in Figure 3-6 illustrate the noise characteristics that were fitted by the different AR models. Frequencies found in the fMRI time series are down weighted, i.e. showing a dip in the estimated spectra. For example, the spectra for AR model order 10 without physiological noise modelling (Figure 3-6, 2nd column, bottom) showed a clear dip at the cardiac frequency (~ 0.66 Hz) indicating that a strong signal was present at this frequency and has been fitted by the AR model. Across all AR model orders, damping of low frequency oscillations was observed (Figure 3-6, left). Up to AR model order 4, no differences in the spectra obtained from the different noise modelling schemes were found. However, the

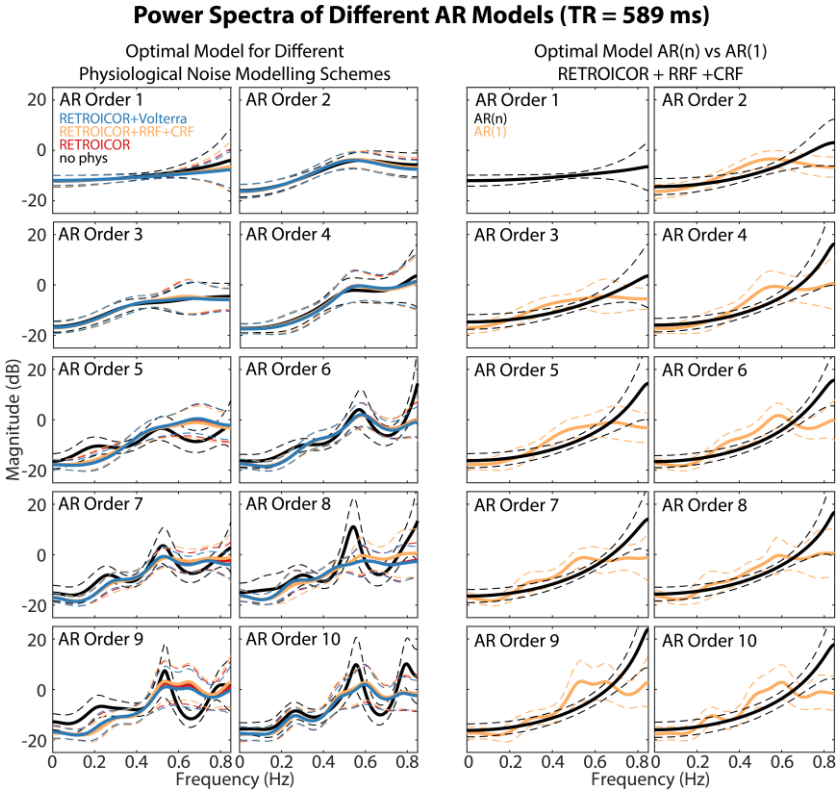

Figure 3-6: Spectrum of AR models. Spectrum (solid line = mean, dotted line = standard deviation) of different AR models in grey matter for the short-TR sequence (subject 1, run 1, TR = 589 ms, 2.5×2.5×2.5 mm^3, smoothed with a 5 mm FWHM Gaussian kernel). Spectrum without physiological noise modelling (black), with RETROICOR regressors (red), with RETROICOR regressors and cardiac and respiration response function modelling (orange) and with RETROICOR regressors and Volterra expansion of the realignment parameters (blue) when using only AR coefficients from matching optimal AR model orders (LEFT). Spectrum of AR(1) (orange) and spectrum of matching higher order models (black) when using RETROICOR regressors and cardiac and respiration response function modelling (RIGHT).

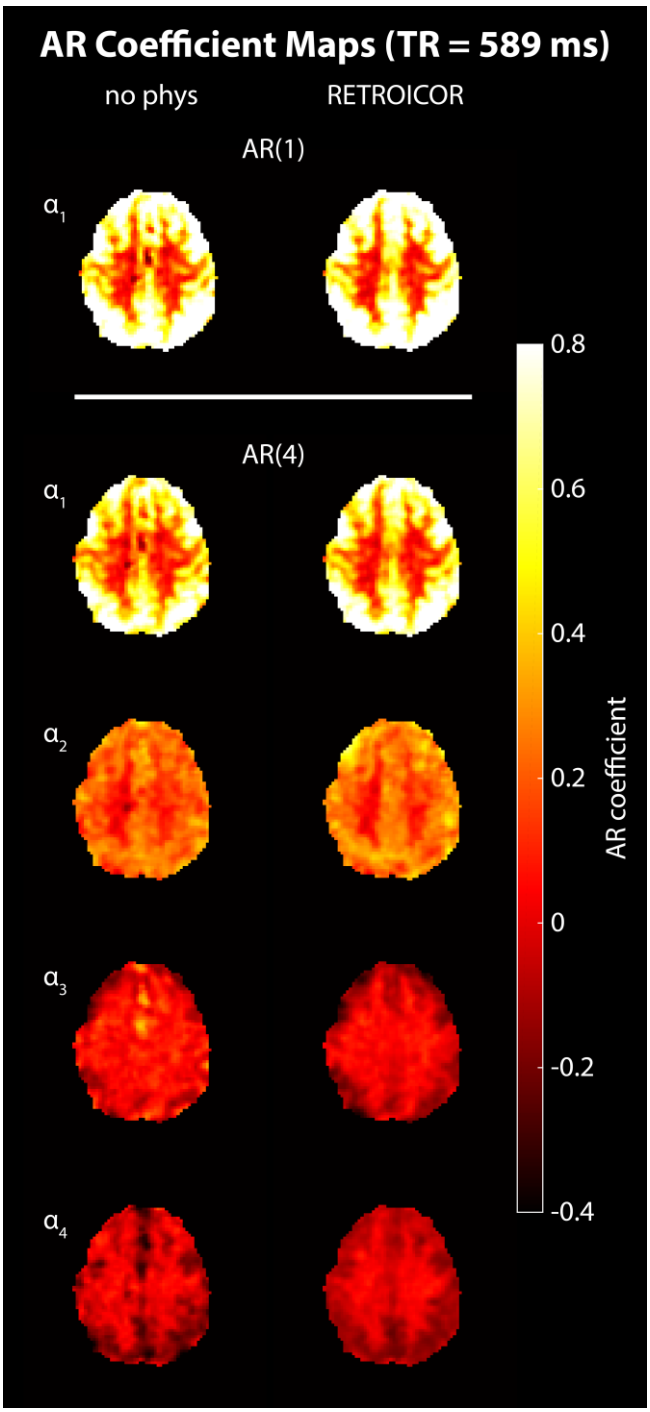

Figure 3-7: AR coefficient maps in one axial slice for an AR model of order 1 (TOP) and order 4 (BOTTOM) without physiological noise modelling (LEFT) and with the RETROICOR model (RIGHT) (subject 1, run 1, TR = 589 ms, 2.5×2.5×2.5 mm^3, smoothed with a 5 mm FWHM Gaussian kernel). High first order coefficients were found in all grey matter voxels for both AR model orders and physiological noise modelling approaches. Higher order coefficients retain anatomical structure up to 4^{th} order (BOTTOM). However, RETROICOR modelling reduces the coefficient values successfully with a more homogenous distribution of the higher order coefficients (BOTTOM, RIGHT).

spectra showed increased damping of low frequency components with increasing AR model order. For even higher AR model orders, cardiac and respiratory frequencies can be found in the spectrum, especially in the case of no physiological noise modelling. Comparing the spectrum of the winning model with the AR(1)-model when including RETOICOR, RRF and

CRF regressors shows that the AR(1)-model can only approximate the required, more complex shape of the power spectra in the voxel with higher optimal AR model order (Figure 3-6, right). The largest differences were observed for the high frequency part of the spectrum.

The estimated AR parameter maps retain anatomical structures indicative of tissue specific noise processes (Figure 3-7). High first order AR coefficients > 0.8 were obtained for the AR(1) and the AR(4) model in grey matter regions. Higher order AR coefficients were mainly present in grey matter voxels and nearly zero in white matter (Figure 3-7, bottom left). Including RETROICOR regressors reduced the higher order coefficients values, providing a more homogenous spatial distribution (Figure 3-7, bottom right).

3.3.4 Noise spectrum and FAST for pre-whitening

The average spectrum of the residual image time series visualizes remaining noise contributions after classical model estimation (Figure 3-8 and Figure 3-9). The spectrum of the 'no phys' modelling scheme was utilized to identify possible remaining noise sources. In particular, the short-TR sequence showed distinct peaks in good agreement with the measured heart and breathing rates (Figure 3-8): cardiac – 0.66Hz (aliased), respiration – 0.31 Hz, interaction – 0.35 Hz, as well as low frequency oscillations in grey matter following a 1/f characteristic. Including RETROICOR regressors successfully removed the cardiac and respiratory frequency components. The impact of the low frequency regressors modelling cardiac and respiratory variations (RETROICOR + RRF + CRF) or remaining movement-related signal fluctuations (RETROICOR + Volterra) was limited, with most of the remaining 1/f noise compared to the AR(1) model (Figure 3-8, top). Note that the cardiac and respiratory components remain in the spectrum. Adding RETROICOR regressors removed these physiological noise peaks, resulting in a nearly flat, i.e. white, noise distribution across frequencies.

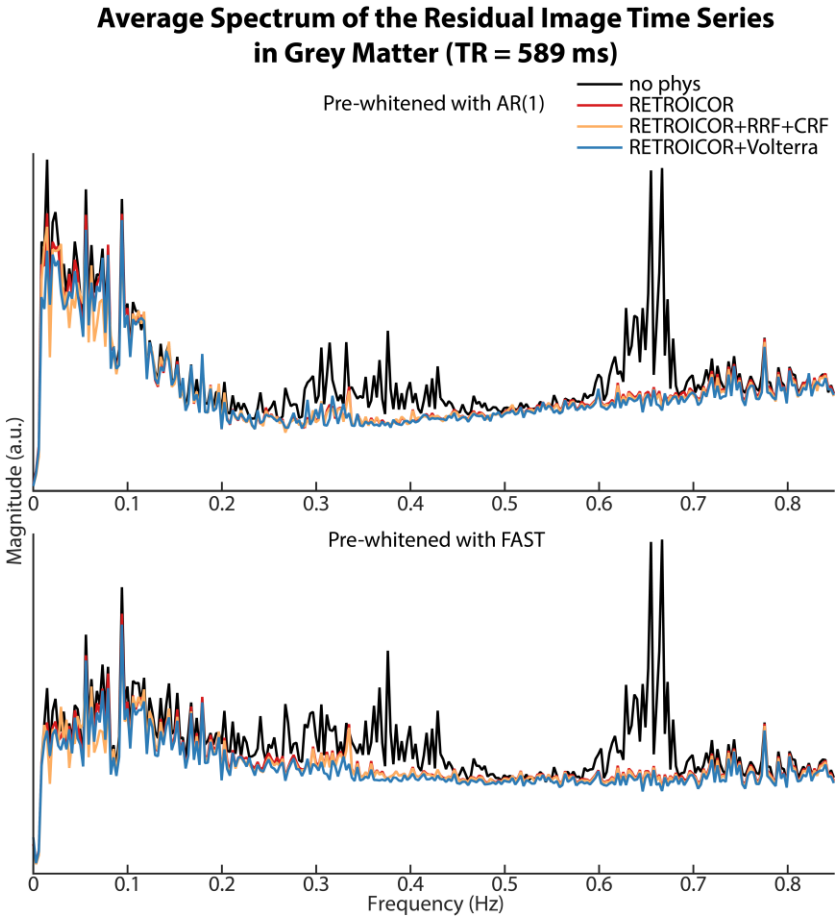

Figure 3-8: Average spectrum of the residual image time series using the classical model estimation algorithm and pre-whitening with an AR(1) model (TOP) or the FAST option (BOTTOM) without physiological noise modelling (black), with RETROICOR regressors (red), with RETROICOR regressors and cardiac and respiration response function modelling (orange) and with RETROICOR regressors and Volterra expansion of the realignment parameters (blue) for the short-TR sequence (subject 1, run 1, TR = 589 ms, 2.5×2.5×2.5 mm^3, smoothed).

The average spectrum of the long-TR sequence showed a nearly flat noise distribution across frequencies when pre-whitening with the AR(1) model (Figure 3-9A, top) or FAST (Figure 3-9A, bottom). Individual contributions from the heavily aliased physiological frequencies (0.09 Hz – cardiac, 0.16 Hz – respiration, and 0.1 Hz – interaction) could not be discerned. Including physiological noise regressors reduced the energy content across a broad range of frequencies, with only a slight reduction in peak height and number. Similarly for the downsampled short-TR sequence, both pre-whitening options resulted in a nearly flat noise distribution (Figure 3-9B) with not distinct peaks at the aliased physiological frequencies (0.18 Hz – cardiac, 0.1 Hz – respiration and 0.08 Hz – interaction).

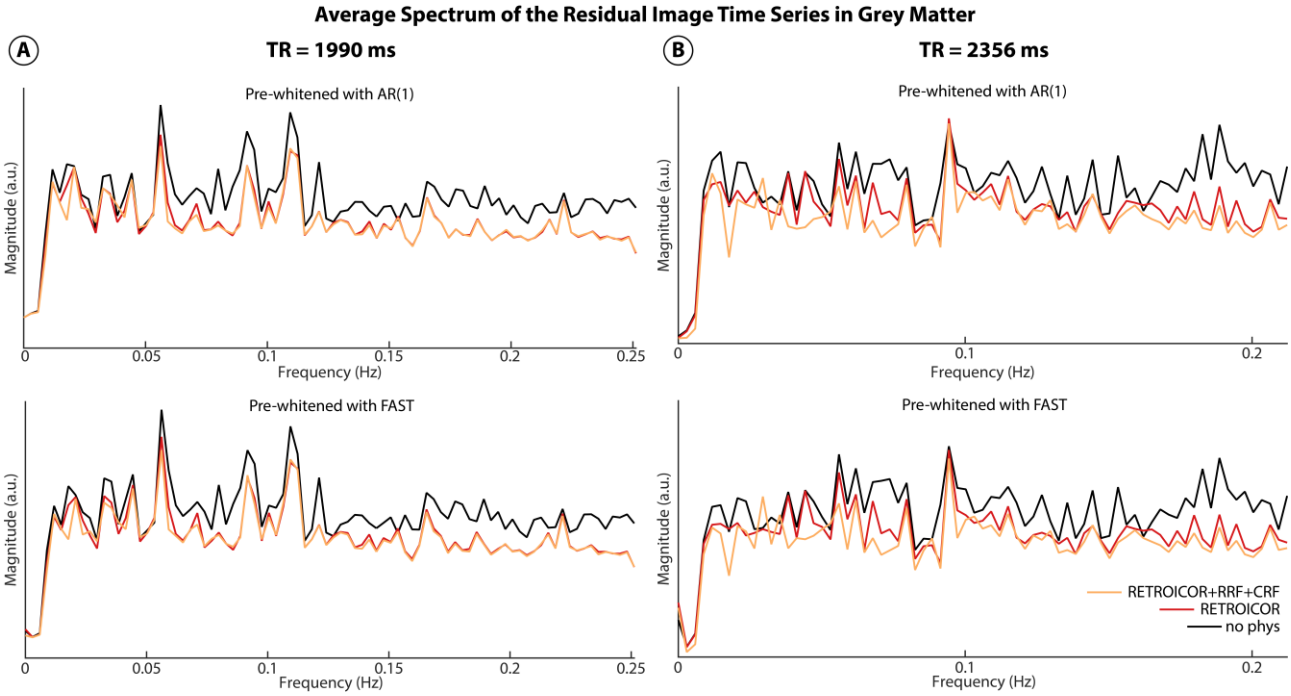

Figure 3-9: Average spectrum of the residual image time series using the classical model estimation algorithm and pre-whitening with an AR(1) model (TOP) or the FAST option (BOTTOM) without physiological noise modelling (black), with RETROICOR regressors (red) and with RETROICOR regressors and cardiac and respiration response function modelling (orange) for the long-TR sequence (A) (subject 1, run 1, TR = 1990 ms, 1.3×1.3×1.3 mm^3, smoothed with a 5 mm FWHM Gaussian kernel) and the downsampled short-TR sequence (B) (subject 1, run 1, TR = 2356 ms, 2.5×2.5×2.5 mm^3, smoothed with a 5 mm FWHM Gaussian kernel).

3.3.5 Impact of smoothing

Estimating optimal AR model orders on the un-smoothed data showed very high AR model orders mainly in CSF-bearing regions, but also close to the insula and the anterior cingulate cortex (white arrows in Figure 3-10, 1st column), as well as moderate optimal AR model orders in grey matter regions without physiological noise modelling (Figure 3-10, 1st column). Nearly all white matter voxels showed an optimal AR model order of 1. Including RETROICOR regressors successfully reduced the higher AR model orders in CSF and grey matter regions, with a remaining AR model order of 2 to 4 in most grey matter areas (Figure 3-10, 2nd column). Some voxels with AR model order 10 can be found in posterior and anterior regions near tissue-air boundaries (white arrow in Figure 3-10, 2nd column). Adding RRF + CRF regressors had a limited impact on optimal AR model orders (Figure 3-10, 3rd column). The additional movement regressors (RETROICOR + Volterra) reduced optimal AR model orders in a small number of voxels at the posterior and anterior tissue-air boundaries (white arrow in Figure 3-10, 4th column).

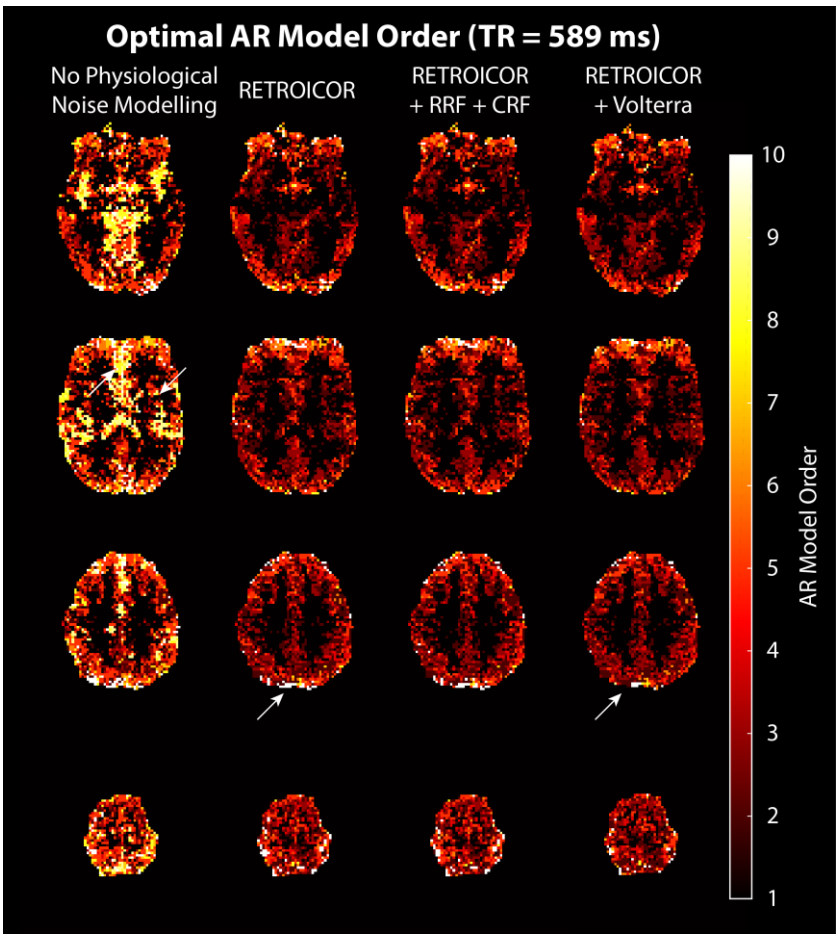

Figure 3-10: Estimated optimal AR model orders for the short-TR sequence without physiological noise modelling (1st column), with RETROICOR regressors (2nd column), with RETROICOR regressors and cardiac and respiration response function modelling (3rd column) and with RETROICOR regressors and Volterra expansion of the realignment parameters (4th column) when no smoothing was applied (subject 1, run 1, TR = 589 ms, 2.5×2.5×2.5 mm3). The white arrows indicate high remaining optimal AR model orders at posterior and anterior tissue-air boundaries with RETROICOR regressors (2nd column), and their slight reduction when including RETROICOR + Volterra regressors (4th column).

3.4 Discussion

3.4.1 Effect of TR and physiological noise on optimal AR model order

The high AR model orders found in the short-TR sequence indicate a complex noise covariance structure that needs to be taken into account when drawing inference on single-subject fMRI data. As expected, physiological noise regressors as provided through the RETROICOR model (Glover et al., 2000) successfully reduced serial correlations in the fMRI time series, resulting in decreased optimal AR model orders. However, optimal AR model orders ranging between two and four were still found even after including physiological noise regressors.

The broad distribution of optimal AR model orders across all grey matter voxels contradicts remaining task related activity as a possible noise source. Also, the low optimal AR model

order found in white matter excludes the possibility of hardware related sources which would affect grey and white matter equally. In the power spectra in Figure 3-6 and the residuum spectra in Figure 3-8 not a single unique frequency could be identified driving the observed effects. Rather, a broad 1/f noise characteristic and large variance around the cardiac peaks were observed. This indicates un-modelled neuronal activity (Bianciardi et al., 2009), given the high intrinsic serial correlation of the hemodynamic response function (Arbabshirani et al., 2014), as well as remaining physiological fluctuations not captured by the linear RETROICOR model as possible sources. Noise sources of even higher frequency seem unlikely other than the known cardiac and respiratory fluctuations and their higher harmonics (Weisskoff et al., 1993).

Accounting for remaining low frequency oscillations through cardiac and respiration response function modelling had a comparatively limited impact, indicating either their localized reach or that more individualized response functions might be required (Falahpour et al., 2013). If specialized equipment is available, more direct measures of end-tidal CO2 through carbon-dioxide data (Wise et al., 2004) and blood flow and oxygenation using near-infrared spectroscopy data (Frederick et al., 2012) could improve the modelling of physiological processes in the low-frequency range. Including the Volterra expansion of the realignment regressors to model remaining movement related signals (Friston et al., 1996) had a small impact mainly limited to voxels at tissue-air boundaries. Importantly, motion regressors characterizing translation and rotation were included in all analysis schemes, and therefore, apparent bulk motion through respiration-induced fluctuations in the main magnetic field is included even in the ‘no phys’ option. Hence, serial correlations introduced through respiration could be slightly underestimated in the results presented here.

Low AR model orders were obtained for the long-TR and the downsampled short-TR sequence in line with previous studies (Lund et al., 2006; Penny et al., 2003). Despite their different spatial resolutions, virtually identical results were obtained from both sequences, indicating that extensive aliasing in sequences with a TR above 2 seconds presumably renders individual noise processes indistinguishable, resulting in low optimal AR model orders. This is in line with the observation of a negligible change in *t*-values with increasing AR model order for data acquired with long TRs and a reduction in *t*-values with increasing AR model order for data acquired with shorter TRs (Sahib et al., 2016).

3.4.2 Implications for error modelling in statistical inference

When using pre-whitening to account for serial correlations, the complex noise structure found in the data acquired with sub-second TR needs to be accommodated in the estimation

of the error covariance V. When choosing the AR model order for spectral estimation, too low AR model orders result in too smooth estimates, whereas too high AR model orders can lead to spurious peaks (Schlindwein and Evans, 1992). Applied to empirical data, using a higher AR model order rather than a too low AR model order has been recommended for spectral estimation (Boardman et al., 2002; Schlindwein and Evans, 1992). Alternatively, the FAST noise model introduced in SPM12 has shown promising results, as indicated in the frequency spectra of the residuals (Figure 3-8, bottom). However, the cardiac and respiratory peak could not be accounted for, and, therefore, additional noise modelling strategies targeting these specific frequencies are required. Either identifying the noise sources and incorporating nuisance regressors for physiological fluctuations or specifying a comprehensive noise model that can capture serial correlations obtained from a broad range of TR values might be the way forward.

As observed previously (Kaneoke et al., 2012), noise characteristics varied across tissue classes and cortical and subcortical regions. Grey matter voxels showed properties of both CSF and white matter, which could be partially introduced through the applied spatial smoothing and partial volume effects. Indeed, the optimal AR model orders obtained for the unsmoothed data show extended white matter areas with optimal AR model order 1, elevated AR model orders in grey matter, and extreme values almost exclusively in CSF-bearing regions. While smoothing might introduce noise in adjacent voxels, it also considerably increases the signal-to-noise ratio (SNR) and functional sensitivity. These results highlight that careful selection of voxels for noise estimation purposes is required, as previously suggested in Purdon et al. (2001) and Woolrich et al. (2001). Pooling across voxels to estimate the stationary temporal covariance V might thus remain feasible when carefully selecting voxels with similar noise properties.

When using the VB framework to infer about regional activation in response to a task, spatial priors express the spatial contingency of evoked responses (Penny et al., 2005) as well as any further prior knowledge. Given the distinct noise properties of different tissue classes found in this work and previous studies (Penny et al., 2003; Woolrich et al., 2001), one might conclude that tissue specific priors could improve noise modelling. However, Penny et al. (2007) showed that Gaussian Markov Random Field priors (Woolrich et al., 2004), which assume the AR coefficient to vary smoothly, supersede tissue specific priors modelling the spatial variability in serial correlations. Given the observed variance in optimal AR model orders (Figure 3-10) and AR coefficient values (Figure 3-7) between different cortical and subcortical regions we anticipate a similar outcome for the data presented here.

3.4.3 Limitations and considerations

When employing SMS acceleration to increase BOLD sensitivity in fMRI time series, two counteracting mechanisms need to be considered. On one hand, the temporal SNR decreases with increasing SMS acceleration factor (Chen et al., 2015). On the other hand, the number of samples per unit time increases, although the effective degrees of freedom do not rise at the same rate due to serial correlations. First investigations show that moderate SMS acceleration factors between two and six strike a balance between the two (Todd et al., 2016). It is clear, however, that the effects of physiological noise needs to be further evaluated when employing SMS acceleration, given its determining role for temporal SNR (Todd et al., 2017; Triantafyllou et al., 2005). Importantly, the spatial variability of different noise processes might render different SMS-factors optimal for different ROIs (Todd et al., 2017).

We have limited our considerations to the single-subject level, keeping in mind the increased interest in using ultra-high field fMRI in single subject studies (Branco et al., 2016; De Martino et al., 2011; Stephan et al., 2017b). However, group studies employing mixed-effect models also rely on the precise estimation of effect sizes and their variance (Chen et al., 2012). Since an unbiased estimator is used for the parameters, random-effects analyses are more robust against deviations in the error covariance estimation.

3.5 Conclusion

Unlike fMRI time series with a longer, more conventional TR of ~ 2 s, SMS EPI data with a short TR of ~ 600 ms exhibit a complex noise structure that cannot be captured by an AR(1) model. While physiological noise modelling successfully reduces serial correlations, an advanced noise model is still required to account for the non-white noise content. Otherwise, single-subject analyses of fMRI data with sub-second TR will result in increased false positive rates, effectively declaring voxels as active without the prescribed significance. Hence, for valid inference on single subject-level with sub-second TR, more advanced pre-whitening schemes in combination with physiological noise modelling are necessary.

3.6 Acknowledgements

We thank Will Penny for valuable comments on the VB algorithm and the estimation and interpretation of the frequency response of the AR models. We thank Aiman Al-Najjar, Nicole Atcheson and Jake Palmer for help with data collection. We thank the reviewers for their time and efforts and Mattias Villani and Lars Kasper for helpful comments on the pre-print. This research was supported by the National Health and Medical Research Council (APP

1088419). MB acknowledges funding from Australian Research Council Future Fellowship grant FT140100865. SB acknowledges support through the Australian Government Research Training Program Scholarship. The authors acknowledge the facilities of the National Imaging Facility (NIF) at the Centre for Advanced Imaging, University of Queensland.

Chapter 4

Interactive and flexible MRI data evaluation: the uniQC toolbox

Keywords

sequence development

quality control

image quality

SPM

MATLAB

time series analysis

Abstract

The challenge of unified and comprehensive quality control (QC) in MRI results from the vast amount of artefact sources combined with the complex processing pipelines applied to the data. Beyond standard image quality measures, MRI sequence development is often in need of flexible diagnostic tools to test diverse hypotheses on artefact origin, such as hardware fluctuations, k-space spikes, or subject movement. These tests are usually performed in a sequential order, where one outcome informs the next evaluation. This necessitates fast switching between mathematical image operations and interactive display of multi-dimensional data to assess image properties from a range of different perspectives. Additionally, for complex image analysis pipelines, as employed, for example, in fMRI, direct access to the standard analysis packages is required to ultimately evaluate functional sensitivity of new sequence prototypes. In this work, we introduce the uniQC toolbox that provides seamless combination of algebraic matrix operations, image processing, visualisation options and data provenance in an intuitive, object-oriented framework using MATLAB, and interfacing SPM for all fMRI-related pre-processsing and statistical analysis steps. Therein, processing of 4D image time series data is generalised to an arbitrary number of dimensions to handle data from, for example, multiple receiver coils, multi-echo or phase fMRI data in a unified framework along with classical statistical analysis and powerful visualisation options. Here, we present the underlying class structure of the uniQC toolbox and typical use cases in fMRI sequence development.

4.1 Introduction

Developing new methods for magnetic resonance imaging (MRI) requires continuous data evaluation via flexible and interactive diagnostic tools. Therein, artefact sources need to be identified, image quality measures estimated, and, ultimately, complex analysis pipelines need to be executed. Additionally, operation on and visualisation of multi-dimensional data is required to accommodate the development of new contrast mechanisms and acquisition techniques. Here we present the uniQC toolbox, which utilizes an object-oriented design to integrate visualisation, image operations and established processing steps as implemented in SPM[5] to provide a flexible and interactive n-dimensional image analysis framework.

In particular when evaluating new acquisition methods for functional MRI (fMRI), advancements at the single image level need to be translated to the image time series, and, ultimately, to the statistical map obtained from an intricate analysis pipeline. Examples of recent developments in MRI acquisition include new radio-frequency (RF) pulses (Breuer et al., 2005; Feinberg et al., 2010; Larkman et al., 2001; Setsompop et al., 2012) and new readout trajectories such as 3D echo-planar imaging (EPI) (Poser et al., 2010) or spirals (Glover, 2012). Additionally, noise correction methods including prospective motion correction (Speck et al., 2006), real-time shim feedback (Duerst et al., 2015) and concurrent magnetic field monitoring (Barmet et al., 2008; Bollmann et al., 2017) have been developed to counteract major noise sources during the image acquisition. New contrast mechanisms such as multi-echo EPI (Poser et al., 2006), functional quantitative susceptibility mapping (Özbay et al., 2016) or cerebral-blood-volume fMRI (Huber et al., 2017) extend the common 4D dimensionality of the image time series, and require handling of multi-dimensional data with several coils, echoes, magnitude/phase or tag/control pairs. Common to all of these approaches is that they affect the image formation at a fundamental level, but the ultimate goal is to increase sensitivity and/or specificity for detecting signal changes indicative of neuronal activity.

The uniQC toolbox was specifically designed to assist during methods development, the translation of these methods to neuroscientific practice (study design/piloting), and the quality control (QC) during data acquisition. Since every experiment is different during sequence evaluation and study design/piloting, a *unique* pipeline is required for QC, often with interactive features. Given the vast amount of artefact sources, such as coil gain fluctuations, k-space spikes, or subject movement, but also errors introduced by the operator, fast switching between image operations and visualisation of multi-dimensional

[5] http://www.fil.ion.ucl.ac.uk/spm/

data becomes necessary to assess image properties from a range of perspectives. Importantly, this assessment is usually performed in a sequential order, where one outcome informs the next evaluation, and, hence, does not follow a prescribed protocol. This flexibility needs to be accompanied by reproducibility, to ensure that the whole of the experiment, i.e. the data acquisition and analysis, is well documented. Thus, uniQC provides a *unified* framework that allows flexibility while preserving reproducibility, to easily adapt the data analysis to changes in the data acquisition. In addition, an established pipeline might be used for QC within a larger study, requiring its *universal* application. The *uni*QC toolbox provides this unified universal approach respecting the uniqueness of QC criteria in MR methods development. As a consequence, *flexibility*, *reproducibility* and *accessibility* are the design principles governing the development of uniQC.

Flexibility is concerned with the handling of various MRI data and the combination of different operations. Essentially, MRI data are images concatenated along multiple dimensions forming n-dimensional data matrices containing diverse information about the object under investigation. Examples include the composition of 3D volumes from 2D slices or 4D image time series from 3D volumes. New developments such as phase fMRI (Bianciardi et al., 2014) or multi-echo EPI (Poser et al., 2006) require representation and analysis of MRI data of arbitrary dimensionality. Data flexibility is provided here as a natural extension from 4D to n-dimensional data matrices giving the researcher the ability to handle and label each individual dimension as desired. Furthermore, operational flexibility is achieved by providing basic image analysis building blocks such as tSNR assessment, image comparisons, contrast enhancement, region-of-interest (ROI) analysis or smoothing. These elementary units can then be combined to perform a complex evaluation tailored to the data at hand. Additionally, visual assessment plays a crucial role when evaluating MRI data. Hence, different options are provided here to fit a variety of needs, which are fully integrated into the same framework as the image analysis.

Reproducibility is pursued by eschewing a graphical user interface, but providing an object-oriented implementation where everything is scriptable in an easy-to-read fashion, and, thereby, documented. Further, through the object-oriented implementation, the interaction between methods and data is well defined. To prevent substantial rewrite of existing code, SPM is tightly integrated into uniQC and provides data nifti[6] file read and write, preprocessing and model estimation functions.

[6] https://nifti.nimh.nih.gov/

Accessibility is enabled by the overloading of common operators and the integration with the html-based MATLAB[7] help browser (`doc`). Thereby, basic image operations can be combined into complex analysis, while the resulting code remains easy to read also for non-expert programmers. Additionally, the object-oriented design provides a well-defined interface for specific contributions to enhance and adapt the functionality.

It is these design criteria that set uniQC apart from other toolboxes, which provide similar underlying functions. For example, after creating an object `I` of the uniQC-class `MrImage` from a multi-echo time series (`I = MrImage('multi_echo.nii')`), realigning this data set using the realignment parameters from the first echo and applying them to the subsequent echoes amounts to `I.realign('representationIndexArray', {'echo', 1}, 'applicationIndexArray', {'echo', 1:3})`. Similarly, a 5D data set of single coil images (`C = MrImage('multi_coil.nii')`) can be easily realigned based on the sum-of-squares combined image using operator overloading via `C.realign('representationIndexArray', sum(C.^2, 'coil'), 'applicationIndexArray', {'coil', 1:8})`. Integrating new functions, or simply utilizing built-in MATLAB image operations is facilitated via `I.perform_unary_operation(@(x) medfilt3(x), '3d')`, which automatically applies the MATLAB 3D median filter at every image for each time point and echo.

In summary, uniQC provides a seamless integration of algebraic matrix operations, image processing, visualisation options and data provenance enabling flexible and interactive MRI data evaluation. In the following Methods chapter, we will first introduce the key classes `MrImage` and `MrSeries` and then provide an overview of the overall class structure. In the Results section, we will highlight selected applications, and present reference demonstrations for the use of all classes.

4.2 Methods

4.2.1 Overview

Central to uniQC is the `MrImage` class, which contains one image consisting of an n-dimensional data matrix and the corresponding image geometry (Figure 4-1, right). Methods of `MrImage` include algebraic matrix operations (`I + 3`), image operations (`I.imclose`) and visualisation (`I.plot`). Thus, `MrImage` represents the fundamental functional unit which encapsulates all basic operations. Based on this, `MrSeries` is a collection of

[7] The MathWorks, Inc., Natick, MA, US

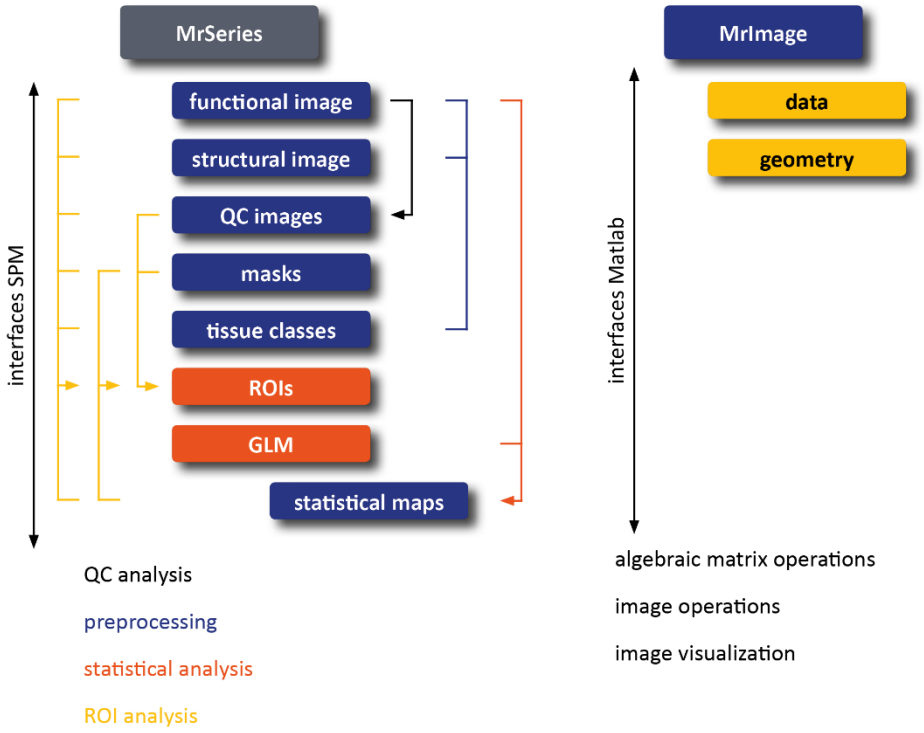

Figure 4-1: Overview of `MrImage` and `MrSeries`. `MrImage` (right) builds the interface with MATLAB and translates built-in algebraic matric operations, image operations and visualisation from data matrices to image objects. `MrSeries` (left) provides a framework for processing of image time series. General functions for QC analysis, ROI analysis, preprocessing and statistical analysis (via SPM) are provided within `MrSeries` and can be arbitrarily combined.

`MrImages` to facilitate a comprehensive time series analysis (Figure 4-1, left). For example, basic QC measures such as mean and tSNR are computed from the functional image (`S.compute_stat_images`), and then evaluated using masks to define specific regions of interest (`S.analyse_rois`). Additionally, the impact of common preprocessing steps performed on functional and/or structural images (`S.realign`) can similarly be included in the evaluation. Ultimately, statistical maps are estimated using the functional image and the information contained in the general linear model (GLM) (`S.specify_and_estimate_1st_level`). Throughout, the modularization of methods in `MrImage` allows direct access to principal operations in fMRI methods and data evaluation and their flexible combination into complex analysis pipelines.

To allow for fast prototyping of image analysis pipelines, it is beneficial to keep data and operations close together, to swiftly switch between different tasks. Combining both image data and operations in one container is the natural outset to an object-oriented approach. MATLAB's equivalent bracket and dot-notation for object methods then allows for very compact representations of QC tasks. For example, visualising the SNR benefit of realignment of a 4D image time series `I` could be expressed as `plot(abs(I.snr-`

`I.realign.snr)`, with `abs`, `snr` and `realign` all being methods of the image that return a modified image, and plot acting as a non-modifying visualization method. Furthermore, MATLAB's operator overloading (here -/minus) makes for an intuitive syntax for most algebraic image operations. The next sections will introduce each class in more detail and also outline specifics concerning their implementation.

4.2.2 MrImage

`MrImage` contains data and meta-data of one n-dimensional image. Figure 4-2 shows an overview of its properties and methods (also available via `doc MrImage` or `methods(MrImage)`). Properties include the n-dimensional data array, the object name (for plotting and referencing within `MrSeries`, e.g. `'with new method'`), an info array which is automatically populated when calling methods (`operator(nameImage1, nameImage2)`), and parameters to control saving and plot options. Handling of the image geometry is facilitated through a number of complex properties, which are objects themselves. The `dimInfo` contains the dimensionality information in the voxel space defined by the data, i.e. it describes the properties of the n-dimensional data matrix. To place this data matrix into world space, the `affineGeometry` contains the affine transformation matrix using the nifti convention. `MrImageGeometry` is a dependent object that combines the information from both `dimInfo` and `affineGeometry` to provide geometry information most commonly used in fMRI analyses: field-of-view (FOV), number of voxels, resolution, repetition time (TR), offcenter, rotation, shear. The results of ROI analysis are stored in rois containing a cell of `MrRoi` objects.

A `MrImage` object can, in the simplest case, be constructed from a data matrix (`I = MrImage(data_matrix)`). The `dimInfo` and `affineGeometry` will incorporate the dimensionality information obtained from data (`nSamples` and `nDims`) and otherwise resort to default values. Specific dimensionality information can be incorporated during construction as well, allowing to specify the sampling of the data: `I = MrImage(data_matrix, 'dimLabels', {'x', 'y', 'z', 't', 'echo', 'coil'}, 'units', {'mm', 'mm', 'mm', 's', 'ms', 'samples'}, 'resolutions', [1.5 1.5 2 0.65 32 1])`. Read-in functions for nifti, Philips par/rec and mat-files are provided as well.

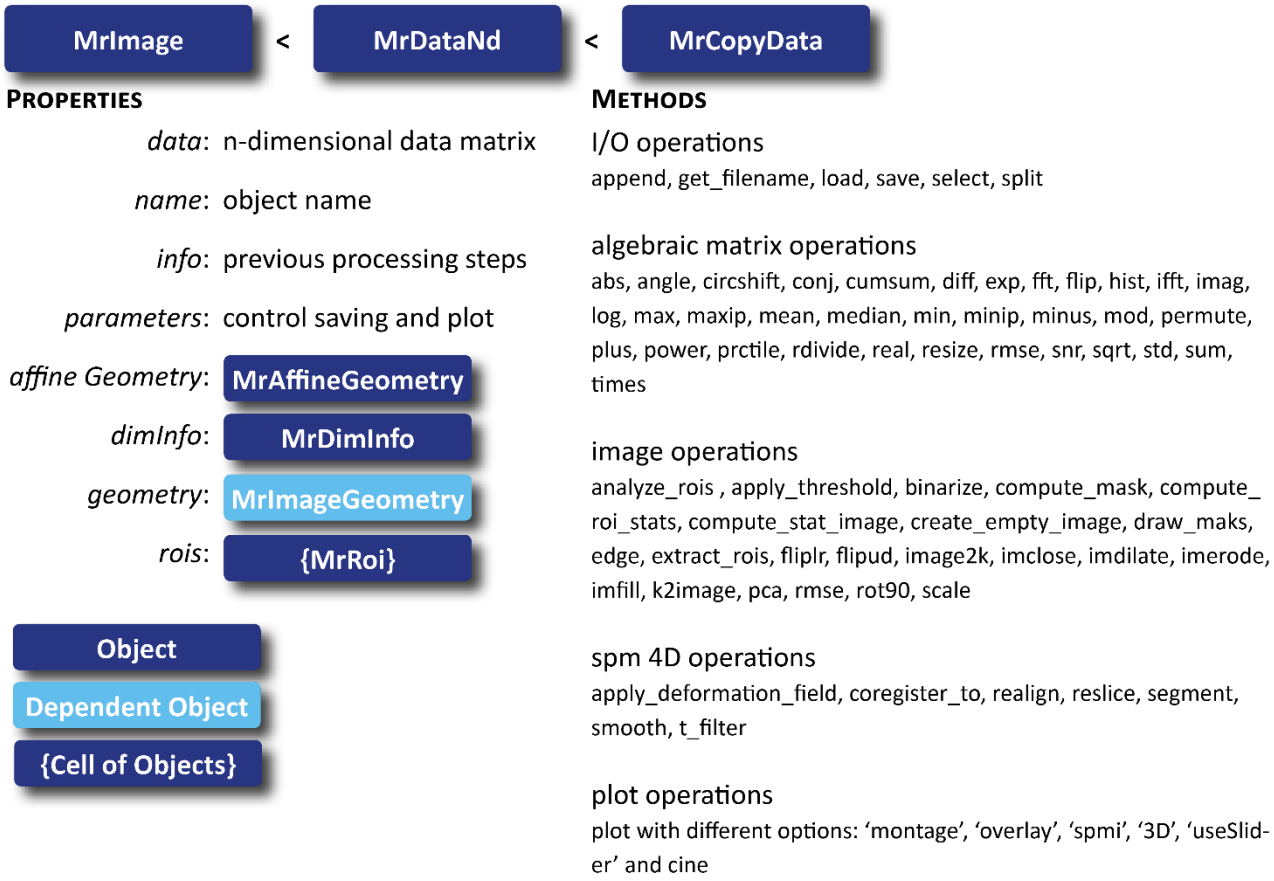

Figure 4-2: Properties and methods of the `MrImage` class. A complete overview can be obtained via `methods(MrImage)`. The algebraic matrix operations create an intuitive syntax, e.g. `(I1 .* I2) + I3`. The image operations generalize 2D image operations to nD images. The spm 4D operations encapsulate preprocessing steps within SPM. The plot properties are controlled via property/value pairs and offer a range of visualisation options.

Methods of `MrImage` can be divided into 5 categories: input/output operations, algebraic matrix operations, image operations, SPM 4D operations and plot operations (Figure 4-2, right). Operator overloading[8] is employed to allow the intuitive concatenation of processing options. For example, object and non-object variables can be easily combined using common mathematical symbols (`I_plus_3 = I + 3`). In combination with the defined `dimLabels`, subsets of data can be intuitively accessed, and combined with processing and plot operations in one step (`plot(I1.abs - I2.abs), 'z', 15, 'coil', 1:3`). Thereby, the visual inspections becomes part of the processing pipeline and is inherently documented and reproducible.

[8] https://au.mathworks.com/help/matlab/matlab_oop/implementing-operators-for-your-class.html

4.2.3 MrSeries

The `MrSeries` class is a collection of `MrImage` objects to perform evaluation of (f)MRI data (Figure 4-3). The methods of `MrSeries`, governed by the parameters stored in the parameters field, directly operate on these images and populate them accordingly. Further, `MrSeries` automatically creates a folder structure that, in conjunction with the `processingLog`, documents the performed analysis (Figure 4-3, right). This allows to restore a previous processing step (`MrSeries.restore('realign')`), and provides an interface to other software compatible to the nifti format.

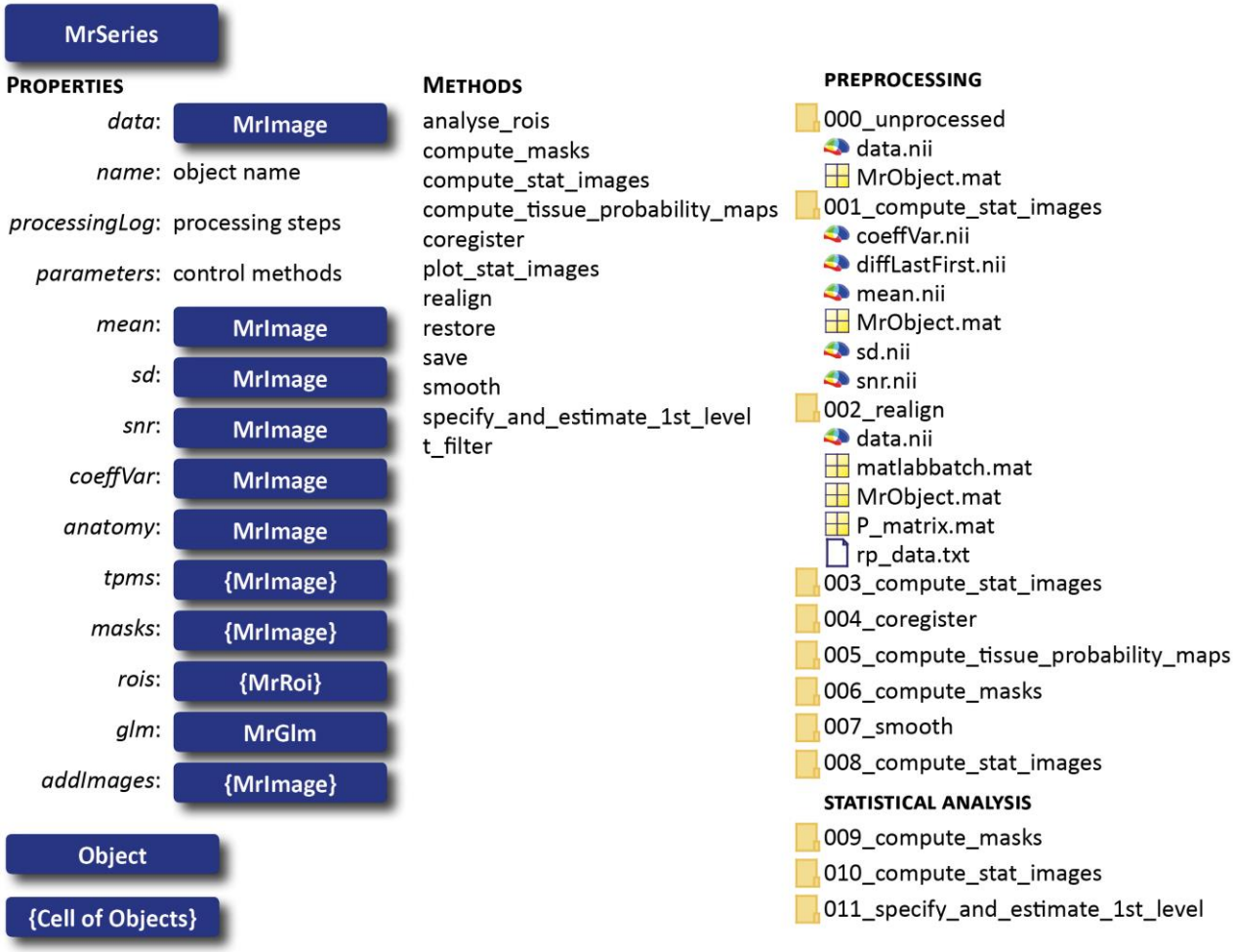

Figure 4-3: Properties and methods of the `MrSeries` class. The folder structure (right) is the result of `demo_preprocessing` and `demo_model_estimation_1st_level`.

4.2.4 Class structure

The following chapter provides an overview of all classes defined within the uniQC toolbox: `MrImage`, `MrSeries`, `MrDimInfo`, `MrDataNd`, `MrAffineGeometry`, `MrImageGeometry`, `MrGlm`, `MrRoi`, `MrCopyData`, `MrImageSpm4D`, and `MrUnitTest`. Table 4-1 summarizes the class name, the purpose, exemplary operations and the parent

class	purpose	operations	parent

MrImage	Contains and analyses one nD image	`I.compute_masks;`
		`I.imfill;`
		`I.plot;`
			MrDataNd

MrSeries	Contains and analyses a selection of MrImages	`S.compute_stat_images;`
		`S.coregister;`
		`S.specify_and_estimate_1st_level`
			MrCopyData

MrDimInfo	Contains dimensionality information	`DI.select;`
		`DI.split;`
		`DI.permute;`
			MrCopyData

MrDataNd	Contains nD data arrays	`D1 + D2;`
		`D.select;`
		`D.abs;`
			MrCopyData

MrAffineGeometry	Contains affine geometry	`AG.apply_transformation;`	MrCopyData
MrImageGeometry	Contains common parameters for time series data	`disp(IG)`	MrCopyData; dependent property of MrImage
MrGlm	Contains experiment information	`G.init_glm;`	MrCopyData
MrRoi	Contains data and summary statistics of ROIs	`R.compute_stats;` `R.plot;`	MrCopyData
MrCopyData	Deep recursive copy and object comparisons	`CD.copyobj;` `CD.comp;`	handle
MrImageSpm4D	Wrapper for SPM functions	`I4D.realign;` `I4D.segment;`	MrImage
MrUnitTest	Unit test	`run(UT);`	unittest.TestCase

Table 4-1: Overview of all uniQC classes indicating their name, purpose, exemplary operations and parent class.

class. After MrImage and MrSeries have been introduced above, MrDimInfo, MrDataNd, MrAffineGeometry, MrImageGeometry, MrGlm, MrRoi and MrCopyData will be described in more detail here. Information about MrImageSpm4D can be found in the chapter *Integration with SPM* and MrUnitTest is described in *Unit testing*.

MrDimInfo contains all dimensionality information describing an n-dimensional data matrix. Figure 4-4 illustrates properties of MrDimInfo, dependent properties, and their geometric interpretation in an n-dimensional data set. MrDimInfo provides the means to handle and label data matrices with arbitrary dimensions. The center location and extent of each sample are given by samplingPoints and samplingWidths, respectively. Descriptions of each dimension are contained in dimLabels and units (defaults are 'x', 'y', 'z', 't', 'coil', 'echo' for dimLabels and 'mm', 'mm', 'mm', 's', 'nil', 'ms' for units). Resolutions are derived from samplingPoints and contain the (equidistant) spacing between them. Ranges give the first and last sampling point. The number of dimensions and the number of samples in each dimension are contained in nDims and nSamples, respectively. The samplingWidths can be used, for example, to express the slice gap, i.e., difference between slice thickness and slice distance (resolutions), or to convert ranges into FOV (+ samplingWidths, see Figure 4-4).

Properties of MrDimInfo and their dependencies are summarized in Figure 4-4 (left). The construction of an MrDimInfo object from different input data is illustrated on the right hand side. In the first case, samplingPoints are explicitly given alongside dimLabels and units. If no dimLabels or units are given, default values are assumed, since no empty dimLabels or units are allowed. If not given explicitly, samplingWidths are initialized to the same values as resolutions (assuming, e.g., no slice gap). Later on, when resolutions are changed in an existing MrDimInfo object, samplingWidths remain unaltered (except if set explicitly). Thus, when selecting a subset of samples, samplingWidths can provide information on the extent of a sample even when the sampling points are non-equidistant and, hence, a resolution is no longer defined. Information about the sampling points can also be provided using a combination of other (dependent) properties, as illustrated in Figure 4-5 in the subsequent rows. When nSamples and ranges are given as an input, equidistant spacing is assumed to create the samplingPoint array. Similarly, nSamples and resolutions, in conjunction with one sampling point and its array index, can be used to create all sampling points. When creating

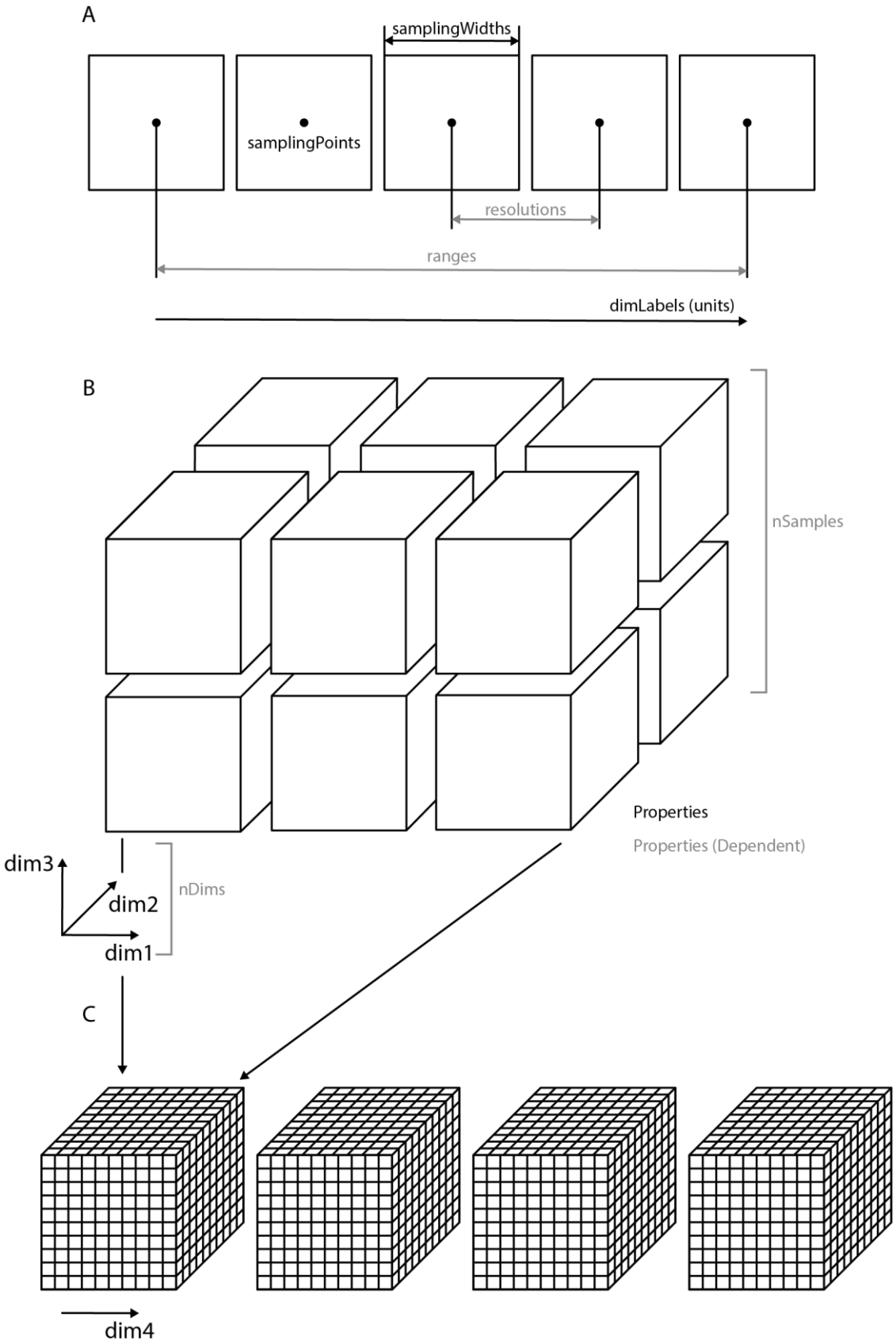

Figure 4-4: Properties defining `MrDimInfo` include `samplingPoints`, `samplingWidths`, `dimLabels` and `units`. The dependent properties `resolutions`, `ranges`, `nSamples` and `nDims` are derived from sampling points.

an `MrDimInfo` object from a nifti or Philips par/rec file, `nSamples`, `resolutions` and the first sampling points are extracted from the header.

Note that `MrDimInfo` describes the n-dimensional data array through an orthogonal coordinate system originating at the first sample. This allows the comprehensive description of other kinds of data besides images, e.g., raw coil (k-space) data or k-space trajectories, and incorporates higher dimensions, e.g., time, coils, echo time and contrast, within the same framework that describes image data. When forming an image, `MrAffineGeometry` provides the transformation to the nifti neuroimaging coordinate system.

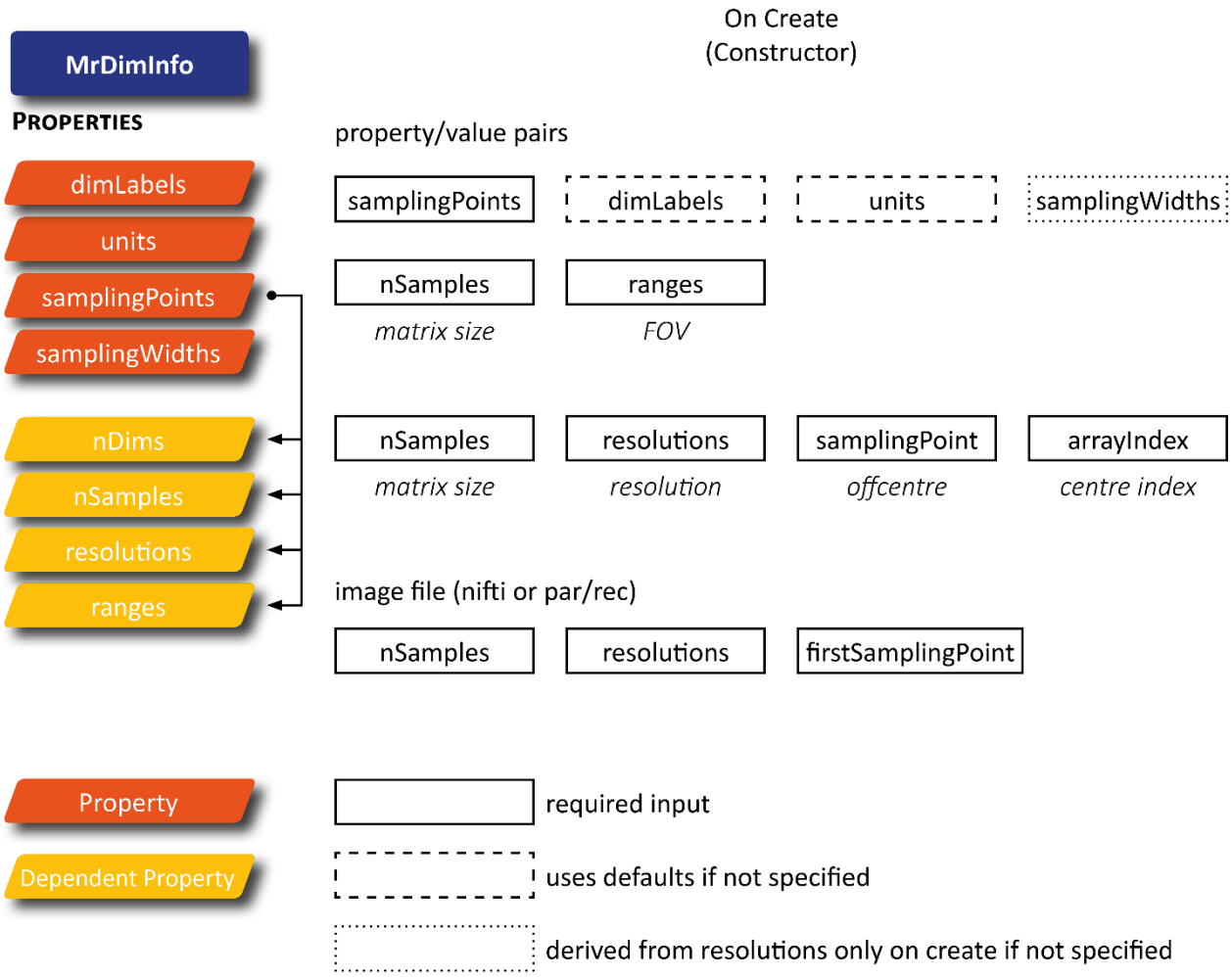

Figure 4-5: Constructor of `MrDimInfo` using different property/value pairs. `MrDimInfo` can be constructed from properties (orange) as well as a combination of dependent properties (yellow).

A key feature to easily access, display and manipulate subsets of data is the direct dot-notation of user-defined properties, e.g., by referring to `dimInfoObject.MyDimLabel.resolutions`, which is enabled by overloading MATLAB's subsref and subsasgn functions. An example output is given below (case 1b in `demo_dim_info.m`):

```
MrDimInfo with properties:
                    nDims: 5
                nSamples: [64 50 33 100 8]
            resolutions: [3 3 3 2.5000 1]
                 ranges: [2×5 double]
              dimLabels: {'x' 'y' 'z' 't' 'coil'}
                  units: {'mm'  'mm'  'mm'  's'  'nil'}
         samplingPoints: {1×5 cell}
         samplingWidths: {[3]  [3]  [3]  [2.5000]  [1]}
```

`MrDataNd` contains the n-dimensional data described in `MrDimInfo` and provides general algebraic matrix operations (note that it does not rely on the implicit expansion of arrays as introduced in MATLAB R2016b). Properties include the data matrix, the object name, and info field, parameters and a `MrDimInfo` object (cf. Figure 4-2). Note that `MrDataNd` has no `affineGeometry` and can be used as a general storage for non-image data.

`MrAffineGeometry` stores the affine transformation of an image in nifti convention. It uses `spm_matrix` to translate an affine transformation matrix into `offcentre` (translation), `rotation`, `shear`, and `resolution` (scaling). Note that the affine geometry is in general disregarded during plot and images are presented in voxel space. The display options in SPM (`MrImage.plot('plotType', 'spmi')`) allow the visualisation when applying the affine geometry.

`MrImageGeometry` offers convenient access to geometry information for 4D data sets, i.e. for fMRI time series analysis. It contains the 'classical' geometric information to describe a 4D data set, i.e. `FOV_mm [1x3]`, `nVoxels [1x4]`, `resolution_mm [1x3]`, `TR_s [1x1]`, `offcentre_mm [1x3]`, `rotation_deg [1x3]`, `shear [1x3]`, `sliceOrientation [1x1]`, and `coordinateSystem` (`scanner` or `nifti`). `MrImageGeometry` is constructed from `MrAffineGeometry` and `MrDimInfo`. As the geometry of an `MrImage` object, it is a dependent property and does not have a set – method, only a constructor. It is always created on the fly from `MrDimInfo` and `MrAffineGeometry` to ensure clear update rules. The `displayOffset` from `MrAffineGeometry` is used to specify the `offcenter_mm`

according to the coordinate system (i.e. `nifti` is first voxel, `scanner` is centre of imaging volume).

`MrGlm` is used to specify the first-level (single-subject) GLM and to provide an interface to the SPM design specification and estimation. An overview of its properties, a description of these and an example are given in Table 4-2.

`MrRoi` contains the results of ROI analysis. `MrRoi` is interfaced best using methods of `MrImage` to extract the data in a slice-by-slice fashion (`I.extract_rois(mask)`). Then, descriptive statistics such as mean, snr, min and max can be computed per slice and over the whole (ROI) volume (`I.compute_roi_stats()`). Results can directly be visualised as time series values or histograms (`I.rois{1}.plot`).

`MrCopyData is a` super class that provides a clone-method for all object classes, (i.e., a deep recursive copy, in contrast to the default reference copy behaviour for handle objects in MATLAB) and recursive find and comparison utilities. Thereby, independent copies of objects can be created allowing different processing streams from the same source image, such as creating a mask from a mean image. All uniQC classes are derived from `MrCopyData`.

4.2.5 File management

The file management within `MrSeries` is illustrated in Figure 4-3. The results of each processing step are saved in a consecutively numbered folder starting with the automatically created unprocessed data. The overall save path is stored in `S.parameters.save.path` and populated on create with `pwd/MrSeries_date_time`, which can then be adapted by the user. During save, the data and the `MrSeries` object are separated, allowing easy access to the data and straightforward interfacing with other tools. The data created in each step are saved as nifti images or text files (e.g. for the realignment parameters) and the `MrSeries` object is saved as a .mat file, but stripped of the data. To restore a previous analysis, the `MrSeries` constructor can be called with the used save path (`S = MrSeries(path)`). Within `MrSeries`, one can also revert to previous instances of the `MrSeries` object by calling the restore function (`S.restore(iProcessingStep)`). Similarly, `MrImage` allows to define a path and a filename (including the file extension) which are used during saving. Note that the object name is used for referencing within the application of different processing steps and the filename is used when saving the data. While `MrSeries` automatically saves the data after each processing steps, `MrImage` requires the user to manually save the data (`I.save`).

property	description	example
regressors	confound regressors included in the model estimation (e.g. realignment parameters)	[nxm] matrix with n being the number of volumes

conditions	cells of names, onsets and durations describing the stimulus timing	`names = {'stimulus'}`
		`onsets = {[10 20 30]}`
		`durations = {[5]})`

timingUnits	units in which the TR is specified	`'secs'` or `'scans'`
repetitionTime	timing of the image acquisition (in timingUnits)	`2.5`
hrfDerivatives	derivatives of the hemodynamic response	`[0 0]` - canonical only `[1 0]` - temporal derivative `[0 1]` - dispersion derivative `[1 1]` - both
maskingThreshold	intensity threshold [0 1] applied to the mean image to exclude voxels below the given proportion of the global intensity	`0.8` `-Inf` includes all voxels
explicitMasking	explicit mask image for parameter estimation	`'masks/brain_mask.nii'`
estimationMethod	parameter estimation method	`'classical'` or `'Bayesian'`
serialCorrelations	serial correlations model used for pre-whitening (classical only)	`'AR(1)'` or `'FAST'`
ARModelOrderBayes	AR model order for pre-whitening (Bayes only)	`3`
gcon	contrast vector for contrast estimation (Bayes only)	`[1 0]` `[1 -1]`
designMatrix	design matrix scaled for display	`loads SPM.xX.nKX`
parameters	contains file path and the SPM directory	

Table 4-2: Overview of `MrGlm` properties which are derived from the SPM estimate batch.

4.2.6 Integration with SPM

SPM operations are integrated via the intermediate class `MrImageSpm4D`. `MrImageSpm4D` contains one real-valued, 3 or 4-dimensional image, which forms the input into the SPM functions `compute_tissue_probability_maps`, `coregister`, `realign`, `smooth`, and `t_filter`. When extending these operations to n-dimensional images, a number of possible scenarios occur, which are best illustrated on the example of `realign`:

1) complex image time series (complex 4D) – estimate realignment parameters on magnitude image and apply to magnitude and phase image
2) multi-echo image time series (real 5D) – estimate realignment parameters on first echo and apply to all echoes
3) multi-coil image time series (real 5D) – estimate realignment parameters on the combined image and apply to individual coil images
4) multi-contrast image time series (real 5D) – estimate and apply realignment parameters for each contrast individually

Thus, one has to specify the application dimension and the representation dimension on which the parameters are estimated. In the first example, the representation dimension is the magnitude image and the application dimensions are the magnitude and phase images, respectively. Similarly for the multi-echo and multi-coil images. Here, the representation dimension are the first echo or the coil-combined image and the application dimensions are the individual echoes or coil images. The last example estimates and applies the realignment parameters independently for each image. Other SPM operations can be seen as special cases of these scenarios. For example, `smooth` has no representation dimension, but the data need to be split into 4D images for SPM. Hence, it's beneficial to select the split dimensions as the dimensions with the smallest number of sampling points. Note that the first 3 dimensions are seen as the image forming dimensions, typically x, y, and z. In the case of `t_filter`, the representation and application dimensions are typically a one-to-one matching. In contrast, the transformation parameters and flow fields estimated via `coregister` and `compute_tissue_probability_maps` need to be applied to all dimensions. In summary, when extending SPM functions to the n-dimensional case, one has to specify which data forms the representation dimension and how the estimated parameters are then transferred to the application dimension.

4.2.7 Unit testing

Unit testing is implemented in `MrUnitTest` using the object-oriented framework provided within MATLAB (`testsuite` introduced in R2016a). Class constructors are tested using either reference parameters (e.g. `MrDimInfo` via `MrUnitTest.make_dimInfo_reference`) or test data sets. The whole test suite (`test/unit_test_main`) can be run via `TestSuite` or individual test can be selected using tags (class names or `'Constructor'`) or test case names. Currently, `MrUnitTest` contains test methods for the constructor and methods of `MrDimInfo`, `MrAffineGeometry`, `MrImageGeometry` and `MrDataNd`.

4.2.8 Coding conventions

The coding conventions employed in uniQC follow the MATLAB Style Guidelines 2.0 by Richard Johnson. A short summary and designated conventions for uniQC are available in custom_coding_conventions.pdf in the guidelines folder. The most notable deviation from the coding conventions was designed to enhance the readability: methods are named using underscores, e.g. `compute_tissue_probability_maps` instead of `computetissueprobabilitymaps`. All properties, however, remain mixed case. Auxiliary classes, i.e. classes that are used as a property of another class, start with the whole class name, e.g. `MrImage` and `MrImageGeometry`. To easily identify classes belonging to uniQC, all classes start with `Mr`. In the directory `utils`, functions for creating new classes, methods and enumeration are provided. To utilise the native documentation options in MATLAB, one-line descriptions are added to class definitions, properties and methods, which are then displayed when calling `doc MrClass`. Furthermore, all conventions are compatible with the hyperlinked documentation displayed in the MATLAB help browser. Throughout uniQC, (`'propertyName', propertyValue`) pairs are used instead of sequential input to accommodate the large number of possible inputs for the most versatile methods (e.g. `plot`) and the user-defined naming of dimensions.

4.2.9 Example data

A number of example data sets are included in the uniQC toolbox and stored in `data/nifti` and `data/parrec`. In particular, examples include a 3D nifti image, a short 4D time series, a long 4D single-echo time series for model estimation, a 5D multi-echo time series, a 5D deformation field, a folder filled with 3D nifti images forming a 5D image, and a 4D Philips par/rec file. These files are used in the examples below and in the demo scripts.

4.3 Results

4.3.1 Example Use Cases

In the following section, a number of example use cases will be discussed in detail, illustrating the usage and interplay of the different classes introduced above. All example scripts can be found in the folder `demo/[MrClassName]`. Additionally, a short overview for all demos within the uniQC toolbox is provided below. The demos provide detailed instructions for specific key methods of each class, comments on optimal usage and implementation specifics. They are best run either step-by-step in debug mode or by executing one code section at a time, and are meant to serve as a point of reference together with the documentation (doc `MrClass.method`).

4.3.2 Visualisation tools

First, the different visualisation tools provided within uniQC will be introduced, which play a key role in the data evaluation. A comprehensive overview is provided in `MrImage/demo_plot_images`, which also produced the output presented in Figure 4-6. Using plot with default settings will show the first 3D volume in a montage plot[9], i.e. the first two dimensions are shown as slices and the third as tiles (Figure 4-6A). Any subset of the data can be selected using the defined `dimLabels` (`I.plot('t', 1:15, 'echo', 2, 'coil', [3,6,7])`). Note that all samples of any non-selected dimension will be plotted and additional figures will be created to accommodate images with more than 3 dimensions.

Visualising data in this way allows the implicit documentation of the performed assessment, i.e. the specific dimension and array index are explicitly documented, and no manual interaction is required to re-create the same plot. Overlay images (`I.plot('overlayImages', I.edge)`) can be added to the plot which allows, for example, the assessment of segmentation and ROI definitions (Figure 4-6B). The `overlayImages` can be a cell array of an arbitrary number of `MrImage` objects including masks, edges and maps. The `useSlider` option allows to interactively scroll through a 4D image or play a video across dimensions (Figure 4-6C). To explore a 3D volume, the `3d` option provides 3 orthogonal images and a 3D view[10]. Note that the images are displayed in matrix space and any 3D image can be selected, for example slice along time or across

[9] Plotting only the first 3D volume was chosen as a default option to prevent the un-intentional output of, for example, a whole time series with potentially several hundreds of volumes.

[10] Adapted from vis3d.m by Joshua Stough (April 2013) from the MATLAB file exchange (http://ch.mathworks.com/matlabcentral/fileexchange/37268-3d-volume-visualization/content/vis3d.m)

coils. Access to the common SPM visualisation options (`I.plot('plotType', 'spmi')`) is provided as well, and, depending on the input data, display or check registration is chosen automatically.

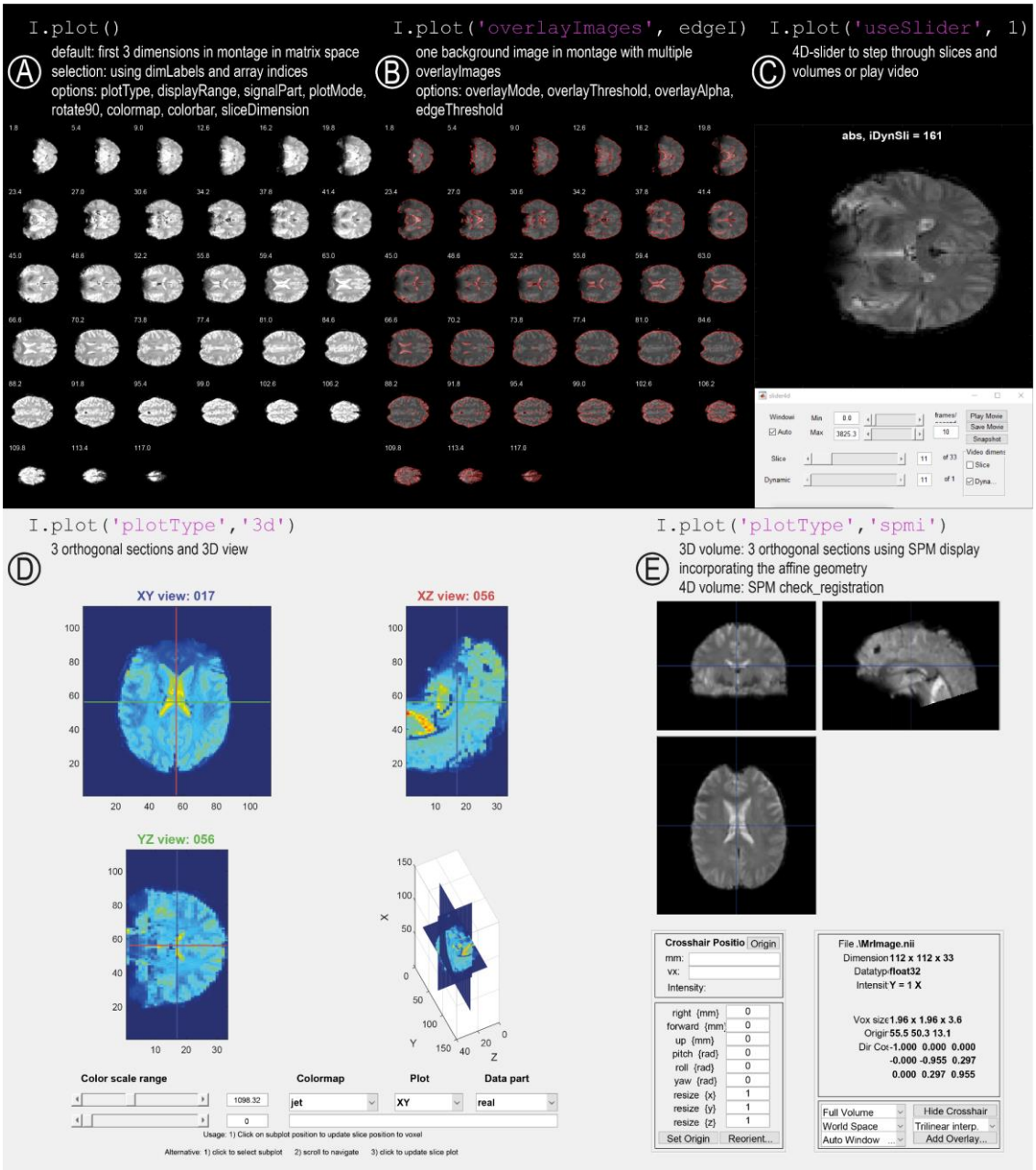

Figure 4-6: Plot operations for MrImage using 2D slices and tiles (A-C) and 3D volumes (D,E).

4.3.3 Image operations

An overview of all image and algebraic matrix operations is presented in Figure 4-2, and examples are provided in `MrImage/demo_image_math_imcalc_fslmaths`. The method calls are chosen such that they provide a natural extension of the MATLAB syntax, i.e. `abs(I)` internally computes `abs(I.data)`. Further, arithmetic operators are overloaded allowing `I + 3` and `I1./I2`. However, the image object always needs to be

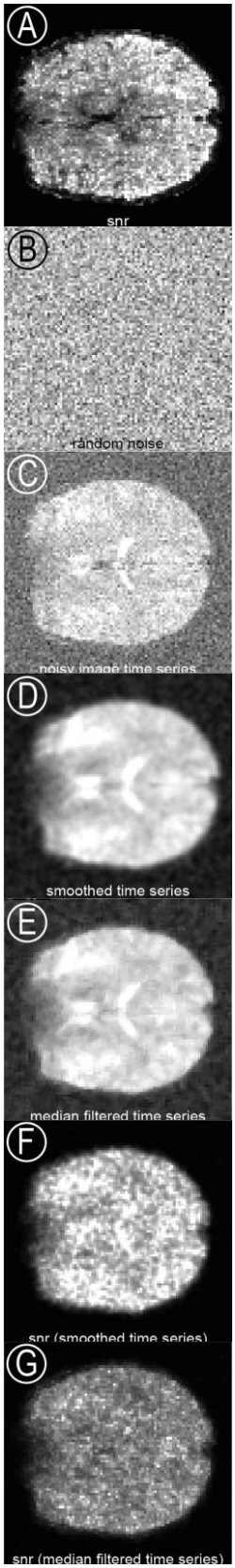


```
% load data
I = MrImage(fileTest);
% compute tSNR and plot
snrI = I.snr();
snrI.plot;

% add Gaussian noise to the image time series
% make noise image with same dimensions as I
noise = MrImage(randn(I.geometry.nVoxels));
noise.name = 'random noise';
noise.plot;

% add just a bit noise, though
noiseI = I.scale + noise .* 0.05;
noiseI.name = 'noisy image time series';
noiseI.plot;


% remove noise via smoothing
noiseISmoothed = noiseI.smooth(2); % FWHM = 2
noiseISmoothed.name = 'smoothed time series';
noiseISmoothed.plot;


% filter using matlab 3D median filter
IMedianFilter = NoiseI.perform_unary_operation(...
@(x) medfilt3(x), '3d');
IMedianFilter.name = 'median filtered image';
IMedianFilter.plot;

% compute tSNR and plot
noiseISmoothedSnr = noiseISmoothed.snr;
noiseISmoothedSnr.plot('displayRange', [0 35]);



% compute tSNR and plot
IMedianFilterSnr = IMedianFilter.snr;
IMedianFilterSnr.plot('displayRange', [0 35]);
```

Figure 4-7: Illustration and code for algebraic matrix and image operations using `MrImage`. First, the tSNR of the raw time series is estimated (A). Next, a random noise image is generated (B) and added to an image time series (C). The introduced noise is then removed using the Gaussian smoothing kernel in SPM (D) or a median filter supplied in MATLAB (E). Last, the resulting tSNR of the two processing options is compared (F and G).

the first item, i.e. `3 + I` will produce an error. Operations frequently encountered in time series analysis are integrated as well, such as `I.snr`, which computes the temporal SNR. Image operations including `I.imclose` and `I.imfill`, which have a native MATLAB 2D implementation, are automatically applied repeatedly to generalize to higher order dimensions. Key methods in the implementation of these operations are `perform_unary_operation` and `perform_binary_operation`. These methods have a function handle and the application dimension as input, and generalize the application of arbitrary operations on the `MrImage` object, including the update of the `dimInfo` and the `info` field. Figure 4-7 illustrates the combination of algebraic matrix operations, image operations and visualisation by adding random noise to an image time series and applying different filters to remove it. Note how the MATLAB-internal image operation `medfilt3` can easily be integrated and is then automatically applied for each 3D image along the time series (Figure 4-7E). Further, the resulting tSNR maps a directly scaled when calling the plot method (`'displayRange', [0 35]`) (Figure 4-7FG).

4.3.4 Quality control pipeline for fMRI data

The quality control pipeline presented below will introduce `MrSeries` and illustrate how it encapsulates operations commonly performed during quality control and analysis of fMRI data (the complete script is provided in `demo_fmri_qa`). As illustrated in Figure 4-1 and Figure 4-3, `MrSeries` contains a number of `MrImage` objects, which are automatically populated during the relevant method call. Examples include the computation and visualisation of key statistical images such `mean`, `std`, `tSNR`, `coeffVar` and `diffLastFirst` (Figure 4-8A). Preprocessing steps are integrated in a similar manner, such that `S.realign` will update the data and the regressors in the glm (Figure 4-8B). After computing statistical images form the realigned data, different `sliceDimensions` can be chosen to visualize the images in different planes (Figure 4-8C). The slider allows the interactive exploration of the whole data set (Figure 4-8D). To perform a ROI analysis, a mask image needs to be created (Figure 4-8E), followed by the extraction of data and tSNR values (Figure 4-8F). Finally, a principal component analysis (PCA) is performed to identify possible artefactual fluctuations (Figure 4-8G).

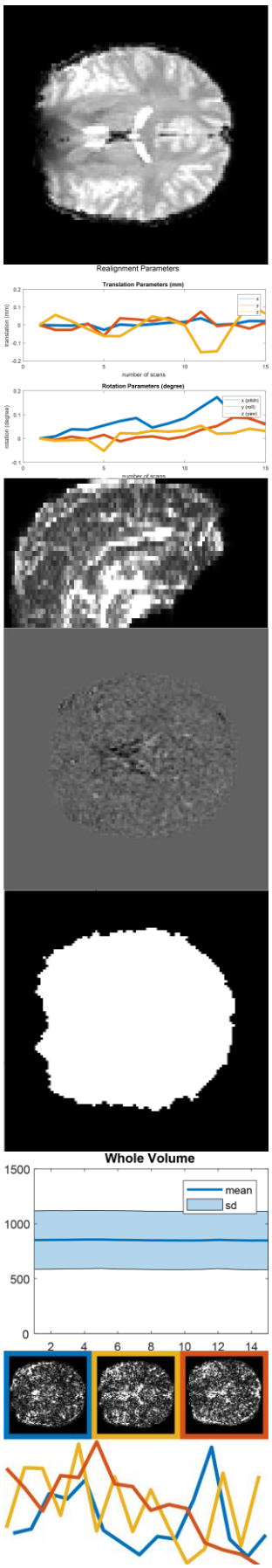


```
(A) % load data
S = MrSeries(fileRaw)
% compute times series statistics
S.compute_stat_images;
S.mean.plot;

(B) % realign image time series
S.realign;
% check realignment parameters
S.glm.plot_regressors;

(C) % check sd images sagittal views
S.sd.plot('sliceDimension', 1, 'x', 48:69, 'rotate90',2)

(D) % any image fluctuations or drifts?
diffMean = S.data - S.mean;
diffMean.plot('useSlider', true);

(E) % compute mask from mean for ROI analysis
S.parameters.compute_masks.nameInputImages = 'mean';
S.parameters.compute_masks.nameTargetGeometry = 'mean';
S.parameters.compute_masks.threshold =
S.mean.prctile(75);
S.compute_masks();

(F) % perform ROI analysis
S.parameters.analyze_rois.nameInputImages = {'data',
'snr'};
S.parameters.analyze_rois.nameInputMasks = '.*mask';
S.analyze_rois();
(G) % perform spatial PCA
PC4D = S.data.pca(3);
```

Figure 4-8: Illustration of `MrSeries` for quality control using statistical images (A, C), realignment parameters (B), difference images (D), ROI analyses (E, F) and a principal component analysis (G).

4.3.5 Extension to n-dimensional data sets

Based on the scenarios identified in the section *Integration with SPM*, the following syntax was developed to specify the representation and application dimensions (Table 4-3). More details can be found in `demo_multi_echo_realign` and `demo_split_complex`.

Scenario	Syntax
0) real 4D `dimLabels = 'x' 'y' 'z' 't'`	`I.realign` – this is the standard case which is also natively available in SPM
1) complex 4D `dimLabels = 'x' 'y' 'z' 't'`	`I.realign` – data are automatically split and estimation is performed on the magnitude images and the realignment parameters are then applied to the phase images
2) multi-echo 5D `dimLabels = 'x' 'y' 'z' 't' 'echo'`	`I.realign('applicationIndexArray', {'echo', 1:3})` – the representation index is automatically chosen as the first index of all extra (non-4D) dimensions and the realignment parameters are then applied to all echoes
3) multi-coil 5D `dimLabels = 'x' 'y' 'z' 't' 'coil'`	`I.realign('representationIndexArray', sum(I.^2, 'coil'), 'applicationIndexArray', {'coil', 1:8})` – the representation index is now the sum-of-squares combined image and the realignment parameters are then applied to all single-coil images
4) multi-contrast 5D `dimLables = 'x' 'y' 'z' 't' 'c'`	`I.realign('representationIndexArray', {'c', 1:5}, 'applicationIndexArray', {'c', 1:5})` – the representation index are the individual contrast images, and the realignment parameters are applied in a one-to-one mapping

Table 4-3: Overview of Scenarios of different realignment schemes including real 4D (0), complex 4D (1), and different configurations of real 5D data (2-4).

4.3.6 Demos overview

`MrImage/demo_add_overlay.m`: Illustrates how to use plot with `overlayImages` and compares it to an implementation using native MATLAB code.

`MrImage/demo_constructor.m`: Illustrates how `MrImage` objects can be created from nifti files, folders and Philips par/rec files.

`MrImage/demo_coregister.m`: Illustrates how to coregister a structural to a functional image and the difference between changing (only) the geometry and reslicing the coregistered image.

`MrImage/demo_image_math_imcalc_fslmaths.m`: Illustrates how to estimate image properties and compare different images.

`MrImage/demo_multi_echo_realign.m`: Illustrates the syntax to extend SPM preprocessing options to n-dimensional data.

`MrImage/demo_plot_images.m`: Illustrates the versatile plot options; see also section *Visualisation tools*.

`MrImage/demo_roi_analysis.m`: Template for a fast analysis of regions-of-interest defined using tissue masks and manually drawn masks, which can be saved and, thereby, enhance the documentation of the performed analysis.

`MrImage/demo_spikes.m`: Illustrates the performance of different visualisation options such as mean and tSNR images and dynamic displays to identify k-space spikes.

`MrImage/demo_split_complex.m`: Illustrates how complex data are automatically split and combined to perform SPM preprocessing operations.

`MrSeries/demo_fmri_qa.m`: Illustrates how to combine different visualisations and image operations to inspect an fMRI time series.

`MrSeries/demo_model_estimation_1st_level.m`: Illustrates how to specify a 1st level model using `MrGlm` and estimating its parameters using the classical restricted maximum Likelihood approach within SPM (Kiebel and Holmes, 2007). Note that this requires the output of `MrSeries/demo_preprocessing`.

`MrSeries/demo_model_estimation_1st_level_Bayesian.m`: Illustrates how to estimate the same model as in `MrSeries/demo_model_estimation_1st_level` using a Variational Bayesian framework (Penny et al., 2003). Note that this requires the output of `MrSeries/demo_model_estimation_1st_level` and `MrSeries/demo_preprocessing`.

`MrSeries/demo_preprocessing.m`: Example preprocessing script for fMRI data. Illustrates how `MrSeries` automatically updates data and populates appropriate properties such as `mean`, `snr`, `sd` images, tissue probability maps and masks.

`MrSeries/demo_snr_analysis_mrseries.m`: Example of a tSNR assessment in different ROIs illustrating the impact of different preprocessing steps on tSNR in grey matter.

`MrDimInfo/demo_dim_info.m`: The `MrDimInfo` class implements data selection and access used in plots and computations. The demo covers the creation of `dimInfo` objects, retrieving parameters via `get_dims` and `dimInfo.dimLabel`, adding/setting dimensions, retrieving array indices and sampling points, selecting a subset of dimensions and creating `dimInfos` from files. Note that `dimInfo` does not know about the `affineGeometry`, i.e. all sampling points are with reference to the data matrix.

`MrAffineGeometry/demo_affine_geometry.m`: Exemplifies creation of a `MrAffineGeometry` object using a nifti file, a Philips par/rec file, prop/val pairs or an affine transformation matrix.

`MrImageGeometry/demo_image_geometry.m`: Shows how an `MrImageGeometry` object can be created from file or via `MrDimInfo` and `MrAffineGeometry` objects.

`MrDataNd/demo_save.m`: Illustrates how data are split to allow compatibility with SPM read-in.

`MrCopyData/demo_copy_data.m`: Shows the functionality of `MrCopyData` for deep cloning and recursive operations.

4.4 Discussion and conclusion

4.4.1 Summary

We have presented the uniQC toolbox that integrates image operations and visualisation for multi-dimensional data sets. UniQC provides a framework with intuitive access to well-established SPM operations and versatile built-in MATLAB functions. Thus, it enables the implementation of flexible and interactive analysis workflows during (f)MRI sequence development and the adaptive design of QC pipelines when translating new acquisition techniques into neuroscientific practice.

Following the development towards the acquisition of large data sets (Van Essen et al., 2013), QC analysis (Esteban et al., 2017) and the prescription of complex analysis pipelines (Gorgolewski et al., 2011) have produced powerful tools to handle large data sets. In contrast, Lipsia (Lohmann et al., 2001) provides advanced visualisation tools for statistical maps on cortical segmentations, but is very prescriptive with regard to the performed analysis. UniQC takes a slightly different stance, and focuses on the in-depth analysis of one data set, as often encountered in methods development, ideally right next to the scanner console during data acquisition. Therein, flexibility, reproducibility and accessibility are pursued by adapting an already established syntax, i.e. MATLAB and SPM commands, the modularization of workflows into small functional units, and the integration of comprehensive meta-data for documentation.

4.4.2 Comparison to other fMRI analysis software

Most SPM user will be familiar with `spm_imcalc`, and also its restrictions to either a few images or operations along the 4th dimension. Thus, `spm_imcalc` is sufficient to compute a tSNR image, but lacks flexibility to easily compare the average tSNR within a ROI before and after realignment (see `demo_snr_analysis_mrseries` for the implementation within uniQC). The FSL software package (Jenkinson et al., 2012) provides similar functions as uniQC. However, a fundamental difference is the strictly defined dimensionality (4D image time series for fMRI) in FSL, which is not the case in uniQC. Further, uniQC is integrated into a powerful and versatile development environment (MATLAB), whereas a text editor is sufficient, but also the limit, for the development of shell scripts as used in FSL. For example, executing one code section at a time in MATLAB allows the concurrent development and documentation of a performed analysis. Visualisation (*fslview*), matrix operations (*fslmaths*) and processing options (e.g. *flirt*) are all separate programs in FSL, and their integration is required solely from the user side. The documentation of the processing steps is also the

responsibility of the user, especially when using the GUI or the command line. To increase the ease of use, uniQC features one common interface to all processing steps, allows their straightforward concatenation and provides versatile and built-in documentation options.

Apart from new conceptual developments, the integration of uniQC into SPM and MATLAB provides a number of important advantages to lower the barrier of entry in comparison to other software packages such as MINC[11], AFNI (Cox, 1996), Freesurfer (Fischl, 2012) and FSL – at the cost of requiring a MATLAB license. In particular, the high-level language and the syntax chosen in uniQC allows also non-expert programmers to easily express their ideas and interact playfully with the data. Additionally, the cross-platform compatibility of uniQC allows different users to collaboratively evaluate a data set or the same user to analyse their data using different underlying computing infrastructure. In comparison, MINC, AFNI, Freesurfer and FSL are all intended for Linux – and often specific flavours or versions thereof – or MacOS. Using these tools under Windows either requires virtual machines, WSL[12], or Cygwin[13] rebuilds, which then need constant maintenance from the developers[14]. As a consequence, MINC, AFNI and FSL require, next to elaborate installation guidelines, root access/administrator privileges[15,16,17], which are often not available on shared infrastructure. However, the installation of uniQC amounts to downloading SPM and uniQC and adding the path of the respective directories (`addpath(SpmDirectory)` for SPM and `addpath(genpath(uniQcDirectory))` for uniQC). The most important advantage, though, is the easy integration of extensions or new algorithms. Because MATLAB code is directly interpreted, the underlying code is readily accessible and readable, and new features do not require re-compilation for different platforms. This allows to build a user and developer community, where already existing MATLAB code can be integrated and new features can be added without requiring experience in C++ or other low-level languages. Due to the modularisation, provided by the object-oriented design, users will not require a full immersion into the uniQC code base to extend the functionality of the framework.

[11] https://en.wikibooks.org/wiki/MINC
[12] https://en.wikipedia.org/wiki/Windows_Subsystem_for_Linux
[13] https://www.cygwin.com/
[14] from https://en.wikibooks.org/wiki/MINC/Tutorials/BinaryInstalls accessed at the 27th of May, 2018: "For this build type I have not yet figured out a nice consistent way to build .deb dpkg files under debian that work. Nor have I put the time into figuring our the cygwin installer package structure (but will eventually). So what this means is that the cygwin download is a static .tar.gz archive of pre-compiled binaries that I build and release from time to time."
[15] https://en.wikibooks.org/wiki/MINC/Tutorials/BinaryInstalls
[16] https://afni.nimh.nih.gov/pub/dist/doc/htmldoc/background_install/install_instructs/steps_linux_ubuntu16.html
[17] https://fsl.fmrib.ox.ac.uk/fsl/fslwiki/FslInstallation/Linux

UniQC is in particular driven to facilitate the interaction between the data and the users, allowing them to bring their expert knowledge into the data evaluation. In contrast to MINC, AFNI, Freesurfer, FSL, MRIQC, Nypipe and Lipsia, which are developed for fMRI data analysis to investigate brain function, uniQC specifically targets the data analysis performed during the development of new data acquisition techniques (Figure 4-9). Thus, uniQC will be valuable to everyone who requires a general framework for the analysis of high-dimensional images, sequence and methods developers who are familiar with MATLAB but have limited experience with neuroimaging analysis software, and for SPM – users who want to add a QC pipeline to their standard analysis. Specifically during the translation into neuroscientific practice, one has to ascertain that the chosen method is appropriate for the designated application and the obtained benefits outweigh the additional effort. Additionally, an adaptive QC framework is required to ensure the continuous performance of a new technique. Therein, the quality measures established during the initial development need to be closely monitored to identify problems early on, along-side the more common outcomes of complex fMRI data analysis pipelines.

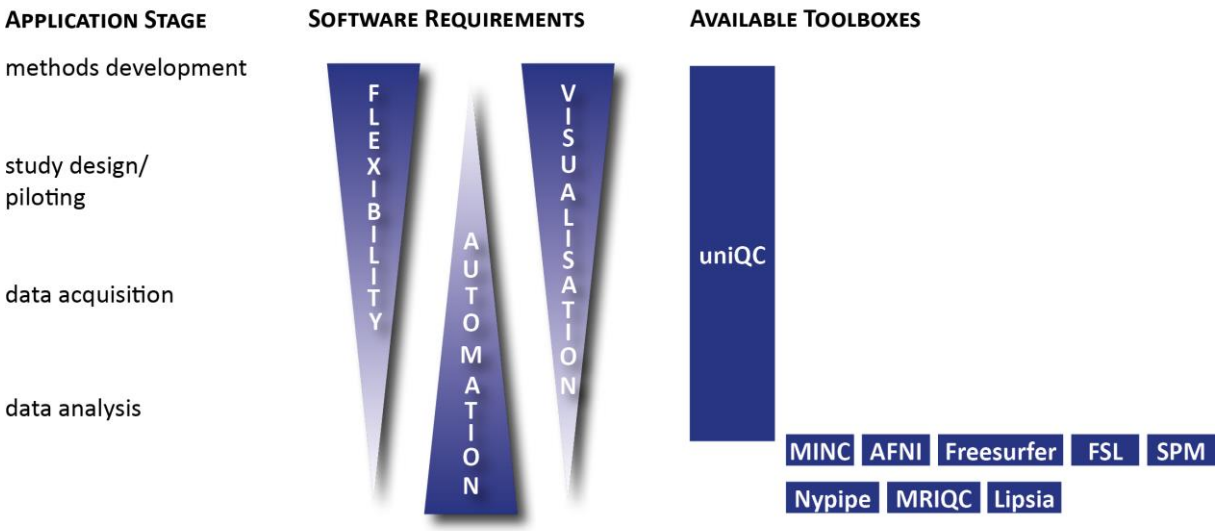

Figure 4-9: Application stages and corresponding software requirements for image processing toolboxes. The uniQC toolbox main application stage is methods development and the translation of these methods into neuroscientific practice. During the pilot of a study, for example, different options need to be considered before the data acquisition from a group of subject begins. During the data acquisition, the established quality measures need to be closely monitored. Ultimately, many tools are available for data analysis of large data sets, but the established workflows through uniQC can be translated up to this stage.

4.4.3 Limitations and Outlook

Limitations of uniQC include its dependence on the object-oriented framework in MATLAB, which is rapidly developing. Thus, fairly recent versions of MATLAB are required for good performance and full functionality, e.g. `testsuite` (introduced in R2016a) or `numArgumentsFromSubscript` for `subsref` (introduced in R2015b). Additionally, the storage of large data matrices in RAM and the creation of `MrCopyObjects` within methods can reduce performance in environments with low memory capabilities.

Next enhancements of uniQC include the support of other data or file formats, such as read-in functions for ISMRMRD or BIDS file structures, additional plot operations for `MrDataNd` to better visualize k-space data or k-space trajectories, and the extension of the unit test to all constructors and critical methods.

4.5 Software note

UniQC is released under the GPL (version 3.0) and available online via https://github.com/CAIsr/uniQC.

4.6 Acknowledgements

We thank all supervisors for allowing to work on this project, which needs perseverance and belief, since it will only pay off in the long run, and Michael Wyss and Laetitia Vionnet for extensive beta-testing and helpful feedback on new functionality. We appreciate the input provided by Steffen Bollmann on the intricacies of other toolboxes, in particular MINC.

Chapter 5

Discussion and Conclusion

5.1 Summary

The non-invasive investigation of brain function using fMRI has significantly advanced our understanding of cognitive processes and brain diseases (see e.g. Bullmore, 2012; Rosen and Savoy, 2012). Therein, functional sensitivity needs to be sufficiently high to obtain a faithful representation of the underlying neurovascular activity. Ascertaining adequate functional sensitivity homogeneously across the whole brain can be challenging, because it depends not only on the employed acquisition protocol, but also on its interaction with the underlying tissue microstructure. For example, increased iron levels as encountered in the sub-cortical nuclei of the basal ganglia reduce the effective transverse relaxation time T_2^*. Thus, the functional sensitivity in these areas is reduced compared to cortical regions. In this thesis, I have investigated the performance of multi-echo fMRI to overcome these limitations. I showed that functional sensitivity could be successfully increased in the basal ganglia nuclei, while preserving the sensitivity at the level of the cortex (Chapter 2 – *Using multi-echo simultaneous multi-slice (SMS) EPI to improve functional MRI of the subcortical nuclei of the basal ganglia at ultra-high field (7T)*). This findings suggest that multi-echo fMRI might be particularly beneficial when investigating motor functions in patients with Parkinson's disease as these patients have been shown to have heavily increased iron levels in the caudate and globus pallidus (Wang et al., 2016), and, hence considerably shorter T_2^* in these areas compared to healthy controls. As demonstrated here, by using multi-echo fMRI it is possible to tailor the functional sensitivity to the properties of the underlying tissue, promising the means to overcome this issue.

To further the general applicability of fMRI at the single-subject level, I have investigated the impact of simultaneous multi-slice (SMS) acquisitions on functional sensitivity (Breuer et al., 2005; Feinberg et al., 2010; Larkman et al., 2001; Setsompop et al., 2012). This sequence type provides increased acquisition speed, i.e. more samples per unit time, and, thereby, increased statistical power to detect an effect. Especially when using fMRI to make clinically relevant predictions, valid inference at the single-subject level is necessary (Branco et al., 2016; Stephan et al., 2017b). Here, I showed that modelling of physiological noise sources such as cardiac and respiratory activity, in combination with advanced pre-whitening schemes are crucial for single-subject fMRI using fast acquisition schemes (Chapter 3 - *Serial correlations in single-subject fMRI with sub-second TR*). Thus, the concurrent measurement of cardiac and respiratory traces should from part of every fMRI experiment at 7T.

Over the course of this thesis, it has been necessary to assess functional sensitivity across all levels ranging from basic image quality to temporal signal-to-noise-ratios (tSNR),

contrast-to-noise-ratios (CNR), and t-scores. In particular during the development and evaluation of new acquisition strategies (Bollmann et al., 2017, Chapter 2 and Chapter 3), these measures need to be computed in a flexible, yet easily accessible manner. In particular, the convenient handling of multi-dimensional data, for example obtained by multi-echo fMRI (Chapter 2), is not integrated in other fMRI analysis software. Thus, a general framework for the analysis of fMRI data and the evaluation of functional sensitivity has been developed. As a result, the uniQC toolbox was conceived to represent MRI data of arbitrary dimensionality and generalize matrix, image and preprocessing operations across these dimensions (Chapter 4 - *Interactive and flexible quality control in fMRI sequence evaluation: the uniQC toolbox*). For example, developmental versions of uniQC have already substantially simplified the evaluation of new acquisition schemes (Chapter 3, Bollmann et al., 2018; Kasper et al., 2018; Wyss et al., 2017), improvement of contrast mechanisms for arterial spin labelling at ultra-high field (Zimmer et al., 2016) and assessment of advanced noise modelling schemes (Kasper et al., 2017).

5.2 Advanced pre-whitening schemes for single-subject fMRI

Following the initial assessment of the pre-whitening performance of the FAST model in Chapter 3, Corbin et al. (2018) have provided a more detailed evaluation. In particular, they have assessed the pre-whitening performance based on the TR and the number of model components, and observed a slight dependence on the subject and the TR. They confirmed our finding that the AR(1) model is insufficient to accurately model serial correlations in sequences with short TR. In conclusion, they could derive a robust FAST model, which, in combination with physiological noise modelling, showed good pre-whitening performance across a range of TRs and high computational stability.

5.3 T-score testing for the mean as a measure of functional sensitivity

Revisiting the definition of BOLD sensitivity in equation (14)

$$S_{BOLD} = \frac{\Delta I|_{T_2^* \to T_2^* + \Delta T_2^*} \cdot \sqrt{N}}{\sigma_{time}}.$$

shows a number of similarities to the t-score presented in equation (7).

$$T = \frac{c^T \hat{\beta}}{\sqrt{\hat{\sigma}^2 c^T (X^T X)^{-1} c}}.$$

In both, a measure of effect size (ΔI and $\hat{\beta}$, respectively) is compared to the variance of the noise (σ_{time} and $\hat{\sigma}$). A notable difference is the assumption of an independent and identically distributed error in equation (14), which is not the case for fMRI time series, and in particular

not for acquisitions with short TR (Chapter 3). Further, equation (14) does not take into account noise modelling in the GLM, which can substantially increase BOLD sensitivity by reducing $\hat{\sigma}$ (Hutton et al., 2011; Kasper et al., 2017). In particular in the presence of serial correlations, t-scores estimated using an appropriate pre-whitening model represent a more accurate measure of BOLD sensitivity.

However, if noise properties of different sequences or the increased number of samples afforded by faster acquisitions are investigated, comparing t-scores rests on the assumption of equal effect sizes ΔI across different sessions. Since the BOLD response can be significantly altered by covariates such as attention even in primary sensory areas (Puckett et al., 2017), an elaborate design will be required to counteract these effects (as implemented in Chapter 2). An alternative formulation, based on the GLM, has been introduced in Corbin et al. (2018). Therein, BOLD sensitivity is assessed by t-score testing for the mean signal $\bar{I}$:

$$S_{BOLD} = \frac{c_0^T \hat{\beta}}{\sqrt{\hat{\sigma}^2 c_0^T (X_w^T X_w)^{-1} c_0}} = \frac{\bar{I}}{\hat{\sigma}\eta_0} = \frac{tSNR}{\eta_0} \qquad (19)$$

where c_0 is the contrast vector for the mean, X_w is the pre-whitened design matrix, and η_0 characterizes the effective degrees of freedom. In the absence of serial correlations, η_0 reduces to $\sqrt{1/N}$, i.e. the degrees of freedom assumed in equation (14). However, the numerator between the two definitions differs. Here, the effect size estimates are excluded, making it an easy-to-apply measure for functional sensitivity. Therein, the overall temporal noise, the effect of confound modelling, the effect of pre-whitening, and the design efficiency including the effective degrees of freedom, can be assessed simultaneously (Corbin et al., 2018).

5.4 Implications for group-level inference

Most neuroimaging studies perform group level inference to generalize their findings to the population. Therein, mixed-effect analysis[18] are performed, which describe a hierarchical, two-level process, in which a population effect with a between-subject variance σ_b^2 give rise to an observation at the single-subject level with within-subject variance σ_w^2. Using a summary-statistics approach, the mean estimates $\hat{\beta}$ from the first level are taken as the input of the second level, thereby implicitly containing contributions from within- and between-subject variance. Since the restricted maximum likelihood estimation scheme provides

[18] Note that mixed-effects analysis as known from statistics have been introduced into the neuroimaging literature as random-effects analysis, but there is no difference between the two terms (Penny and Holmes, 2007).

unbiased parameter estimates, a group-level inference is extremely robust against underestimation of within-subject variance (Penny and Holmes, 2007). However, the group-level inference employed in Chapter 2 (Chen et al., 2012) explicitly combines effect size estimates and their variance. Since rapid acquisition schemes were used for both multi-echo and single-echo data, the single-subject t-scores might be inflated. However, the comparison performed in Chapter 2 still holds, because the within-subject variance is either equally underestimated in both conditions, or even more so for the single-echo condition because of its shorter TR. Thus, conclusions about the *relative* sensitivity can still be drawn. The impact of a full-mixed effects analysis compared to a summary statistics approach remains to be explored. For example, Kirilina et al. (2016) investigated advanced acquisition schemes using multi-echo and 3D readouts to increase functional sensitivity. While robust improvements where observed at the single-subject level, high inter-subject variability limited the translation to the group level. Similarly, we have observed even stronger improvements at the single subject level for the multi-echo acquisition (Chapter 2). In general, between-subject variance can have three underlying sources: true differences in neuronal activity, differences in physiology and variance introduced through the measurement process. An example of a known confound in physiology are age-related changes in the cerebrovascular system (Bangen et al., 2009). Further, the orientation of the cortical sheet to the main magnetic field can have a significant impact on the measured signal (Viessmann et al., 2018). Thus, new acquisition techniques may not only target variance at the single-subject level, but also reduce unwanted differences between subjects.

5.5 The impact of spatial specificity on statistical power

We have discussed the definition of functional sensitivity, and in particular how both BOLD sensitivity and spatial specificity influence overall functional sensitivity. Note that the definition of these two deviates from the definition of sensitivity (true positive rate) and specificity (true negative rate) in classical hypothesis testing. This originated from a challenge particular to fMRI, i.e. the use of voxel-based analysis to form topological inference. During the data acquisition, a continuous object is discretised, and the signal is averaged within pre-specified volume elements (= voxels). These voxels are neither independent nor does their spatial extent typically match organisational features of brain function. To draw conclusions independent from the underlying sampling grid, inference is usually performed to identify regions, cluster or peaks as active. Consequently, before sensitivity or specificity in the classical sense can be estimated, the underlying fundamental *test item*, and in particular its spatial extent, need to be specified. The spatial specificity

introduced here serves the purpose to illustrate the different parameters which define this test item. Importantly, spatial specificity also impacts BOLD sensitivity, and functional sensitivity thus needs to be evaluated considering both. Then, classical evaluation of sensitivity and specificity, such as receiver operating characteristics estimation can be performed (Nandy and Cordes, 2004; Skudlarski et al., 1999; Sorenson and Wang, 1996).

Especially in group analyses, fMRI faces a second challenge related to spatial specificity and BOLD sensitivity, caused by the small number of independent samples (subjects) compared to the large number of tested variables (voxels/clusters/peaks). This gives rise to two effects, the first one is the low reproducibility of fMRI studies due to inflated false positive rates (Button et al., 2013; Eklund et al., 2015; Ioannidis, 2005). In response, a white paper has been compiled by the neuroimaging community describing best practices in data analysis and sharing (Nichols et al., 2017), and commitments towards implementing these practices have been made by scientific journals ("Fostering reproducible fMRI research," 2017). However, inference in fMRI does not stop at the question of the presence or absence of an effect, but most of the interpretation rests on the spatial distribution of the observed activity pattern or estimated connectivity parameters. There, the second problem, which has been discussed to a lesser degree, but potentially has even larger impact, manifests. Cremers et al. (2017) show how too low power, i.e. too little sensitivity, does not simply lead to non-significant findings, but rather produces spurious, misleading patterns, which in turn lead to heavily compromised models of brain function. For example, strong, localized effects where observed in small subsamples with a typical group size for a cognitive task. However, the full spatial extent of the response could only be identified using the full sample with more than 450 participants. Furthermore, considerable differences between the regions identified as active within each subsample were observed, although all of them were contained within the results obtained from the whole sample. Consequently, spatial specificity needs to match the underlying distribution of neuronal activity for optimal functional sensitivity.

5.6 Outlook

We have seen how the definition of functional sensitivity has developed over time. Being initially a measure of effect size only (Deichmann et al., 2002) (eq. (9)), it evolved towards a measure of the ability to detect an effect above the noise floor (Poser et al., 2006) (eq. (12)). Following from the statistical analysis, it now incorporates also measures of how efficiently signal and noise can be estimated (Corbin et al., 2018) (eq. (19)). In the future, new demands could include estimates on power or reproducibility – accelerated through the

development towards clinical fMRI[19], or the ability to delineate fine-grained sub-structures (Kashyap et al., 2017). Thus, the interaction between the data acquisition and the analysis will continue to shape the definition of functional sensitivity.

[19] http://www.thebrainblog.org/2018/05/18/if-how-when-fmri-might-go-clinical/

Bibliography

Abosch, A., Yacoub, E., Ugurbil, K., Harel, N., 2010. An assessment of current brain targets for deep brain stimulation surgery with susceptibility-weighted imaging at 7 tesla. Neurosurgery 67, 1745–56; discussion 1756. https://doi.org/10.1227/NEU.0b013e3181f74105

Abragam, A., 1983. Principles of Nuclear Magnetism. Clarendon Press, Oxford.

Arbabshirani, M.R., Damaraju, E., Phlypo, R., Plis, S., Allen, E., Ma, S., Mathalon, D., Preda, A., Vaidya, J.G., Adali, T., Calhoun, V.D., 2014. Impact of autocorrelation on functional connectivity. NeuroImage 102, 294–308. https://doi.org/10.1016/j.neuroimage.2014.07.045

Ashburner, J., Friston, K.J., 2005. Unified segmentation. NeuroImage 26, 839–851. https://doi.org/10.1016/j.neuroimage.2005.02.018

Attwell, D., Iadecola, C., 2002. The neural basis of functional brain imaging signals. Trends Neurosci. 25, 621–625.

Balteau, E., Hutton, C., Weiskopf, N., 2010. Improved shimming for fMRI specifically optimizing the local BOLD sensitivity. NeuroImage 49, 327–336. https://doi.org/10.1016/j.neuroimage.2009.08.010

Bandettini, P. (Ed.), 2012. 20 Years of fMRI. NeuroImage 62, 575–1324.

Bandettini, P.A., Wong, E.C., Hinks, R.S., Tikofsky, R.S., Hyde, J.S., 1992. Time course EPI of human brain function during task activation. Magn. Reson. Med. 25, 390–397.

Bangen, K.J., Restom, K., Liu, T.T., Jak, A.J., Wierenga, C.E., Salmon, D.P., Bondi, M.W., 2009. Differential age effects on cerebral blood flow and BOLD response to encoding: Associations with cognition and stroke risk. Neurobiol. Aging 30, 1276–1287. https://doi.org/10.1016/j.neurobiolaging.2007.11.012

Barmet, C., Zanche, N.D., Pruessmann, K.P., 2008. Spatiotemporal magnetic field monitoring for MR. Magn. Reson. Med. 60, 187–197. https://doi.org/10.1002/mrm.21603

Barth, M., Breuer, F., Koopmans, P.J., Norris, D.G., Poser, B.A., 2016. Simultaneous multislice (SMS) imaging techniques: SMS Imaging. Magn. Reson. Med. 75, 63–81. https://doi.org/10.1002/mrm.25897

Barth, M., Metzler, A., Klarhofer, M., Roll, S., Moser, E., Leibfritz, D., 1999. Functional MRI of the human motor cortex using single-shot, multiple gradient-echo spiral imaging. Magn Reson Imaging 17, 1239–43.

Barth, M., Poser, B.A., 2011. Advances in High-Field BOLD fMRI. Materials 4, 1941–1955. https://doi.org/10.3390/ma4111941

Bednark, J.G., Campbell, M.E.J., Cunnington, R., 2015. Basal ganglia and cortical networks for sequential ordering and rhythm of complex movements. Front. Hum. Neurosci. 9. https://doi.org/10.3389/fnhum.2015.00421

Berger, M.C., Bachert, P., Gröbner, J., Nagel, A.M., 2016. Multi-contrast T2□-relaxometry upon visual stimulation at 3T and 7T. Magn. Reson. Imaging 34, 864–874. https://doi.org/10.1016/j.mri.2016.03.015

Bernstein, K.F.K., Xiaohong Joe Zhou Matt A., 2005. Handbook of MRI Pulse Sequences. Elsevier Science.

Bianciardi, M., Fukunaga, M., van Gelderen, P., Horovitz, S.G., de Zwart, J.A., Shmueli, K., Duyn, J.H., 2009. Sources of functional magnetic resonance imaging signal fluctuations in the human brain at rest: a 7 T study. Magn. Reson. Imaging 27, 1019–1029. https://doi.org/10.1016/j.mri.2009.02.004

Bianciardi, M., van Gelderen, P., Duyn, J.H., 2014. Investigation of BOLD fMRI resonance frequency shifts and quantitative susceptibility changes at 7 T. Hum. Brain Mapp. 35, 2191–2205. https://doi.org/10.1002/hbm.22320

Birn, R.M., Diamond, J.B., Smith, M.A., Bandettini, P.A., 2006. Separating respiratory-variation-related neuronal-activity-related fluctuations in fluctuations from fMRI. Neuroimage 31, 1536–1548. https://doi.org/10.1016/j.neuroimage.2006.02.048

Birn, R.M., Smith, M.A., Jones, T.B., Bandettini, P.A., 2008. The respiration response function: The temporal dynamics of fMRI signal fluctuations related to changes in respiration. NeuroImage 40, 644–654. https://doi.org/10.1016/j.neuroimage.2007.11.059

Boardman, A., Schlindwein, F.S., Rocha, A.P., 2002. A study on the optimum order of autoregressive models for heart rate variability. Physiol. Meas. 23, 325.

Bollmann, S., Bednark, J.G., Poser, B.A., Cunnington, R., Barth, M., 2015. Single-Echo vs Multi-Echo Acquisition for Simultaneous Multiband fMRI at 7T in the Basal Ganglia, in: Proceedings of the Organization for Human Brain Mapping 21. Presented at the HBM, Honolulu, USA, p. 1597.

Bollmann, S., Kasper, L., Vannesjo, S.J., Diaconescu, A.O., Dietrich, B.E., Gross, S., Stephan, K.E., Pruessmann, K.P., 2017. Analysis and correction of field fluctuations in fMRI data using field monitoring. NeuroImage. https://doi.org/10.1016/j.neuroimage.2017.01.014

Bollmann, S., Stab, D., Barth, M., 2018. BOLD fMRI with 0.5 mm isotropic voxel size and minimal in-plane distortion using 3D planes-on-a-paddlewheel (POP) EPI at 7 Tesla, in: Presented at the 26th Annual Meeting of the International Society for Magnetic Resonance Imaging in Medicine. Paris, France, p. 708.

Boxerman, J.L., Bandettini, P.A., Kwong, K.K., Baker, J.R., Davis, T.L., Rosen, B.R., Weisskoff, R.M., 1995. The intravascular contribution to fMRI signal change: Monte Carlo modeling and diffusion-weighted studies in vivo. Magn. Reson. Med. 34, 4–10.

Boyacioğlu, R., Schulz, J., Koopmans, P.J., Barth, M., Norris, D.G., 2015. Improved sensitivity and specificity for resting state and task fMRI with multiband multi-echo EPI compared to multi-echo EPI at 7 T. NeuroImage 119, 352–361. https://doi.org/10.1016/j.neuroimage.2015.06.089

Boyacioğlu, R., Schulz, J., Müller, N.C.J., Koopmans, P.J., Barth, M., Norris, D.G., 2014. Whole brain, high resolution multiband spin-echo EPI fMRI at 7T: A comparison with gradient-echo EPI using a color-word Stroop task. NeuroImage 97, 142–150. https://doi.org/10.1016/j.neuroimage.2014.04.011

Boynton, G.M., Engel, S.A., Glover, G.H., Heeger, D.J., 1996. Linear Systems Analysis of Functional Magnetic Resonance Imaging in Human V1. J. Neurosci. 16, 4207–4221.

Branco, P., Seixas, D., Castro, S.L., 2016. Temporal reliability of ultra-high field resting-state MRI for single-subject sensorimotor and language mapping. NeuroImage. https://doi.org/10.1016/j.neuroimage.2016.11.029

Brett, M., Johnsrude, I.S., Owen, A.M., 2002. The problem of functional localization in the human brain. Nat. Rev. Neurosci. 3, 243–249. https://doi.org/10.1038/nrn756

Breuer, F.A., Blaimer, M., Heidemann, R.M., Mueller, M.F., Griswold, M.A., Jakob, P.M., 2005. Controlled aliasing in parallel imaging results in higher acceleration (CAIPIRINHA) for multi-slice imaging. Magn. Reson. Med. 53, 684–691. https://doi.org/10.1002/mrm.20401

Bright, M.G., Murphy, K., 2013. Reliable quantification of BOLD fMRI cerebrovascular reactivity despite poor breath-hold performance. Neuroimage 83, 559. https://doi.org/10.1016/j.neuroimage.2013.07.007

Brown, R.W., Cheng, Y.-C.N., Haacke, E.M., Thompson, M.R., Venkatesan, R., 2014a. Chapter 4 - Magnetization, Relaxation, and the Bloch Equation, in: Magnetic Resonance Imaging. Wiley, pp. 53–66. https://doi.org/10.1002/9781118633953.ch4

Brown, R.W., Cheng, Y.-C.N., Haacke, E.M., Thompson, M.R., Venkatesan, R., 2014b. Chapter 18 - Fast Imaging in the Steady State, in: Magnetic Resonance Imaging. Wiley, pp. 447–510. https://doi.org/10.1002/9781118633953.ch18

Brown, R.W., Cheng, Y.-C.N., Haacke, E.M., Thompson, M.R., Venkatesan, R., 2014c. Chapter 10 - Multi-Dimensional Fourier Imaging and Slice Excitation, in: Magnetic Resonance Imaging. Wiley, pp. 165–206. https://doi.org/10.1002/9781118633953.ch10

Brown, R.W., Cheng, Y.-C.N., Haacke, E.M., Thompson, M.R., Venkatesan, R., 2014d. Magnetic Resonance Imaging: Physical Principles and Sequence Design. Wiley. https://doi.org/10.1002/9781118633953

Brunheim, S., Johst, S., Pfaffenrot, V., Maderwald, S., Quick, H.H., Poser, B.A., 2017. Variable slice thickness (VAST) EPI for the reduction of susceptibility artifacts in whole-brain GE-EPI at 7 Tesla. MAGMA. https://doi.org/10.1007/s10334-017-0641-0

Bullmore, E., 2012. The future of functional MRI in clinical medicine. NeuroImage, 20 YEARS OF fMRI 62, 1267–1271. https://doi.org/10.1016/j.neuroimage.2012.01.026

Button, K.S., Ioannidis, J.P.A., Mokrysz, C., Nosek, B.A., Flint, J., Robinson, E.S.J., Munafò, M.R., 2013. Power failure: why small sample size undermines the reliability of neuroscience. Nat. Rev. Neurosci. 14, 365–376. https://doi.org/10.1038/nrn3475

Buxton, R.B., Wong, E.C., Frank, L.R., 1998. Dynamics of blood flow and oxygenation changes during brain activation: The balloon model. Magn. Reson. Med. 39, 855–864. https://doi.org/10.1002/mrm.1910390602

Caballero-Gaudes, C., Reynolds, R.C., 2016. Methods for cleaning the BOLD fMRI signal. NeuroImage. https://doi.org/10.1016/j.neuroimage.2016.12.018

Chaimow, D., Uğurbil, K., Shmuel, A., 2018. Optimization of functional MRI for detection, decoding and high-resolution imaging of the response patterns of cortical columns. NeuroImage 164, 67–99. https://doi.org/10.1016/j.neuroimage.2017.04.011

Chang, C., Cunningham, J.P., Glover, G.H., 2009. Influence of heart rate on the BOLD signal: The cardiac response function. NeuroImage 44, 857–869. https://doi.org/10.1016/j.neuroimage.2008.09.029

Chen, G., Saad, Z.S., Nath, A.R., Beauchamp, M.S., Cox, R.W., 2012. FMRI group analysis combining effect estimates and their variances. NeuroImage 60, 747–765. https://doi.org/10.1016/j.neuroimage.2011.12.060

Chen, L., T. Vu, A., Xu, J., Moeller, S., Ugurbil, K., Yacoub, E., Feinberg, D.A., 2015. Evaluation of highly accelerated simultaneous multi-slice EPI for fMRI. NeuroImage 104, 452–459. https://doi.org/10.1016/j.neuroimage.2014.10.027

Cohen-Adad, J., Polimeni, J.R., Helmer, K.G., Benner, T., McNab, J.A., Wald, L.L., Rosen, B.R., Mainero, C., 2012. T(2)* mapping and B(0) orientation-dependence at 7 T reveal cyto- and myeloarchitecture organization of the human cortex. Neuroimage 60, 1006–1014. https://doi.org/10.1016/j.neuroimage.2012.01.053

Corbin, N., Todd, N., Friston, K., Callaghan, M., 2018. Accurate modelling of temporal correlations in rapidly sampled fMRI time series. HBM in press.

Cox, R.W., 1996. AFNI: software for analysis and visualization of functional magnetic resonance neuroimages. Comput Biomed Res 29, 162–73.

Cremers, H.R., Wager, T.D., Yarkoni, T., 2017. The relation between statistical power and inference in fMRI. PLOS ONE 12, e0184923. https://doi.org/10.1371/journal.pone.0184923

Cunnington, R., Windischberger, C., Deecke, L., Moser, E., 2002. The preparation and execution of self-initiated and externally-triggered movement: a study of event-related fMRI. Neuroimage 15, 373–85. https://doi.org/10.1006/nimg.2001.0976

Dagli, S.M., Ingeholm, J.E., Haxby, J.V., 1999. Localization of Cardiac-Induced Signal Change in fMRI. NeuroImage 9, 407–415. https://doi.org/10.1006/nimg.1998.0424

De Martino, F., Esposito, F., van de Moortele, P.-F., Harel, N., Formisano, E., Goebel, R., Ugurbil, K., Yacoub, E., 2011. Whole brain high-resolution functional imaging at ultra

high magnetic fields: An application to the analysis of resting state networks. NeuroImage 57, 1031–1044. https://doi.org/10.1016/j.neuroimage.2011.05.008
De Panfilis, C., Schwarzbauer, C., 2005. Positive or negative blips? The effect of phase encoding scheme on susceptibility-induced signal losses in EPI. NeuroImage 25, 112–121. https://doi.org/10.1016/j.neuroimage.2004.11.014
Deichmann, R., Josephs, O., Hutton, C., Corfield, D.R., Turner, R., 2002. Compensation of Susceptibility-Induced BOLD Sensitivity Losses in Echo-Planar fMRI Imaging. NeuroImage 15, 120–135. https://doi.org/10.1006/nimg.2001.0985
Deistung, A., Schafer, A., Schweser, F., Biedermann, U., Turner, R., Reichenbach, J.R., 2013. Toward in vivo histology: a comparison of quantitative susceptibility mapping (QSM) with magnitude-, phase-, and R2*-imaging at ultra-high magnetic field strength. Neuroimage 65, 299–314. https://doi.org/10.1016/j.neuroimage.2012.09.055
Desikan, R.S., Ségonne, F., Fischl, B., Quinn, B.T., Dickerson, B.C., Blacker, D., Buckner, R.L., Dale, A.M., Maguire, R.P., Hyman, B.T., Albert, M.S., Killiany, R.J., 2006. An automated labeling system for subdividing the human cerebral cortex on MRI scans into gyral based regions of interest. NeuroImage 31, 968–980. https://doi.org/10.1016/j.neuroimage.2006.01.021
Drayer, B., Burger, P., Darwin, R., Riederer, S., Herfkens, R., Johnson, G.A., 1986. MRI of brain iron. AJR Am J Roentgenol 147, 103–10. https://doi.org/10.2214/ajr.147.1.103
Duerst, Y., Wilm, B.J., Dietrich, B.E., Vannesjo, S.J., Barmet, C., Schmid, T., Brunner, D.O., Pruessmann, K.P., 2015. Real-time feedback for spatiotemporal field stabilization in MR systems. Magn. Reson. Med. 73, 884–893. https://doi.org/10.1002/mrm.25167
Duyn, J.H., Moonen, C.T.W., Yperen, G.H. van, Boer, R.W. de, Luyten, P.R., 1994. Inflow versus deoxyhemoglobin effects in bold functional MRI using gradient echoes at 1.5 T. NMR Biomed. 7, 83–88. https://doi.org/10.1002/nbm.1940070113
Edelstein, W.A., Glover, G.H., Hardy, C.J., Redington, R.W., 1986. The intrinsic signal-to-noise ratio in NMR imaging. Magn. Reson. Med. 3, 604–618. https://doi.org/10.1002/mrm.1910030413
Eklund, A., Andersson, M., Josephson, C., Johannesson, M., Knutsson, H., 2012. Does parametric fMRI analysis with SPM yield valid results?—An empirical study of 1484 rest datasets. NeuroImage 61, 565–578. https://doi.org/10.1016/j.neuroimage.2012.03.093
Eklund, A., Nichols, T., Knutsson, H., 2015. Can parametric statistical methods be trusted for fMRI based group studies?
Falahpour, M., Refai, H., Bodurka, J., 2013. Subject specific BOLD fMRI respiratory and cardiac response functions obtained from global signal. NeuroImage 72, 252–264. https://doi.org/10.1016/j.neuroimage.2013.01.050
Feinberg, D.A., Moeller, S., Smith, S.M., Auerbach, E., Ramanna, S., Glasser, M.F., Miller, K.L., Ugurbil, K., Yacoub, E., 2010. Multiplexed Echo Planar Imaging for Sub-Second Whole Brain FMRI and Fast Diffusion Imaging. PLoS ONE 5, e15710. https://doi.org/10.1371/journal.pone.0015710
Fera, F., Yongbi, M.N., van Gelderen, P., Frank, J.A., Mattay, V.S., Duyn, J.H., 2004. EPI-BOLD fMRI of human motor cortex at 1.5 T and 3.0 T: Sensitivity dependence on echo time and acquisition bandwidth. J. Magn. Reson. Imaging 19, 19–26. https://doi.org/10.1002/jmri.10440
Fischl, B., 2012. FreeSurfer. NeuroImage 62, 774–781. https://doi.org/10.1016/j.neuroimage.2012.01.021
Fonov, V., Evans, A., McKinstry, R., Almli, C., Collins, D., 2009. Unbiased nonlinear average age-appropriate brain templates from birth to adulthood. NeuroImage 47, S102. https://doi.org/10.1016/S1053-8119(09)70884-5
Fostering reproducible fMRI research, 2017. . Nat. Neurosci. 20, 298.

Fox, P.T., Raichle, M.E., 1986. Focal physiological uncoupling of cerebral blood flow and oxidative metabolism during somatosensory stimulation in human subjects. Proc. Natl. Acad. Sci. U. S. A. 83, 1140–1144.

Fox, P.T., Raichle, M.E., Mintun, M.A., Dence, C., 1988. Nonoxidative glucose consumption during focal physiologic neural activity. Science 241, 462–464.

Frazier, J.A., Chiu, S., Breeze, J.L., Makris, N., Lange, N., Kennedy, D.N., Herbert, M.R., Bent, E.K., Koneru, V.K., Dieterich, M.E., Hodge, S.M., Rauch, S.L., Grant, P.E., Cohen, B.M., Seidman, L.J., Caviness, V.S., Biederman, J., 2005. Structural Brain Magnetic Resonance Imaging of Limbic and Thalamic Volumes in Pediatric Bipolar Disorder. Am. J. Psychiatry 162, 1256–1265. https://doi.org/10.1176/appi.ajp.162.7.1256

Frederick, B. deB., Nickerson, L.D., Tong, Y., 2012. Physiological denoising of BOLD fMRI data using Regressor Interpolation at Progressive Time Delays (RIPTiDe) processing of concurrent fMRI and near-infrared spectroscopy (NIRS). NeuroImage 60, 1913–1923. https://doi.org/10.1016/j.neuroimage.2012.01.140

Friedman, L., Glover, G.H., 2006. Report on a multicenter fMRI quality assurance protocol. J. Magn. Reson. Imaging JMRI 23, 827–839. https://doi.org/10.1002/jmri.20583

Friston, K., 2007a. Chapter 19 - Topological Inference, in: Statistical Parametric Mapping: The Analysis of Funtional Brain Images. Elsevier/Academic Press, Amsterdam ; Boston.

Friston, K., 2007b. Chapter 2 - Statistical parametric mapping, in: Statistical Parametric Mapping: The Analysis of Funtional Brain Images. Elsevier/Academic Press, Amsterdam ; Boston.

Friston, K.J., Jezzard, P., Turner, R., 1994. Analysis of functional MRI time-series. Hum. Brain Mapp. 1, 153–171. https://doi.org/10.1002/hbm.460010207

Friston, K.J., Penny, W., Phillips, C., Kiebel, S., Hinton, G., Ashburner, J., 2002. Classical and Bayesian Inference in Neuroimaging: Theory. NeuroImage 16, 465–483. https://doi.org/10.1006/nimg.2002.1090

Friston, K.J., Penny, W.D., Ashburner, J.T., Kiebel, S.J., Nichols, T.E. (Eds.), 2006. Statistical Parametric Mapping: The Analysis of Functional Brain Images, 1 edition. ed. Academic Press, Amsterdam ; Boston.

Friston, K.J., Williams, S., Howard, R., Frackowiak, R.S., Turner, R., 1996. Movement-related effects in fMRI time-series. Magn. Reson. Med. 35, 346–355.

Gati, J.S., Menon, R.S., Uğurbil, K., Rutt, B.K., 1997. Experimental determination of the BOLD field strength dependence in vessels and tissue. Magn. Reson. Med. 38, 296–302. https://doi.org/10.1002/mrm.1910380220

Geissler, A., Gartus, A., Foki, T., Tahamtan, A.R., Beisteiner, R., Barth, M., 2007. Contrast-to-noise ratio (CNR) as a quality parameter in fMRI. J. Magn. Reson. Imaging 25, 1263–1270. https://doi.org/10.1002/jmri.20935

Gelman, N., Gorell, J.M., Barker, P.B., Savage, R.M., Spickler, E.M., Windham, J.P., Knight, R.A., 1999. MR imaging of human brain at 3.0 T: preliminary report on transverse relaxation rates and relation to estimated iron content. Radiology 210, 759–67. https://doi.org/10.1148/radiology.210.3.r99fe41759

Genovese, C.R., Lazar, N.A., Nichols, T., 2002. Thresholding of statistical maps in functional neuroimaging using the false discovery rate. Neuroimage 15, 870–8. https://doi.org/10.1006/nimg.2001.1037

Glaser, D., Friston, K., 2007. Chapter 10 - Covariance Components, in: Statistical Parametric Mapping: The Analysis of Funtional Brain Images. Elsevier/Academic Press, Amsterdam ; Boston.

Glover, G.H., 2012. Spiral imaging in fMRI. NeuroImage 62, 706–712. https://doi.org/10.1016/j.neuroimage.2011.10.039

Glover, G.H., 1999a. Deconvolution of Impulse Response in Event-Related BOLD fMRI1. NeuroImage 9, 416–429. https://doi.org/10.1006/nimg.1998.0419
Glover, G.H., 1999b. 3D z-shim method for reduction of susceptibility effects in BOLD fMRI. Magn. Reson. Med. 42, 290–299. https://doi.org/10.1002/(SICI)1522-2594(199908)42:2<290::AID-MRM11>3.0.CO;2-N
Glover, G.H., Li, T.Q., Ress, D., 2000. Image-based method for retrospective correction of physiological motion effects in fMRI: RETROICOR. Magn. Reson. Med. 44, 162–167. https://doi.org/10.1002/1522-2594(200007)44:1<162::AID-MRM23>3.0.CO;2-E
Goldstein, J.M., Seidman, L.J., Makris, N., Ahern, T., O'Brien, L.M., Caviness, V.S., Kennedy, D.N., Faraone, S.V., Tsuang, M.T., 2007. Hypothalamic Abnormalities in Schizophrenia: Sex Effects and Genetic Vulnerability. Biol. Psychiatry 61, 935–945. https://doi.org/10.1016/j.biopsych.2006.06.027
Gonzalez-Castillo, J., Roopchansingh, V., Bandettini, P.A., Bodurka, J., 2011. Physiological noise effects on the flip angle selection in BOLD fMRI. NeuroImage 54, 2764–2778. https://doi.org/10.1016/j.neuroimage.2010.11.020
Gorno-Tempini, M.L., Hutton, C., Josephs, O., Deichmann, R., Price, C., Turner, R., 2002. Echo Time Dependence of BOLD Contrast and Susceptibility Artifacts. NeuroImage 15, 136–142. https://doi.org/10.1006/nimg.2001.0967
Grabner, G., Poser, B.A., Fujimoto, K., Polimeni, J.R., Wald, L.L., Trattnig, S., Toni, I., Barth, M., 2014. A study-specific fMRI normalization approach that operates directly on high resolution functional EPI data at 7Tesla. NeuroImage 100, 710–714. https://doi.org/10.1016/j.neuroimage.2014.06.045
Griswold, M.A., Jakob, P.M., Heidemann, R.M., Nittka, M., Jellus, V., Wang, J., Kiefer, B., Haase, A., 2002. Generalized autocalibrating partially parallel acquisitions (GRAPPA). Magn. Reson. Med. 47, 1202–1210. https://doi.org/10.1002/mrm.10171
Haacke, E.M., Cheng, N.Y., House, M.J., Liu, Q., Neelavalli, J., Ogg, R.J., Khan, A., Ayaz, M., Kirsch, W., Obenaus, A., 2005. Imaging iron stores in the brain using magnetic resonance imaging. Magn Reson Imaging 23, 1–25. https://doi.org/10.1016/j.mri.2004.10.001
Haacke, E.M., Xu, Y., Cheng, Y.C., Reichenbach, J.R., 2004. Susceptibility weighted imaging (SWI). Magn Reson Med 52, 612–8. https://doi.org/10.1002/mrm.20198
Hallgren, B., Sourander, P., 1958. The effect of age on the non-haemin iron in the human brain. J Neurochem 3, 41–51.
Harrison, L.M., Penny, W., Ashburner, J., Trujillo-Barreto, N., Friston, K.J., 2007. Diffusion-based spatial priors for imaging. NeuroImage 38, 677–695. https://doi.org/10.1016/j.neuroimage.2007.07.032
Harrison, L.M., Penny, W., Daunizeau, J., Friston, K.J., 2008. Diffusion-based spatial priors for functional magnetic resonance images. NeuroImage 41, 408–423. https://doi.org/10.1016/j.neuroimage.2008.02.005
Harvey, A.K., Pattinson, K.T.S., Brooks, J.C.W., Mayhew, S.D., Jenkinson, M., Wise, R.G., 2008. Brainstem functional magnetic resonance imaging: Disentangling signal from physiological noise. J. Magn. Reson. Imaging 28, 1337–1344. https://doi.org/10.1002/jmri.21623
Hoge, R.D., Atkinson, J., Gill, B., Crelier, G.R., Marrett, S., Pike, G.B., 1999. Linear coupling between cerebral blood flow and oxygen consumption in activated human cortex. Proc. Natl. Acad. Sci. U. S. A. 96, 9403–9408.
Holland, D., Kuperman, J.M., Dale, A.M., 2010. Efficient correction of inhomogeneous static magnetic field-induced distortion in Echo Planar Imaging. NeuroImage 50, 175–183. https://doi.org/10.1016/j.neuroimage.2009.11.044
Hoogenraad, F.G., Pouwels, P.J., Hofman, M.B., Rombouts, S.A., Lavini, C., Leach, M.O., Haacke, E.M., 2000. High-resolution segmented EPI in a motor task fMRI study. Magn Reson Imaging 18, 405–9.

Hu, X., Kim, S.-G., 1994. Reduction of signal fluctuation in functional MRI using navigator echoes. Magn. Reson. Med. 31, 495–503.
Huber, L., Handwerker, D.A., Jangraw, D.C., Chen, G., Hall, A., Stüber, C., Gonzalez-Castillo, J., Ivanov, D., Marrett, S., Guidi, M., Goense, J., Poser, B.A., Bandettini, P.A., 2017. High-Resolution CBV-fMRI Allows Mapping of Laminar Activity and Connectivity of Cortical Input and Output in Human M1. Neuron 96, 1253-1263.e7. https://doi.org/10.1016/j.neuron.2017.11.005
Huettel, S.A., Song, A.W., McCarthy, G., 2008. Functional Magnetic Resonance Imaging, 2nd edition. ed. Sinauer Associates, Sunderland, Mass.
Hutton, C., Bork, A., Josephs, O., Deichmann, R., Ashburner, J., Turner, R., 2002. Image Distortion Correction in fMRI: A Quantitative Evaluation. NeuroImage 16, 217–240. https://doi.org/10.1006/nimg.2001.1054
Hutton, C., Josephs, O., Stadler, J., Featherstone, E., Reid, A., Speck, O., Bernarding, J., Weiskopf, N., 2011. The impact of physiological noise correction on fMRI at 7 T. NeuroImage 57, 101–112. https://doi.org/10.1016/j.neuroimage.2011.04.018
Ioannidis, J.P.A., 2005. Why Most Published Research Findings Are False. PLoS Med. 2, e124. https://doi.org/10.1371/journal.pmed.0020124
Jenkinson, M., Beckmann, C.F., Behrens, T.E.J., Woolrich, M.W., Smith, S.M., 2012. FSL. NeuroImage, 20 YEARS OF fMRI 62, 782–790. https://doi.org/10.1016/j.neuroimage.2011.09.015
Jezzard, P., Clare, S., 1999. Sources of distortion in functional MRI data. Hum. Brain Mapp. 8, 80–85.
Kaneoke, Y., Donishi, T., Iwatani, J., Ukai, S., Shinosaki, K., Terada, M., 2012. Variance and Autocorrelation of the Spontaneous Slow Brain Activity. PLoS ONE 7, e38131. https://doi.org/10.1371/journal.pone.0038131
Kashyap, S., Ivanov, D., Havlicek, M., Poser, B.A., Uludağ, K., 2017. Impact of acquisition and analysis strategies on cortical depth-dependent fMRI. NeuroImage. https://doi.org/10.1016/j.neuroimage.2017.05.022
Kasper, L., 2014. Noise Reduction in fMRI Utilizing Concurrent Magnetic Field Monitoring (PhD Thesis). ETH Zurich.
Kasper, L., Bollmann, S., Diaconescu, A.O., Hutton, C., Heinzle, J., Iglesias, S., Hauser, T.U., Sebold, M., Manjaly, Z.-M., Pruessmann, K.P., Stephan, K.E., 2017. The PhysIO Toolbox for Modeling Physiological Noise in fMRI Data. J. Neurosci. Methods. https://doi.org/10.1016/j.jneumeth.2016.10.019
Kasper, L., Engel, M., Barmet, C., Haeberlin, M., Wilm, B.J., Dietrich, B.E., Schmid, T., Gross, S., Brunner, D.O., Stephan, K.E., Pruessmann, K.P., 2018. Rapid anatomical brain imaging using spiral acquisition and an expanded signal model. NeuroImage 168, 88–100. https://doi.org/10.1016/j.neuroimage.2017.07.062
Kasper, L., Haeberlin, M., Dietrich, B.E., Gross, S., Barmet, C., Wilm, B.J., Vannesjo, S.J., Brunner, D.O., Ruff, C.C., Stephan, K.E., Pruessmann, K.P., 2014. Matched-filter acquisition for BOLD fMRI. NeuroImage 100, 145–160. https://doi.org/10.1016/j.neuroimage.2014.05.024
Kass, R.E., Raftery, A.E., 1995. Bayes Factors. J. Am. Stat. Assoc. 90, 773–795. https://doi.org/10.1080/01621459.1995.10476572
Kettinger, Á., Hill, C., Vidnyánszky, Z., Windischberger, C., Nagy, Z., 2016. Investigating the Group-Level Impact of Advanced Dual-Echo fMRI Combinations. Front. Neurosci. 10. https://doi.org/10.3389/fnins.2016.00571
Keuken, M.C., Bazin, P.-L., Crown, L., Hootsmans, J., Laufer, A., Müller-Axt, C., Sier, R., van der Putten, E.J., Schäfer, A., Turner, R., Forstmann, B.U., 2014. Quantifying inter-individual anatomical variability in the subcortex using 7T structural MRI. NeuroImage 94, 40–46. https://doi.org/10.1016/j.neuroimage.2014.03.032

Kiebel, S.J., Holmes, A.P., 2007. Chapter 8 - The General Linear Model, in: Friston, K., Ashburner, J., Kiebel, S., Nichols, T., Penny, W. (Eds.), Statistical Parametric Mapping: The Analysis of Funtional Brain Images. Elsevier/Academic Press, Amsterdam ; Boston.

Kirilina, E., Lutti, A., Poser, B.A., Blankenburg, F., Weiskopf, N., 2016. The quest for the best: The impact of different EPI sequences on the sensitivity of random effect fMRI group analyses. NeuroImage 126, 49–59. https://doi.org/10.1016/j.neuroimage.2015.10.071

Koopmans, P.J., Barth, M., Norris, D.G., 2010. Layer-specific BOLD activation in human V1. Hum. Brain Mapp. 31, 1297–1304. https://doi.org/10.1002/hbm.20936

Koopmans, P.J., Barth, M., Orzada, S., Norris, D.G., 2011. Multi-echo fMRI of the cortical laminae in humans at 7T. NeuroImage 56, 1276–1285. https://doi.org/10.1016/j.neuroimage.2011.02.042

Krüger, G., Glover, G.H., 2001. Physiological noise in oxygenation-sensitive magnetic resonance imaging. Magn. Reson. Med. 46, 631–637.

Kundu, P., Inati, S.J., Evans, J.W., Luh, W.-M., Bandettini, P.A., 2012. Differentiating BOLD and non-BOLD signals in fMRI time series using multi-echo EPI. NeuroImage 60, 1759–1770. https://doi.org/10.1016/j.neuroimage.2011.12.028

Kundu, P., Santin, M.D., Bandettini, P.A., Bullmore, E.T., Petiet, A., 2014. Differentiating BOLD and non-BOLD signals in fMRI time series from anesthetized rats using multi-echo EPI at 11.7T. NeuroImage 102, 861–874. https://doi.org/10.1016/j.neuroimage.2014.07.025

Kundu, P., Voon, V., Balchandani, P., Lombardo, M.V., Poser, B.A., Bandettini, P.A., 2017. Multi-echo fMRI: A review of applications in fMRI denoising and analysis of BOLD signals. NeuroImage 154, 59–80. https://doi.org/10.1016/j.neuroimage.2017.03.033

Kwong, K.K., Belliveau, J.W., Chesler, D.A., Goldberg, I.E., Weisskoff, R.M., Poncelet, B.P., Kennedy, D.N., Hoppel, B.E., Cohen, M.S., Turner, R., 1992. Dynamic magnetic resonance imaging of human brain activity during primary sensory stimulation. Proc. Natl. Acad. Sci. 89, 5675–5679. https://doi.org/10.1073/pnas.89.12.5675

Larkman, D.J., Hajnal, J.V., Herlihy, A.H., Coutts, G.A., Young, I.R., Ehnholm, G., 2001. Use of multicoil arrays for separation of signal from multiple slices simultaneously excited. J. Magn. Reson. Imaging 13, 313–317. https://doi.org/10.1002/1522-2586(200102)13:2<313::AID-JMRI1045>3.0.CO;2-W

Lawrence, S.J.D., Formisano, E., Muckli, L., de Lange, F.P., 2017. Laminar fMRI: Applications for cognitive neuroscience. NeuroImage. https://doi.org/10.1016/j.neuroimage.2017.07.004

Lehericy, S., Bardinet, E., Tremblay, L., Van de Moortele, P.F., Pochon, J.B., Dormont, D., Kim, D.S., Yelnik, J., Ugurbil, K., 2006. Motor control in basal ganglia circuits using fMRI and brain atlas approaches. Cereb Cortex 16, 149–61. https://doi.org/10.1093/cercor/bhi089

Li, Z., Wu, G., Zhao, X., Luo, F., Li, S.J., 2002. Multiecho segmented EPI with z-shimmed background gradient compensation (MESBAC) pulse sequence for fMRI. Magn Reson Med 48, 312–21. https://doi.org/10.1002/mrm.10219

Liu, T.T., 2016. Noise contributions to the fMRI signal: An overview. NeuroImage 143, 141–151. https://doi.org/10.1016/j.neuroimage.2016.09.008

Logothetis, N.K., 2008. What we can do and what we cannot do with fMRI. Nature 453, 869–878. https://doi.org/10.1038/nature06976

Logothetis, N.K., Pauls, J., Augath, M., Trinath, T., Oeltermann, A., 2001. Neurophysiological investigation of the basis of the fMRI signal. Nature 412, 150–157.

Lohmann, G., Müller, K., Bosch, V., Mentzel, H., Hessler, S., Chen, L., Zysset, S., von Cramon, D.Y., 2001. Lipsia—a new software system for the evaluation of functional

magnetic resonance images of the human brain. Comput. Med. Imaging Graph. 25, 449–457. https://doi.org/10.1016/S0895-6111(01)00008-8
Lund, T.E., Madsen, K.H., Sidaros, K., Luo, W.-L., Nichols, T.E., 2006. Non-white noise in fMRI: Does modelling have an impact? NeuroImage 29, 54–66. https://doi.org/10.1016/j.neuroimage.2005.07.005
Makris, N., Goldstein, J.M., Kennedy, D., Hodge, S.M., Caviness, V.S., Faraone, S.V., Tsuang, M.T., Seidman, L.J., 2006. Decreased volume of left and total anterior insular lobule in schizophrenia. Schizophr. Res. 83, 155–171. https://doi.org/10.1016/j.schres.2005.11.020
Malonek, D., Dirnagl, U., Lindauer, U., Yamada, K., Kanno, I., Grinvald, A., 1997. Vascular imprints of neuronal activity: relationships between the dynamics of cortical blood flow, oxygenation, and volume changes following sensory stimulation. Proc. Natl. Acad. Sci. U. S. A. 94, 14826–14831.
Man, L.-C., Pauly, J.M., Macovski, A., 1997. Multifrequency interpolation for fast off-resonance correction. Magn. Reson. Med. 37, 785–792. https://doi.org/10.1002/mrm.1910370523
Mansfield, P., 1984. Real-time echo-planar imaging by NMR. Br. Med. Bull. 40, 187–190.
Marchini, J.L., Smith, S.M., 2003. On Bias in the Estimation of Autocorrelations for fMRI Voxel Time-Series Analysis. NeuroImage 18, 83–90. https://doi.org/10.1006/nimg.2002.1321
Marques, J.P., Kober, T., Krueger, G., van der Zwaag, W., Van de Moortele, P.-F., Gruetter, R., 2010. MP2RAGE, a self bias-field corrected sequence for improved segmentation and T1-mapping at high field. NeuroImage 49, 1271–1281. https://doi.org/10.1016/j.neuroimage.2009.10.002
Moeller, S., Yacoub, E., Olman, C.A., Auerbach, E., Strupp, J., Harel, N., Uğurbil, K., 2010. Multiband multislice GE-EPI at 7 tesla, with 16-fold acceleration using partial parallel imaging with application to high spatial and temporal whole-brain fMRI. Magn. Reson. Med. 63, 1144–1153. https://doi.org/10.1002/mrm.22361
Mountcastle, V.B., Berman, A.L., Davies, P.W., 1955. Topographic organization and modality representation in first somatic area of cat's cerebral cortex by method of single unit analysis. Am. J. Physiol. 183:464.
Murphy, K., Birn, R.M., Bandettini, P.A., 2013. Resting-state fMRI confounds and cleanup. NeuroImage 80, 349–359. https://doi.org/10.1016/j.neuroimage.2013.04.001
Murphy, K., Bodurka, J., Bandettini, P.A., 2007. How long to scan? The relationship between fMRI temporal signal to noise and necessary scan duration. NeuroImage 34, 565–574. https://doi.org/10.1016/j.neuroimage.2006.09.032
Murphy, K., Bright, M.G. (Eds.), 2017. Cleaning up the fMRI time series: Mitigating noise with advanced acquisition and correction strategies. NeuroImage 154, 1–282.
Nandy, R.R., Cordes, D., 2004. New approaches to receiver operating characteristic methods in functional magnetic resonance imaging with real data using repeated trials. Magn. Reson. Med. 52, 1424–1431. https://doi.org/10.1002/mrm.20263
Nasr, S., Polimeni, J.R., Tootell, R.B., 2016. Interdigitated Color- and Disparity-Selective Columns within Human Visual Cortical Areas V2 and V3. J Neurosci 36, 1841–57. https://doi.org/10.1523/JNEUROSCI.3518-15.2016
Nichols, T., Hayasaka, S., 2003. Controlling the familywise error rate in functional neuroimaging: a comparative review. Stat. Methods Med. Res. 12, 419–446. https://doi.org/10.1191/0962280203sm341ra
Nichols, T.E., Das, S., Eickhoff, S.B., Evans, A.C., Glatard, T., Hanke, M., Kriegeskorte, N., Milham, M.P., Poldrack, R.A., Poline, J.-B., 2017. Best practices in data analysis and sharing in neuroimaging using MRI. Nat. Neurosci. 20, 299.
O'Brien, K.R., Kober, T., Hagmann, P., Maeder, P., Marques, J., Lazeyras, F., Krueger, G., Roche, A., 2014. Robust T1-weighted structural brain imaging and morphometry at

7T using MP2RAGE. PLoS One 9, e99676. https://doi.org/10.1371/journal.pone.0099676
Ogawa, S., Lee, T.M., Kay, A.R., Tank, D.W., 1990. Brain magnetic resonance imaging with contrast dependent on blood oxygenation. Proc. Natl. Acad. Sci. 87, 9868–9872.
Ogawa, S., Tank, D.W., Menon, R., Ellermann, J.M., Kim, S.G., Merkle, H., Ugurbil, K., 1992. Intrinsic signal changes accompanying sensory stimulation: functional brain mapping with magnetic resonance imaging. Proc. Natl. Acad. Sci. 89, 5951–5955.
Okada, T., Yamada, H., Ito, H., Yonekura, Y., Sadato, N., 2005. Magnetic field strength increase yields significantly greater contrast-to-noise ratio increase: Measured using BOLD contrast in the primary visual area1. Acad. Radiol. 12, 142–147. https://doi.org/10.1016/j.acra.2004.11.012
Oostenveld, R., Fries, P., Maris, E., Schoffelen, J.-M., 2011. FieldTrip: Open Source Software for Advanced Analysis of MEG, EEG, and Invasive Electrophysiological Data. Comput. Intell. Neurosci. 2011, 1–9. https://doi.org/10.1155/2011/156869
Ordidge, R.J., Gorell, J.M., Deniau, J.C., Knight, R.A., Helpern, J.A., 1994. Assessment of relative brain iron concentrations using T2-weighted and T2*-weighted MRI at 3 Tesla. Magn. Reson. Med. 32, 335–341.
Özbay, P.S., Warnock, G., Rossi, C., Kuhn, F., Akin, B., Pruessmann, K.P., Nanz, D., 2016. Probing neuronal activation by functional quantitative susceptibility mapping under a visual paradigm: A group level comparison with BOLD fMRI and PET. NeuroImage 137, 52–60. https://doi.org/10.1016/j.neuroimage.2016.05.013
Penny, W., Flandin, G., Trujillo-Barreto, N., 2007. Bayesian comparison of spatially regularised general linear models. Hum. Brain Mapp. 28, 275–293. https://doi.org/10.1002/hbm.20327
Penny, W., Kiebel, S., Friston, K., 2003. Variational Bayesian inference for fMRI time series. NeuroImage 19, 727–741. https://doi.org/10.1016/S1053-8119(03)00071-5
Penny, W.D., Holmes, A.J., 2007. Chapter 12 - Random Effects Analysis, in: Friston, K.J., Ashburner, J., Kiebel, S., Nichols, T., Penny, W. (Eds.), Statistical Parametric Mapping. Academic Press, London, pp. 156–165.
Penny, W.D., Trujillo-Barreto, N.J., Friston, K.J., 2005. Bayesian fMRI time series analysis with spatial priors. NeuroImage 24, 350–362. https://doi.org/10.1016/j.neuroimage.2004.08.034
Peters, A.M., Brookes, M.J., Hoogenraad, F.G., Gowland, P.A., Francis, S.T., Morris, P.G., Bowtell, R., 2007. T2* measurements in human brain at 1.5, 3 and 7 T. Magn. Reson. Imaging 25, 748–753. https://doi.org/10.1016/j.mri.2007.02.014
Pohmann, R., Speck, O., Scheffler, K., 2016. Signal-to-noise ratio and MR tissue parameters in human brain imaging at 3, 7, and 9.4 tesla using current receive coil arrays. Magn. Reson. Med. 75, 801–809. https://doi.org/10.1002/mrm.25677
Polimeni, J., Uludag, K. (Eds.), 2018. Neuroimaging with Ultra-high Field MRI: Present and Future. NeuroImage 168, 1–532.
Polimeni, J.R., Renvall, V., Zaretskaya, N., Fischl, B., 2017. Analysis strategies for high-resolution UHF-fMRI data. NeuroImage. https://doi.org/10.1016/j.neuroimage.2017.04.053
Poser, B.A., Koopmans, P.J., Witzel, T., Wald, L.L., Barth, M., 2010. Three dimensional echo-planar imaging at 7 Tesla. NeuroImage 51, 261–266. https://doi.org/10.1016/j.neuroimage.2010.01.108
Poser, B.A., Norris, D.G., 2009. Investigating the benefits of multi-echo EPI for fMRI at 7 T. NeuroImage 45, 1162–1172. https://doi.org/10.1016/j.neuroimage.2009.01.007
Poser, B.A., Versluis, M.J., Hoogduin, J.M., Norris, D.G., 2006. BOLD contrast sensitivity enhancement and artifact reduction with multiecho EPI: Parallel-acquired inhomogeneity-desensitized fMRI. Magn. Reson. Med. 55, 1227–1235. https://doi.org/10.1002/mrm.20900

Posse, S., Wiese, S., Gembris, D., Mathiak, K., Kessler, C., Grosse-Ruyken, M.-L., Elghahwagi, B., Richards, T., Dager, S.R., Kiselev, V.G., 1999. Enhancement of BOLD-contrast sensitivity by single-shot multi-echo functional MR imaging. Magn. Reson. Med. 42, 87–97.

Pruessmann, K.P., Weiger, M., Scheidegger, M.B., Boesiger, P., 1999. SENSE: Sensitivity encoding for fast MRI. Magn. Reson. Med. 42, 952–962. https://doi.org/10.1002/(SICI)1522-2594(199911)42:5<952::AID-MRM16>3.0.CO;2-S

Puckett, A.M., Bollmann, S., Barth, M., Cunnington, R., 2017. Measuring the effects of attention to individual fingertips in somatosensory cortex using ultra-high field (7T) fMRI. NeuroImage 161, 179–187. https://doi.org/10.1016/j.neuroimage.2017.08.014

Purdon, P.L., Solo, V., Weisskoff, R.M., Brown, E.N., 2001. Locally Regularized Spatiotemporal Modeling and Model Comparison for Functional MRI. NeuroImage 14, 912–923. https://doi.org/10.1006/nimg.2001.0870

Purdon, P.L., Weisskoff, R.M., 1998. Effect of temporal autocorrelation due to physiological noise and stimulus paradigm on voxel-level false-positive rates in fMRI. Hum. Brain Mapp. 6, 239–249.

Ritter, P., Becker, R., Graefe, C., Villringer, A., 2007. Evaluating gradient artifact correction of EEG data acquired simultaneously with fMRI. Magn. Reson. Imaging 25, 923–932. https://doi.org/10.1016/j.mri.2007.03.005

Robinson, S., Windischberger, C., Rauscher, A., Moser, E., 2004. Optimized 3 T EPI of the amygdalae. Neuroimage 22, 203–10. https://doi.org/10.1016/j.neuroimage.2003.12.048

Robinson, S.D., Pripfl, J., Bauer, H., Moser, E., 2008. The impact of EPI voxel size on SNR and BOLD sensitivity in the anterior medio-temporal lobe: a comparative group study of deactivation of the Default Mode. Magn. Reson. Mater. Phys. Biol. Med. 21, 279–290. https://doi.org/10.1007/s10334-008-0128-0

Robson, M.D., Gore, J.C., Constable, R.T., 1997. Measurement of the point spread function in MRI using constant time imaging. Magn. Reson. Med. 38, 733–740.

Rosen, B.R., Savoy, R.L., 2012. fMRI at 20: Has it changed the world? NeuroImage, 20 YEARS OF fMRI 62, 1316–1324. https://doi.org/10.1016/j.neuroimage.2012.03.004

Sahib, A.K., Mathiak, K., Erb, M., Elshahabi, A., Klamer, S., Scheffler, K., Focke, N.K., Ethofer, T., 2016. Effect of temporal resolution and serial autocorrelations in event-related functional MRI. Magn. Reson. Med. 76, 1805–1813.

Schafer, A., Forstmann, B.U., Neumann, J., Wharton, S., Mietke, A., Bowtell, R., Turner, R., 2012. Direct visualization of the subthalamic nucleus and its iron distribution using high-resolution susceptibility mapping. Hum Brain Mapp 33, 2831–42. https://doi.org/10.1002/hbm.21404

Schenck, J.F., 2003. Magnetic resonance imaging of brain iron. J Neurol Sci 207, 99–102.

Schlindwein, F.S., Evans, D.H., 1992. Autoregressive spectral analysis as an alternative to fast Fourier transform analysis of Doppler ultrasound signals. Diagn. Vasc. Ultrasound 8, 74–84.

Schneider, R., Boada, F., Haueisen, J., Pfeuffer, J., 2015. Automated Slice-Specific Simultaneous Z-Shim Method for Reducing B1 Inhomogeneity and Susceptibility-Induced Signal Loss with Parallel Transmission at 3T. Magn. Reson. Med. 74, 934–944. https://doi.org/10.1002/mrm.25461

Schweser, F., Deistung, A., Lehr, B.W., Reichenbach, J.R., 2011. Quantitative imaging of intrinsic magnetic tissue properties using MRI signal phase: an approach to in vivo brain iron metabolism? Neuroimage 54, 2789–807. https://doi.org/10.1016/j.neuroimage.2010.10.070

Sedlacik, J., Boelmans, K., Lobel, U., Holst, B., Siemonsen, S., Fiehler, J., 2014. Reversible, irreversible and effective transverse relaxation rates in normal aging brain at 3T. Neuroimage 84, 1032–41. https://doi.org/10.1016/j.neuroimage.2013.08.051

Setsompop, K., Gagoski, B.A., Polimeni, J.R., Witzel, T., Wedeen, V.J., Wald, L.L., 2012. Blipped-controlled aliasing in parallel imaging for simultaneous multislice echo planar imaging with reduced g-factor penalty. Magn. Reson. Med. 67, 1210–1224. https://doi.org/10.1002/mrm.23097

Sheth, S.A., 2004. Columnar Specificity of Microvascular Oxygenation and Volume Responses: Implications for Functional Brain Mapping. J. Neurosci. 24, 634–641. https://doi.org/10.1523/JNEUROSCI.4526-03.2004

Shi, Z., Wu, R., Yang, P.-F., Wang, F., Wu, T.-L., Mishra, A., Chen, L.M., Gore, J.C., 2017. High spatial correspondence at a columnar level between activation and resting state fMRI signals and local field potentials. Proc. Natl. Acad. Sci. 114, 5253–5258. https://doi.org/10.1073/pnas.1620520114

Shmuel, A., Yacoub, E., Chaimow, D., Logothetis, N.K., Ugurbil, K., 2007. Spatio-temporal point-spread function of fMRI signal in human gray matter at 7 Tesla. NeuroImage 35, 539–552. https://doi.org/10.1016/j.neuroimage.2006.12.030

Skudlarski, P., Constable, R.T., Gore, J.C., 1999. ROC Analysis of Statistical Methods Used in Functional MRI: Individual Subjects. NeuroImage 9, 311–329. https://doi.org/10.1006/nimg.1999.0402

Sorenson, J.A., Wang, X., 1996. ROC methods for evaluation of fMRI techniques. Magn. Reson. Med. 36, 737–744. https://doi.org/10.1002/mrm.1910360512

Speck, O., Hennig, J., 1998. Functional Imaging by I0-and T2*-parameter mapping using multi-image EPI. Magn. Reson. Med. 40, 243–248.

Speck, O., Hennig, J., Zaitsev, M., 2006. Prospective Real-Time Slice-by-Slice Motion Correction for fMRI in Freely Moving Subjects. Magn. Reson. Mater. Phys. Biol. Med. 19, 55. https://doi.org/10.1007/s10334-006-0027-1

Speck, O., Stadler, J., Zaitsev, M., 2008. High resolution single-shot EPI at 7T. Magn. Reson. Mater. Phys. Biol. Med. 21, 73–86. https://doi.org/10.1007/s10334-007-0087-x

Stephan, K.E., Petzschner, F.H., Kasper, L., Bayer, J., Wellstein, K.V., Stefanics, G., Pruessmann, K.P., Heinzle, J., 2017a. Laminar fMRI and computational theories of brain function. NeuroImage. https://doi.org/10.1016/j.neuroimage.2017.11.001

Stephan, K.E., Schlagenhauf, F., Huys, Q.J.M., Raman, S., Aponte, E.A., Brodersen, K.H., Rigoux, L., Moran, R.J., Daunizeau, J., Dolan, R.J., Friston, K.J., Heinz, A., 2017b. Computational neuroimaging strategies for single patient predictions. NeuroImage 145, 180–199. https://doi.org/10.1016/j.neuroimage.2016.06.038

Stocker, T., Kellermann, T., Schneider, F., Habel, U., Amunts, K., Pieperhoff, P., Zilles, K., Shah, N.J., 2006. Dependence of amygdala activation on echo time: results from olfactory fMRI experiments. Neuroimage 30, 151–9. https://doi.org/10.1016/j.neuroimage.2005.09.050

Todd, N., Josephs, O., Zeidman, P., Flandin, G., Moeller, S., Weiskopf, N., 2017. Functional Sensitivity of 2D Simultaneous Multi-Slice Echo-Planar Imaging: Effects of Acceleration on g-factor and Physiological Noise. Front. Neurosci. 11. https://doi.org/10.3389/fnins.2017.00158

Todd, N., Moeller, S., Auerbach, E.J., Yacoub, E., Flandin, G., Weiskopf, N., 2016. Evaluation of 2D multiband EPI imaging for high-resolution, whole-brain, task-based fMRI studies at 3T: Sensitivity and slice leakage artifacts. NeuroImage 124, 32–42. https://doi.org/10.1016/j.neuroimage.2015.08.056

Triantafyllou, C., Hoge, R.D., Krueger, G., Wiggins, C.J., Potthast, A., Wiggins, G.C., Wald, L.L., 2005. Comparison of physiological noise at 1.5 T, 3 T and 7 T and optimization

of fMRI acquisition parameters. NeuroImage 26, 243–250. https://doi.org/10.1016/j.neuroimage.2005.01.007
Tziortzi, A.C., Haber, S.N., Searle, G.E., Tsoumpas, C., Long, C.J., Shotbolt, P., Douaud, G., Jbabdi, S., Behrens, T.E., Rabiner, E.A., Jenkinson, M., Gunn, R.N., 2014. Connectivity-based functional analysis of dopamine release in the striatum using diffusion-weighted MRI and positron emission tomography. Cereb Cortex 24, 1165–77. https://doi.org/10.1093/cercor/bhs397
Tziortzi, A.C., Searle, G.E., Tzimopoulou, S., Salinas, C., Beaver, J.D., Jenkinson, M., Laruelle, M., Rabiner, E.A., Gunn, R.N., 2011. Imaging dopamine receptors in humans with [11C]-(+)-PHNO: Dissection of D3 signal and anatomy. NeuroImage 54, 264–277. https://doi.org/10.1016/j.neuroimage.2010.06.044
Uludağ, K., Müller-Bierl, B., Uğurbil, K., 2009. An integrative model for neuronal activity-induced signal changes for gradient and spin echo functional imaging. NeuroImage 48, 150–165. https://doi.org/10.1016/j.neuroimage.2009.05.051
Van de Moortele, P.-F., Pfeuffer, J., Glover, G.H., Ugurbil, K., Hu, X., 2002. Respiration-induced B0 fluctuations and their spatial distribution in the human brain at 7 Tesla. Magn. Reson. Med. 47, 888–895. https://doi.org/10.1002/mrm.10145
Van Den Heuvel, M., Keilholz, S.D., Zalesky, A. (Eds.), 2017. Functional Architecture of the Brain. NeuroImage 160, 1–168.
van der Zwaag, W., Francis, S., Head, K., Peters, A., Gowland, P., Morris, P., Bowtell, R., 2009. fMRI at 1.5, 3 and 7 T: Characterising BOLD signal changes. NeuroImage 47, 1425–1434. https://doi.org/10.1016/j.neuroimage.2009.05.015
Van Essen, D.C., Smith, S.M., Barch, D.M., Behrens, T.E.J., Yacoub, E., Ugurbil, K., 2013. The WU-Minn Human Connectome Project: An overview. NeuroImage 80, 62–79. https://doi.org/10.1016/j.neuroimage.2013.05.041
Vannesjo, S.J., Wilm, B.J., Duerst, Y., Gross, S., Brunner, D.O., Dietrich, B.E., Schmid, T., Barmet, C., Pruessmann, K.P., 2015. Retrospective correction of physiological field fluctuations in high-field brain MRI using concurrent field monitoring. Magn. Reson. Med. 73, 1833–1843. https://doi.org/10.1002/mrm.25303
Viessmann, O.M., Bianciardi, M., Scheffler, K., Wald, L.L., Polimeni, J.R., 2018. The EPI rs-fMRI signal shows an orientation effect with respect to B0 and phase-encode axis across cortical depth, in: Presented at the 26th Annual Meeting of the International Society for Magnetic Resonance Imaging in Medicine. Paris, France, p. 0395.
Volz, S., Hattingen, E., Preibisch, C., Gasser, T., Deichmann, R., 2009. Reduction of susceptibility-induced signal losses in multi-gradient-echo images: Application to improved visualization of the subthalamic nucleus. NeuroImage 45, 1135–1143. https://doi.org/10.1016/j.neuroimage.2009.01.018
Wang, J.-Y., Zhuang, Q.-Q., Zhu, L.-B., Zhu, H., Li, T., Li, R., Chen, S.-F., Huang, C.-P., Zhang, X., Zhu, J.-H., 2016. Meta-analysis of brain iron levels of Parkinson's disease patients determined by postmortem and MRI measurements. Sci. Rep. 6, 36669. https://doi.org/10.1038/srep36669
Weiskopf, N., Hutton, C., Josephs, O., Deichmann, R., 2006. Optimal EPI parameters for reduction of susceptibility-induced BOLD sensitivity losses: A whole-brain analysis at 3 T and 1.5 T. NeuroImage 33, 493–504. https://doi.org/10.1016/j.neuroimage.2006.07.029
Weiskopf, N., Hutton, C., Josephs, O., Turner, R., Deichmann, R., 2007. Optimized EPI for fMRI studies of the orbitofrontal cortex: compensation of susceptibility-induced gradients in the readout direction. Magn. Reson. Mater. Phys. Biol. Med. 20, 39–49. https://doi.org/10.1007/s10334-006-0067-6
Weisskoff, R., Baker, J., Belliveau, J., Davis, T., Kwong, K., Cohen, M., Rosen, B., 1993. Power Spectrum Analysis of Funtionally-Weighted MR Data: What's in the Noise?, in: Proceedings of 12th SMRM Annual Meeting. New York, p. 7.

Welvaert, M., Rosseel, Y., 2013. On the Definition of Signal-To-Noise Ratio and Contrast-To-Noise Ratio for fMRI Data. PLoS ONE 8, e77089. https://doi.org/10.1371/journal.pone.0077089
Windischberger, C., Langenberger, H., Sycha, T., Tschernko, E.M., Fuchsjäger-Mayerl, G., Schmetterer, L., Moser, E., 2002. On the origin of respiratory artifacts in BOLD-EPI of the human brain. Magn. Reson. Imaging 20, 575–582. https://doi.org/10.1016/S0730-725X(02)00563-5
Wise, R.G., Ide, K., Poulin, M.J., Tracey, I., 2004. Resting fluctuations in arterial carbon dioxide induce significant low frequency variations in BOLD signal. NeuroImage 21, 1652–1664. https://doi.org/10.1016/j.neuroimage.2003.11.025
Wooldridge, J.M., 2013. Introductory econometrics: a modern approach, 5th ed. ed. South-Western Cengage Learning, Mason, OH.
Woolrich, M.W., Behrens, T.E.J., Smith, S.M., 2004. Constrained linear basis sets for HRF modelling using Variational Bayes. NeuroImage 21, 1748–1761. https://doi.org/10.1016/j.neuroimage.2003.12.024
Woolrich, M.W., Ripley, B.D., Brady, M., Smith, S.M., 2001. Temporal Autocorrelation in Univariate Linear Modeling of FMRI Data. NeuroImage 14, 1370–1386. https://doi.org/10.1006/nimg.2001.0931
Worsley, K., 2007. Chapter 18 - Random Field Theory, in: Friston, K.J., Ashburner, J., Kiebel, S., Nichols, T., Penny, W. (Eds.), Statistical Parametric Mapping. Academic Press, London, pp. 232–236.
Worsley, K.J., Friston, K.J., 1995. Analysis of fMRI time-series revisited--again. NeuroImage 2, 173–181. https://doi.org/10.1006/nimg.1995.1023
Worsley, K.J., Liao, C.H., Aston, J., Petre, V., Duncan, G.H., Morales, F., Evans, A.C., 2002. A General Statistical Analysis for fMRI Data. NeuroImage 15, 1–15. https://doi.org/10.1006/nimg.2001.0933
Wright, P.J., Mougin, O.E., Totman, J.J., Peters, A.M., Brookes, M.J., Coxon, R., Morris, P.E., Clemence, M., Francis, S.T., Bowtell, R.W., Gowland, P.A., 2008. Water proton T 1 measurements in brain tissue at 7, 3, and 1.5T using IR-EPI, IR-TSE, and MPRAGE: results and optimization. Magn. Reson. Mater. Phys. Biol. Med. 21, 121–130. https://doi.org/10.1007/s10334-008-0104-8
Wyss, M., Duerst, Y., Nanz, D., Kasper, L., Wilm, B.J., Dietrich, B.E., Gross, S., Schmid, T., Brunner, D.O., Pruessmann, K.P., 2017. Feedback field control improves the precision of T2 * quantification at 7 T. NMR Biomed. 30. https://doi.org/10.1002/nbm.3753
Yacoub, E., Duong, T.Q., Van De Moortele, P.-F., Lindquist, M., Adriany, G., Kim, S.-G., U?urbil, K., Hu, X., 2003. Spin-echo fMRI in humans using high spatial resolutions and high magnetic fields. Magn. Reson. Med. 49, 655–664. https://doi.org/10.1002/mrm.10433
Yacoub, E., Shmuel, A., Pfeuffer, J., Van De Moortele, P.-F., Adriany, G., Andersen, P., Vaughan, J.T., Merkle, H., Ugurbil, K., Hu, X., 2001. Imaging brain function in humans at 7 Tesla. Magn. Reson. Med. 45, 588–594. https://doi.org/10.1002/mrm.1080
Yacoub, E., Wald, L. (Eds.), 2018. Pushing the spatio-temporal limits of MRI and fMRI. NeuroImage 164, 1–230.
Yao, B., Li, T.Q., Gelderen, P., Shmueli, K., de Zwart, J.A., Duyn, J.H., 2009. Susceptibility contrast in high field MRI of human brain as a function of tissue iron content. Neuroimage 44, 1259–66. https://doi.org/10.1016/j.neuroimage.2008.10.029
Zimmer, F., O'Brien, K., Bollmann, S., Pfeuffer, J., Heberlein, K., Barth, M., 2016. Pulsed arterial spin labelling at ultra-high field with a B 1 + -optimised adiabatic labelling pulse. Magn. Reson. Mater. Phys. Biol. Med. 29, 463–473. https://doi.org/10.1007/s10334-016-0555-2

Appendix B

THE UNIVERSITY OF QUEENSLAND

Institutional Approval Form For Experiments On Humans Including Behavioural Research

Chief Investigator:	A/Prof Ross Cunnington
Project Title:	Attention, Perception, And the Planning Of Actions
Supervisor:	None
Co-Investigator(s):	Simandeep Poonian, Veronika Halasz, Jeffrey Bednark, Vinh Nguyen
Department(s):	QBI; Psychology
Project Number:	2011001394
Granting Agency/Degree:	None
Duration:	28th February 2015

Comments:

Name of responsible Committee:-
Medical Research Ethics Committee
This project complies with the provisions contained in the *National Statement on Ethical Conduct in Human Research* and complies with the regulations governing experimentation on humans.

Name of Ethics Committee representative:-
Professor Bill Vicenzino
Chairperson
Medical Research Ethics Committee

Date: 1 Feb 2012 Signature: _____